Analysis and Modelling of Turbulent Heat Flux in Canonical Shock-Turbulence Interaction

Thesis submitted

by

Russell Quadros
09401001

under the guidance of

Prof. Krishnendu Sinha

Department of Aerospace Engineering
Indian Institute of Technology Bombay
October 2015

Approval Sheet

This thesis entitled **'Analysis and Modelling of Turbulent Heat Flux in Canonical Shock-Turbulence Interaction'** by Mr. Russell Quadros is approved for submission in partial fulfillment of the degree of Doctor of Philosophy.

Examiners

____

____

____

Supervisor

____

Chairman

____

Date:________________

Place: _______________

Declaration

I declare that this written submission represents my ideas in my own words and where others' ideas or words have been included, I have adequately cited and referenced the original sources. I also declare that I have adhered to all principles of academic honesty and integrity and have not misrepresented or fabricated or falsified any idea/data/fact/source in my submission. I understand that any violation of the above will be cause for disciplinary action by the Institute and can also evoke penal action from the sources which have thus not been properly cited or from whom proper permission has not been taken when needed.

Signature

____

Name of the student

____

Roll No.

____

Date:________________

Abstract

High-speed turbulent flows with shock waves are characterized by high localized surface heat transfer rates. Computational predictions are often inaccurate due to the limitations in modelling of the unclosed turbulent energy flux in the regions of shock interaction, which have high mechanical non-equilibrium. In this work, we first investigate the turbulent energy flux generated when homogeneous isotropic turbulence passes through a nominally normal shock wave. We use linear interaction analysis where the incoming turbulence is idealized as being composed of a collection of two-dimensional planar waves, and the shock wave is taken to be a discontinuity. The nature of the post-shock turbulent energy flux is observed to be strongly dependent on the incidence angle of the incoming waves. Three-dimensional statistics, calculated by integrating two-dimensional results over a prescribed upstream energy spectrum, are compared with available direct numerical simulation data. A detailed budget of the governing equation is also considered in order to gain insight into the dominant mechanisms that affect the energy flux evolution.

We also study the variation of velocity-temperature correlation coefficient R_{uT} using linear interaction analysis and direct numerical simulation data; key similarities and differences between R_{uT} and the turbulent energy flux post-shock evolution are highlighted. The post-shock variation of R_{uT} is explained in terms of the contribution of the Kovasznay modes of vorticity, entropy and acoustic disturbances; the dominant modes contributing to R_{uT} are also identified. The modes themselves are then compared between the linear theory and the direct numerical simulation data to justify the match in the peak R_{uT} values at low Mach numbers. Based on the understanding of the physics of the problem, a simple algebraic model is proposed that correctly predicts the amplification of turbulent energy flux across the shock for varying upstream Mach numbers. Linear theory results, along with an understanding of the post-shock flow physics, is employed to devise a differential-equation based model that can capture the amplification of turbulent energy flux across the shock as well as its downstream evolution.

Contents

Abbreviations

DNS	**D**irect **N**umerical **S**imulation
LIA	**L**inear **I**nteraction **A**nalysis
RANS	**R**eynolds-**A**veraged **N**avier-**S**tokes
SBLI	**S**hock/**B**oundary-**L**ayer **I**nteraction
SST	**S**hear **S**tress **T**ransport
STI	**S**hock-**T**urbulence **I**nteraction
SRA	**S**trong **R**eynolds **A**nalogy
TKE	**T**urbulence **K**inetic **E**nergy

Symbols

a	Speed of sound
A_v	Complex amplitude of vorticity wave upstream of the shock
b_1	Shock-unsteadiness modelling parameter
c_0, c_1, c_{ue}	Closure coefficients in heat flux model
C_v	Specific heat at constant volume
C_p	Specific heat at constant pressure
C_μ^0	Closure constant in eddy-viscosity formulation
E	Total energy
e	Internal energy
e	Internal energy
e'_{rms}	Root mean square of internal energy fluctuation
E_{11}	Reynolds stress along streamwise direction
E_{22}, E_{33}	Reynolds stress along transverse direction
$E_{rr}, E_{\phi\phi}$	Reynolds stress along x_r and x_ϕ coordinates, respectively
E_k	Energy spectrum for isotropic turbulence
$\widetilde{F}, \widetilde{H}, \widetilde{K}$	Complex amplitudes associated with acoustic mode
$\widetilde{G}, \widetilde{I}$	Complex amplitudes associated with vorticity mode

h	Enthalpy
k	Wavenumber corresponding to shock-upstream vorticity wave
k_o	Wavenumber corresponding to peak energy level
$\overline{k}$	Streamwise wavenumber of downstream vorticity/entropy wave
$\widetilde{k}$	Streamwise wavenumber of downstream acoustic wave
$\overline{k}$	Streamwise wavenumber of downstream vorticity/entropy wave
$\widetilde{k}$	Streamwise wavenumber of downstream acoustic wave
l	Sine of the upstream incidence angle
$\widetilde{L}$	Complex amplitude associated with shock characteristics
L_ϵ	Dissipation length scale
m	Cosine of the upstream incidence angle
M	Mach number
M_t	Turbulent Mach number
p	Pressure
Pr_T	Turbulent Prandtl number
$\widetilde{Q}$	Complex amplitude associated with entropy mode
r	Compression ratio
R_{uT}	Velocity-temperature correlation coefficient
R	Gas constant
Re_λ	Reynolds number based on Taylor length scale
R_{kk}	Total Reynolds stress
R_{uT}	Velocity-temperature correlation coefficient
s_{ij}	Instantaneous strain-rate tensor
s	Entropy
t	Time
T	Temperature
T_t	Total temperature
u_j	Instantaneous velocity along j^{th} direction
u	Instantaneous streamwise velocity
u_n	Velocity normal to the instantaneous shock
u_t	Velocity tangential to the instantaneous shock

u	Instantaneous streamwise velocity
u'_{rms}	Root mean square of streamwise velocity fluctuation
U	Mean streamwise velocity
V	Specific volume
x_i	Coordinate along ith direction

ϵ	Turbulence dissipation rate
γ	Ratio of specific heats
κ_T	Turbulent conductivity
ω	Specific turbulence dissipation
ω_i	Vorticity along i^{th} coordinate
ψ	Angle of incidence of the upstream wave
ψ_c	Critical angle of incidence of the upstream wave
ψ_z	Angle of incidence yielding zero turbulent energy flux
ϕ	Angle of the $x - x_r$ plane with the $x - y$ plane
ρ	Density
σ_{ik}	Viscous stress tensor
ξ	Shock displacement
ξ_t	Shock speed
ξ_y	Shock distortion

Superscripts

$()'$	Reynolds fluctuation
$()''$	Favre fluctuation
$\overline{()}$	Reynolds averaging
$\widetilde{()}$	Favre averaging

Chapter 1

Introduction

1.1 Motivation

The interaction with a shock wave can drastically alter the characteristics of the incoming turbulence. Compression by the shock decreases the turbulent length and time scales, and also amplifies the turbulence kinetic energy and vorticity fluctuations. The temperature jump across a shock leads to higher viscosity and thus enhanced turbulent dissipation downstream of the shock. Shock-turbulence interaction often generates large amount of acoustic energy. Due to its strong directional character, shock waves impart significant anisotropy to the turbulence field.

Shock-turbulence interaction is of practical interest in many high-speed flows. It is at the heart of shock/boundary-layer interaction, which occurs in applications ranging from transonic to hypersonic Mach numbers. Post-shock turbulence levels determine the extent of flow separation, and the associated pressure and heat loads in such interactions. Shock/boundary-layer interactions in rocket nozzles often lead to unsteady side loads. They can also alter the effectiveness of control surfaces and engine intakes. Enhanced turbulent mixing due to shock waves can be beneficial in supersonic combustors.

Engineering predictions of shock/boundary-layer interaction (SBLI) in practical configurations rely on the Reynolds-averaged Navier Stokes (RANS) approach. Conventional turbulence models, like the $k-\epsilon$ and $k-\omega$ models, often give inaccurate predictions of wall pressure, separation size and wall heat flux [1]. This is primarily because of the underlying gradient diffusion hypothesis that fails in rapidly distorted mean flow such as shock waves. Improvements like those in the realizable $k-\epsilon$ models [2], stress-limited $k-\omega$ model [3] and the SST model [4] address some of these limitations. In addition, several physics-based turbulence models have been proposed specifically for shock-dominated flows. Sinha et al. [5] model the damping effect of shock oscillations on the turbulent kinetic energy in the $k-\epsilon$ framework. In a subsequent work, Veera and Sinha [6] model the effect of upstream temperature fluctuations on turbulent kinetic energy amplification. The evolution of transverse vorticity fluctuations and the effect of baroclinic torques on enstrophy amplification is also studied by Sinha [7]. This lead to lead to an accurate model equation for the turbulent dissipation rate across a shock wave.

Much of the enhanced modelling has been focused on Reynolds stresses, TKE and its dissipation rate. They have a direct bearing on the fluid dynamic aspects of the interaction, and hence have led to better prediction of the separation bubble size, the shock structure and the surface pressure distribution. Improvements in the overall flow topology in the interaction region has also resulted in some limited improvement in the surface heat flux prediction as well [8]. However, there has been very little work directly in the area of heat transfer in shock-dominated flows. Specifically, to understand how the interaction with a shock wave alters the internal energy transport in a turbulent flow.

The turbulent heat transfer is given by either the turbulent enthalpy flux $\widetilde{u_j''h''}$ or the turbulent energy flux $\widetilde{u_j''e''}$, where u_j is the velocity in the j^{th} direction, h is the specific enthalpy and e is the specific internal energy of the gas. Tilde represents Favre averaging and the corresponding fluctuations are marked by double primes. The correlation represents the transport of internal energy by velocity fluctuations in a turbulent flow. It is traditionally modelled in terms of mean temperature gradient and a turbulent conductivity, which is related to the eddy viscosity via a turbulent Prandtl number Pr_T. A value of $Pr_T = 1$ can be derived from the strong Reynolds analogy (SRA) proposed by Morkovin [9]. In practise, a constant value of $Pr_T = 0.89$ gives satisfactory results in flat plate boundary-layer flows and is often used in SBLI applications.

Mahesh et al. [10] show that SRA is not valid across a shock wave and thus, the assumption of a constant Pr_T value may not be applicable to shock-dominated flows. A variable Pr_T model proposed by Xiao et al. [11] is found to improve SBLI results. Similar models are proposed by Sommer et al. [12], Brinckman et al. [13] and Goldberg et al. [14]. In another work, Bowersox [15] presents the exact transport equation for the turbulent energy flux, and simplifies it to get an algebraic model in terms of gradients in mean quantities. The model is independent of the turbulent Prandtl number, but is limited to zero-pressure-gradient boundary layers. To the best of our knowledge, there is no direct study of turbulent energy flux in shock-dominated flows.

The presence of a shock wave can significantly alter the energy transport in a turbulent flow. For example, shock impingement on a boundary layer can result in up to 400% increase in the surface heat flux [16]. The turbulent heat flux generated by the shock wave is possibly a key factor that results in the dramatically increased surface heating rate. The direction of the turbulent heat flux relative to the shock wave and the inclination of the shock with respect to the wall are other factors that may influence the surface heat flux. It is therefore important to know the magnitude and sign of the turbulent energy flux in the post-shock flow, and the physical parameters that govern these quantities. A knowledge of the underlying physics and their characteristic scaling is crucial to develop advanced turbulence models for accurate heat flux prediction.

An associated quantity of interest in heat flux prediction is the turbulent heat flux correlation coefficient R_{uT}, given by

$$R_{uT} = \widetilde{u''T''}/(\sqrt{\widetilde{u''^2}}\sqrt{\widetilde{T''^2}}), \tag{1.1}$$

where $\widetilde{u''T''}$ is the turbulent heat flux and T'' corresponds to temperature fluctuation. From strong Reynolds analogy (SRA) [9], a value of $R_{uT} = -1$ can be deduced for high Reynolds number boundary layers over adiabatic flat plates. This value of R_{uT} corresponds to a $Pr_T \sim 1$ used in conventional RANS models. However, as SRA fails across the shock, R_{uT} may no longer remain constant. A limited analysis of the correlation coefficient in canonical shock-turbulence interaction has been carried out by Mahesh et al. [10], who studied its streamwise variation in the region downstream of the shock for two cases of upstream Mach number. A detailed understanding into the effect of shock on R_{uT} could aid the modelling of the turbulent energy flux vector.

1.2 Objectives

The focus of the current work is to:

- Analyze the generation of turbulent energy flux across the shock in a canonical shock-turbulence interaction using linear interaction analysis and direct numerical simulation data.
- Develop modelling strategies to capture the essential physics of the turbulent energy flux in canonical shock-turbulence interaction.
- Study the effect of upstream parameters on the velocity-temperature correlation coefficient R_{uT}, and understand its variation behind a shock wave.

Canonical shock-turbulence interaction (STI) considered in the current study consists of homogeneous isotropic turbulence passing through a nominally normal shock wave. The upstream turbulence is carried by a steady, one-dimensional, uniform mean flow. This is a fundamental problem that isolates the effect of a shock wave on turbulence. It eliminates other effects like boundary-layer gradients, flow separation, shear layer attachment and streamline curvature, which are present in SBLI flows. In spite of the geometrical simplicity, the model problem exhibits a range of physical effects. These include turbulence anisotropy, generation of acoustic waves, baroclinic torques, and unsteady shock oscillations. Availability of direct numerical simulation (DNS) data and theoretical results make it an ideal problem to study the underlying physics. Physical insights obtained in this canonical problem have proved useful in developing advanced turbulence models for SBLI application [7].

One of the important tools in studying shock-turbulence interaction is linear interaction analysis (LIA) [17, 18]. This theoretical tool models the incoming turbulence as a spectrum of planar waves independently interacting with the shock. LIA has been shown to capture the jump across the shock in turbulence kinetic energy and enstrophy well [5, 7]. Turbulence models based on these LIA results have improved the prediction of surface pressure and flow topology in SBLI flows. In spite of the usefulness of LIA, it has not been used in studying turbulent energy flux, whose study could have direct implications on improving the wall heat flux predictions in SBLI.

The LIA results pertaining to turbulent energy flux and velocity-temperature correlation, and the modelling strategies discussed in this report is a step in this direction.

1.3 Scope of thesis

Chapter 2 describes some of the earlier works in turbulent energy flux studies primarily in supersonic boundary-layer flows. Earlier efforts in modelling the turbulent energy flux, both in supersonic as well as subsonic flows are also discussed. Canonical shock/boundary-layer interaction is described along with RANS capability in predicting the wall heat flux. The canonical shock-turbulence interaction, which is considered in the current work for studying the turbulent energy flux, has been studied extensively in the past using LIA and DNS. Some of these earlier works and their implications in RANS modelling of SBLI flows are also discussed.

Chapter 3 explains the formulation of LIA [17–19] used in the current work. The theory models the turbulence field upstream of the shock as a collection of two-dimensional plane waves of varying intensity, wavenumber and frequency. Each planar disturbance wave interacts independently with the shock wave and generates downstream fluctuations. A superposition of the downstream waves, for a given upstream energy spectrum, gives the turbulent statistics behind the shock wave. DNS study for this canonical configuration was carried out by Larsson et al. [20] for varying upstream Mach number, Reynolds number and turbulent Mach number. Details of this study along with the procedure for the DNS data analysis are also provided in this chapter.

Chapter 4 describes in detail the results for turbulent energy flux obtained in the canonical STI configuration using linear theory and DNS data. As a starting point, an elementary interaction of a single planar vortical wave with a normal shock is studied. The effects of upstream mean flow Mach number and the wave incidence angle (relative to the shock-normal direction) on the energy flux are investigated. Interactions that lead to peak turbulent energy flux and those with vanishingly small values of the correlation are identified for each Mach number. Three-dimensional statistics, computed by integrating the single-wave contributions, are analysed for varying shock strengths. The linear theory results for three-dimensional turbulence are compared with available DNS data. Both the streamwise evolution as well as the peak energy flux behind the shock, are compared for a range of shock strengths. The DNS data is further used to compute the budget of the turbulent energy flux transport equation downstream of the shock.

The modelling of turbulent energy flux in the canonical STI is discussed in chapter 5. First, the conventional eddy viscosity model and realizability model are used to predict the turbulent energy flux in the canonical STI, and their shortcomings are highlighted. Further, an algebraic model based on the realizability formulation is proposed to capture the jump in turbulent energy flux across the shock for varying upstream Mach numbers. To capture the jump in the turbulent energy flux as well as its evolution downstream of the shock, a physics based model transport equation is proposed that can be solved in conjunction with the $k - \epsilon$ equations. The model predictions are further compared with the DNS data.

Chapter 6 describes the study of R_{uT} for the canonical STI configuration. The results obtained from LIA and DNS are compared for varying upstream Mach numbers. Effect of upstream turbulent Mach number as well as Reynolds number on the correlation coefficient is also highlighted using DNS data. Contribution of each of the Kovaznay modes to R_{uT} is studied using LIA. The individual Kovaznay modes are then compared between LIA and DNS both in the region just across the shock as well as along the streamwise direction. This provides insight into the match between the LIA and DNS R_{uT} streamwise variation at low Mach numbers. Finally, chapter 7 brings out the important outcomes of this report.

Chapter 2

Literature Survey

The current report is based on studying the velocity-temperature correlation across a shock. Most studies with respect to this correlation are based in configurations such as supersonic flow over flat plate, jet impingement and in low-speed shear layers. Some of these studies are discussed in section 2.1, along with some limited insight obtained earlier with respect to velocity-temperature correlation in shock-turbulence interaction. Several models have been proposed to capture the physics of velocity-temperature correlation, which has direct consequence on the heat transfer prediction. These models, both in shock-dominated flows and in low-speed flows, are also discussed in section 2.1.

One of the purpose of the current study is to gain insight into RANS modelling of turbulent energy flux in shock-dominated flows, which in turn has effect on the wall heat flux prediction. In section 2.2, we describe two SBLI configurations, and highlight the inability of conventional RANS models to predict the wall heat flux. A configuration of canonical shock-turbulence interaction is assumed for the current study of the correlation. This simplistic yet insightful configuration has been subjected to theoretical, numerical, experimental and modelling works. These are described in section 2.3. Some of the useful outcomes of studying STI on developing physics-based models for SBLI are also discussed in this section.

2.1 Turbulent heat transfer

Most of the earlier works in analysing the turbulent heat transfer have been focussed on studying the velocity-temperature correlation coefficient R_{uT} given by (1.1). R_{uT} represents the correlation between the velocity and the temperature fluctuations in a turbulent flow, and this correlation has a significant effect on the wall heat transfer rates in realistic geometries. A strong correlation between the velocity and the temperature fluctuations was observed in supersonic boundary layers by Morkovin [9], with R_{uT} assuming a value close to -1. This value of R_{uT} directly corresponds the turbulent Prandtl number Pr_T,which is used in conventional modelling. The basis for this value of R_{uT} relies on the fact that the total temperature fluctuations are negligible in such flows. Laurent [21] showed experimentally that the variation of total temperature along the wall-normal direction in a supersonic boundary layer with adiabatic wall conditions, although small cannot be neglected. Debi'eve [22] and Dussage [23] studied supersonic boundary layers with isothermal wall boundary and found experimentally that the value of R_{uT} was almost constant with a value of about -0.8. The correlation coefficient has been studied numerically as well by Wu and Martin [24], who for a supersonic flow over flat plate, used DNS to show that the value of R_{uT} was close to -1 near the wall and a value of about -0.8 along the rest of the boundary layer in the wall-normal direction. A similar DNS study of a supersonic boundary-layer over a flat plate with adiabatic wall conditions was carried out by Pirozzoli et al. [25], who also showed that R_{uT} assumes a value close to -1 near the wall and a value of about -0.5 for most part of the boundary layer in agreement with the low Mach number results. This value of $R_{uT} = -1$ close to the wall can be attributed to the total temperature fluctuations also being small in the near-wall region [25]. Hence, strong Reynolds analogy (SRA) is valid, and R_{uT} and Pr_T take a value close to -1 and 1, respectively (details are provided in section 3.2.4). Away from the wall, the total temperature fluctuations are not negligible, and are of the same order as the static temperature fluctuations in most of the boundary layer [25]. This reflects in the value of R_{uT} and Pr_T deviating from the predictions as per SRA.

Although R_{uT} has been thoroughly studied in supersonic boundary layers, few studies have highlighted the effect of shock waves on the correlation coefficient. Mahesh et al. [10] performed a DNS for isotropic turbulence with vorticity-entropy fluctuations interacting with a normal shock. The upstream turbulence satisfied the Morkovin's hypothesis with a value of $R_{uT} \sim -1$. The value of R_{uT} was seen to decrease in magnitude across the shock with a further decrease along streamwise direction. For an upstream Mach number of 1.29, the value of R_{uT} decreased to about -0.54 at a distance of about $k_0 x = 20$ from the shock, and for a Mach number of 1.8, the value reduces to -0.22 for the same distance from the shock. Here, k_0 represents the wavenumber corresponding to the peak energy level upstream of the shock and x indicates the streamwise distance. They further provide a reason for the variation in R_{uT} across the shock by studying the validity of the Morkovin's hypothesis. Significant total temperature fluctuations are generated at the shock, and their magnitudes increase with increasing Mach number. This leads to a breakdown in the Morkovin's hypothesis that is formulated on the basis of the total temperature fluctuations being negligible.

An important turbulent correlation in the mean energy conservation equation that directly affects the turbulent heat transfer is turbulent energy flux. Conventional models based on Reynolds-averaged Navier-Stokes (RANS) approach incorporate the physics of the turbulent energy flux based on the gradient diffusion hypothesis i.e.,

$$\widetilde{u''e''} = -\frac{\mu_T}{\overline{\rho} Pr_T} \frac{\partial \widetilde{e}}{\partial x}, \tag{2.1}$$

where $\overline{\rho}$ and $\widetilde{e}$ are the mean density and mean internal energy. μ_T is the eddy viscosity and Pr_T is the turbulent Prandtl number, which assumes a constant value based on the Morkovin's hypothesis. Constant Pr_T models pose several limitations in predicting the heat transfer rates in shock-dominated flows. Xiao et al. [11] showed that the conventional model based on a constant value of $Pr_T = 0.89$ significantly overpredict the wall heat flux in shock-dominated flows. They modelled additional two transport equations for enthalpy variance and its dissipation rate, and calculated Pr_T at each point in the flow field in terms of these correlations. The new model was applied to the case of an oblique shock impinging on a turbulent boundary layer; a significant improvement over a constant Pr_T model in the wall heat flux prediction was observed.

Bowersox [15] showed that although the conventional model based on gradient diffusion hypothesis is able to predict the transverse energy flux in supersonic flat plate boundary-layer flow with adiabatic wall conditions, it severely underpredicts the streamwise energy flux. He presented an exact transport equation for the turbulent energy flux, and simplified it to get an algebraic model in terms of gradients in mean quantities. The model is independent of the turbulent Prandtl number and predicts the energy flux values well, but is limited to zero-pressure-gradient boundary layers. Brinckman et al. [13] also suggested a variable Pr_T model for the turbulent heat flux by solving additional transport equations for internal energy variance and its dissipation rate. This formulation was applied to a hot jet flow at Mach number of 2.0 and an improved prediction in mean temperature along the centerline was observed as compared to the constant Pr_T formulation.

Goldberg et al. [14] proposed an algebraic model based on Rodi [26] Reynolds stress formulation to calculate the value of Pr_T locally in the flow. This formulation was applied to cases such as flow over heated plate and jet impingement on a plate at subsonic speed, and modest improvements in heat transfer rate were observed. Aouissi et al. [27] also suggested a variable Pr_T model to predict the turbulent heat flux in round jets. Additional two equations for temperature variance and its dissipation rate were solved and Pr_T was formulated as a function of these two variables. Similar to the experimental results, the model also predicted an almost constant values of Pr_T near the centerline and a steady increase in the Pr_T values towards the periphery of the jet.

Sommer et al. [12] developed a variable turbulent Prandtl number (Pr_T) model for high-speed compressible turbulent boundary layers with adiabatic and isothermal wall conditions. Additional equations for temperature variance and its dissipation were solved in order to calculate Pr_T at each point in the flow field with free stream Mach number reaching as high as 10. A good match in the mean variables was obtained, and Pr_T values were observed to vary along the wall-normal direction with low values near the wall. So and Sommer [28] proposed an explicit algebraic heat flux model that allowed for modelling of the heat flux vector even when the corresponding mean temperature gradient was zero. The model was compared with DNS and experimental data of fully developed channel and pipe flows, both at low as well as high Reynolds number, and was observed to predict the turbulent heat flux correctly.

Abe and Suga [29] with the aid of LES data developed an algebraic scalar-flux model for channel flow under varying flow-boundary conditions and Prandtl numbers. The turbulent scalar flux was expressed in terms of the gradient in mean temperature and a quadratic product of the Reynolds-stress tensor; an improvement in the prediction of turbulent scalar flux in flows with high shear strain was observed. Uddin et al. [30] investigated impingement of turbulent jet orthogonally on a target surface using large eddy simulation (LES). Three alternate models for predicting the turbulent heat flux by Daly and Harlow [31], Abe and Suga [29] and Younis et al. [32] were employed to study the heat transfer. The model by Younis et al. [32] was observed to predict the radial scalar flux much better as compared to the other two models.

Shams et al. [33] considered low Prandtl number flows such as those involving liquid metal and proposed an algebraic turbulent heat flux model to accurately predict the heat transfer. The proposed correlation involved a dependency on Reynolds- and Prandtl number, and the results obtained compared well with the DNS data for various test cases. Pucciarellia et al. [34] assessed various turbulent heat flux models for predicting heat transfer in supercritical pressure fluids and highlighted the general characteristics of each model considered. Schneider et al. [35] with help of LES, tested the validity of algebraic standard turbulent heat flux model applied to trailing-edge section of a turbine blade with film cooling. They showed that the standard model failed in capturing the film cooling predictions at different blowing ratios both qualitatively and quantitatively. Müller et al. [36] developed an algebraic compact, non-linear model for turbulent heat flux prediction in a rotating channel flow. Comparison of heat-transfer rates with experimental and DNS data showed a fairly good match for different rotation rates and Reynolds numbers.

2.2 Shock/boundary-layer interaction

One of the major challenges in design of any supersonic vehicle is the prediction of peak heating and pressure loads on the components. Shock/boundary-layer interaction (SBLI) occuring in high-speed vehicles is one of the reasons for the high loading, and needs to be studied in detail. Carefully designed experiments have isolated the regions of these interactions, and the peak loads along with the flow topology have been analyzed. In this section, we present some of

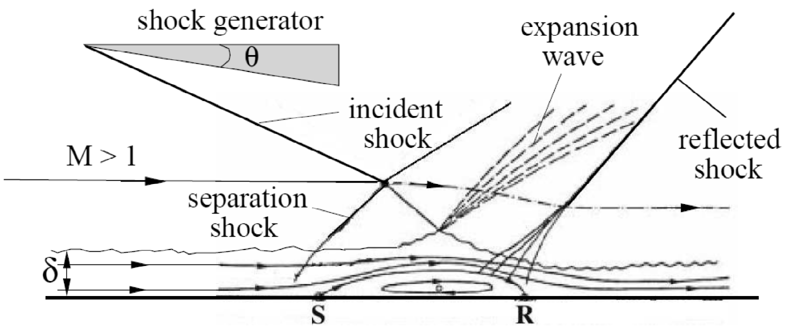

FIGURE 2.1: Schematic of an oblique shock impinging on a turbulent boundary layer; figure also shows the separation region bounded by points S and R. Reproduced from Pasha [37].

the earlier literature in canonical SBLI configurations and Reynolds-averaged Navier-Stokes (RANS) capability in predicting important quantities such as wall heat flux.

2.2.1 Oblique shock impingement

Figure 2.1 shows the schematic of an oblique shock impinging on a turbulent boundary layer. The strength of the oblique shock is governed by the angle made by the shock generator θ to the direction of the incoming flow. A strong shock impinging on the incoming boundary layer leads to a highly adverse pressure gradient, thus causing a separation close to the point of impingement. Points S and R in the schematic show the extent of separation. The presence of a separation region adds to the complexity of the flow topology; additional features such as separation and reflected shocks are generated. The region where the reflected shock is close to the wall expiriences peak heat and pressure loads.

Schulein [16] experimentally studied the case of oblique shock impingement considering three deflection angles of the shock generator corresponding to varying oblique shock strength. Some of the parameters associated with the incoming flow were an upstream Mach number $M_\infty = 5$, freestream temperature $T_\infty = 68.3K$, pressure $P_\infty = 4008N/m^2$ and unit Reynolds number $Re_\infty = 37 \times 10^6 m^{-1}$. The wall was maintained at a constant temperature of 300 K.

Pasha and Sinha [38] performed RANS simulation for the configuration using standard $k - \omega$ model. An improvement in prediction of wall pressure and skin friction coefficient was obtained by adding the shock-unsteadiness correction of Sinha et al. [5]. The wall heat flux was also

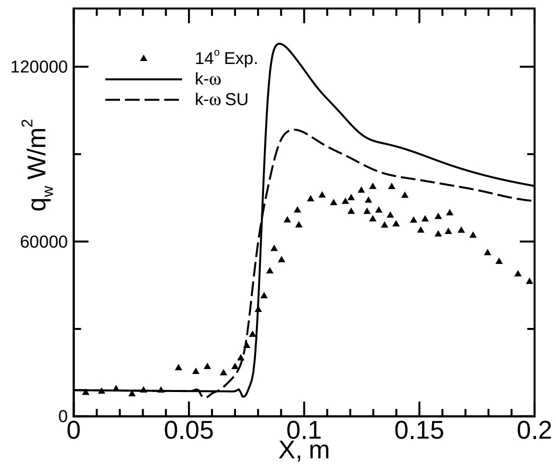

FIGURE 2.2: Wall heat flux as predicted by standard (solid) and shock-unsteadiness modified (dashed) $k-\omega$ models compared with the experimental data (symbols) for an oblique shock impingement case; the case corresponds to 14^o deflection angle of the shock generator (see Schulein [16]).

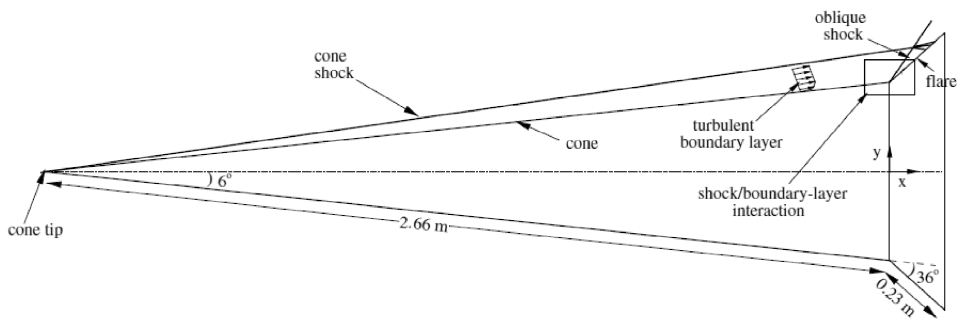

FIGURE 2.3: Schematic of hypersonic cone-flare configuration as described in [39]. Figure reproduced from [8].

calculated using the standard and the shock-unsteadiness model, and the results are shown in figure 2.2. Conventional model overpredicted the peak wall heat flux by almost hundred percent; a significant improvement was observed upon using the shock-unsteadiness modification. There is still a need to bridge the gap between the experimental and numerical results, which calls for a detailed understanding of the flow physics especially in the vicinity of shocks.

2.2.2 Hypersonic cone-flare configuration

Another configuration that brings out the essential physics of shock/boundary-layer interaction is the cone-flare geometry. Figure 2.3 shows the schematic of the interaction. Both cone and flare are at an angle to the incoming flow; the inlet Mach as well as the angle of flare are important in deciding the separation region size. Points S and R correspond to the bounds of the separation region. The region close to the reattachment shock experiences maximum heat and pressure loads.

Pasha and Sinha [8] performed RANS simulations for the cone-flare configuration using standard and shock-unsteadiness [7] $k-\omega$ models. The incoming Mach number was 13.1 and the flare angle was at 36^o so as to cause significant separation at the cone-flare junction. Figure 2.4 shows the wall heat flux as predicted by the RANS models compared with the experimental results of Holden [39]. The zero mark on the x axis indicates the position of the cone-flare junction. The standard $k-\omega$ model does not capture the separation region, and predicts a sudden increase in the heat flux at the junction; it also underpredicts the peak wall heat flux in comparison with the experiment. The shock-unsteadiness model predicts a separation region ($-0.8 < s < 0$), also capturing an increased wall heat flux in this region. The peak heat flux occuring close to the reattachment shock is also predicted by the model; however there are qualitative differences between the experiment and the simulation.

Some other canonical SBLI configurations include compression corner [40] and three-dimensional single fin interaction [37], which also show the defficiency in the RANS models to capture the wall heat flux values. It is therefore essential to study some of the relevant unclosed correlations in the mean energy conservation equation, and model them correctly in the shock regions, so as to improve the wall heat flux predictions.

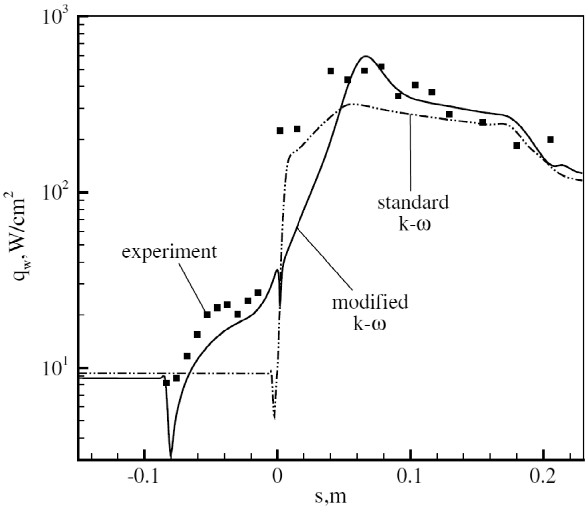

FIGURE 2.4: Wall heat flux as predicted by standard and modified $k-\omega$ models compared with the experimental data for a hypersonic cone-flare configuration at Mach 13.1 with a 36^o flare angle[39]. Figure reproduced from Pasha and Sinha [8].

2.3 Shock-turbulence interaction

Interaction of homogeneous isotropic turbulence with a normal shock, often referred to as canonical shock-turbulence interaction, is a problem rich in flow physics and has been the subject of research for over five decades. Several interesting aspects of the problem have been studied using theoretical analysis, direct numerical simulation and experiments. The understanding of the flow physics has been employed to devise new RANS models for STI, which have been later extended to SBLI configurations. In the following section, we look at some of the important works that have been carried out in canonical STI and highlight the key contributions.

2.3.1 Decomposition

Kovasznay [41] showed that a compressible, viscous and heat-conductive gas can have three distinctly different types of disturbance fields, following three independent differential equations. These three "modes" of disturbance are vorticity, entropy and acoustic (sound-wave) modes. Using experiments in supersonic flow, he demonstrated that the modes propagate independently when the intensity of fluctuations is small, and interact with each other at larger intensities where linearisation is not valid. Details are provided in section 3.3.2. Stanišić and Kovasznay [42] extend this work to identify the independent weak fluctuation modes of an electrically and thermally conducting viscous incompressible fluid in a homogeneous magnetic field.

Doak [43] showed that the mean (time-averaged) energy flux in a time-stationary fluctuating flow is a linear superposition of mean, turbulent, acoustic and thermal components. Sarkar et al. [44] studied the DNS databases for the homogeneous compressible turbulence and proposed a novel decomposition of pressure into incompressible and compressible components, which was further used to model the pressure-dilatation term in the governing equation for turbulent kinetic energy. Mahesh et al. [45] studied the individual contribution of Kovasznay modes to the turbulent kinetic energy generated, when a field of acoustic disturbances interacted with the shock. Similar contribution of the individual modes to total temperature fluctuation downstream of the shock was studied by Mahesh et al. [10].

2.3.2 Linear interaction

Theoretical treatment of canonical STI has been pursued to a large extent using linear interaction analysis (LIA). Ribner [17] formulated LIA to study the interaction between a single vortical planar wave and a normal shock, and highlighted the generation of acoustic and entropy wave downstream of the shock. He further extended this analysis [18] to study an isotropic turbulence field consisting of a spectrum of convected planar waves interacting with a shock, with emphasis on the post-shock noise levels. Moore [46] studied the interaction of an oblique planar sound wave with a shock and showed that when a single wave interacts with the shock, all three disturbance waves i.e., vorticity, entropy and acoustic, are generated. A similar study was also carried out by Kerrebrock [47] and Chang [48].

Ribner [49] extended his earlier work on the single-wave and three-dimensional analysis to study the acoustic energy flux emanating from an unit area behind the shock upon interacting with a turbulence field containing only small vortical fluctuations. In this work he also showed that the acoustic flux generated varied linearly with the shock density ratio. Ribner [50] also studied the one-dimensional power spectra for velocity, temperature and pressure perturbation in a shock-turbulence interaction.

In later works, Lee et al. [51, 52] used LIA to compare with the DNS results of shock-turbulence interaction, and showed a good match in quantities such as turbulent kinetic energy amplification. Mahesh et al. [45] in their study of an acoustic turbulent field interacting with a shock, showed good match between the LIA results of Moore [46] and the corresponding DNS data. In their subsequent work, Mahesh et al. [10] numerically simulated a turbulent field with vorticity-entropy fluctuations and studied the effect of upstream temperature fluctuations on the downstream turbulent correlations. Linear theory results matched important quantities such as amplification of TKE, and also helped probe the Morkovin's hypothesis at the shock. Jamme et al. [53] used LIA to compare with their DNS results for the case of isotropic turbulence with upstream vortical and acoustic disturbance interacting with a normal shock. Both LIA and DNS showed that the influence of upstream acoustic wave on the TKE amplification is noticeable for only those Mach numbers ranging between 1.25 and 1.8.

In other works, Fabre et al. [54] used LIA to study the interaction of a cylindrical element of hot or cold gas (an entropy spot) with a shock wave. The entropy spot was modelled to have a gaussian profile, and the downstream vorticity and pressure patterns generated were studied in detail. They then compared the results with numerical simulation and observed excellent agreement with LIA even for large spot amplitudes. Griffond [55] employed LIA to get insights in the Richtmyer-Meshkov instability occuring when a shock wave hits an interface between two gases. The analysis was carried out for gases with close molar mass and specific heat (low Atwood numbers). The vorticity field deduced from LIA was compared with two-dimensional numerical simulations, and a good agreement was obtained. Larsson and Lele [56] and Larsson et al. [20] used LIA to show a good match with numerical simulations in predicting TKE amplification for a wide range of upstream Mach numbers. The amplification of vorticity variance across the shock using LIA was studied by Sinha [7] and a good match with DNS data was observed again for a wide range of upstream Mach numbers. Ryu and Livescu [57] showed that the downstream DNS statistics including the streamwise and transverse Reynolds stresses, converge to the LIA solutions as the turbulent Mach number becomes very small, even at low values of Reynolds number. These studies over almost five decades have shown that linear theory is indeed a powerful tool in analysing some of the essential physics of the shock-turbulence interaction.

Duck et al. [58] theoretically studied the interaction of an oblique shock with freestream, single-wavelength, plane-wave disturbance and highlighted how the presence of the wedge affects the interaction. They laid special emphasis on studying the pressure disturbances along the wedge (relates to boundary-layer receptivity) and to the vorticity generated behind the shock wave (leads to enhanced mixing). McKenzie and Westphal [59] also study the interaction of linear waves with oblique shock waves and quantify the pressure amplitudes in the post-shock region for varying upstream disturbances.

Mahesh et al. [60] used rapid distortion theory (RDT) to study the response of shear flows and axisymmetric turbulence to rapid one-dimensional compression. The effect of the rapid compression on TKE and its components was studied and the relevant parameters influencing the downstream evolution of TKE were identified. With respect to shock-turbulence interaction, they showed that the evolution of turbulence across the shock is governed by the shock strength, the anisotropy of the incoming turbulence and the shock inclination angle. Jacquin et al. [61] also studied the applicability of RDT to shock-turbulence interaction. They studied the TKE behind the shock and compared the RDT results with the LIA values, and observed significant difference between the two approaches. Lee et al. [62] state that this difference could be due to the inability of RDT formulation to take into account the shock-unsteadiness and shock-curvature effects which have considerable effect on the downstream fluctuations.

2.3.3 Numerical analysis

Numerical analysis of canonical shock-turbulence interaction has been carried out primarily using direct numerical simulation (DNS). One of the early DNS studies of shock-turbulence interaction was by carried out by Lee et al. [51]. Both, the mean as well as the turbulent Mach numbers considered for study had low magnitudes, and the upstream turbulence comprised of vortical fluctuations with negligible thermodynamic fluctuations. They defined a ratio of the form $M_t^2/(M^2-1)$, whose value when below 0.1 gave favorable comparison with the shock front distortion as predicted by the linear theory. Here, M_t is the turbulent Mach number and M is the mean upstream Mach number. Amplification of TKE and transverse vorticity across the shock, distortion of the shock front, generation of high values of thermodynamic fluctuations were also studied in detail. An extension to this study was presented by Lee et al. [52] who carried out DNS of the canonical STI at higher Mach numbers. Emphasis was also laid on change in turbulent length scales across the shock, and most length scales were seen to decrease post the interaction in agreement with the LIA predictions.

Mahesh et al. [45] used DNS to study the interaction of an isotropic field of acoustic waves with a shock wave. The mean Mach number regime spanned from $1.25 - 5$. Variation in post-shock sound intensity and generation of vorticity-entropy fluctuations with increasing Mach number was studied in detail. Influence of upstream entropy fluctuations on the downstream turbulent statistics was also studied by Mahesh et al. [10]. They showed that a negative correlation between velocity and temperature fluctuation upstream of the shock resulted in a higher amplification of turbulence kinetic energy, transverse vorticity and thermodynamic fluctuations.

Jamme et al. [53] carried out DNS to study the effect of varying upstream turbulence cases such as solenoidal, vorticity-entropy and vorticity-acoustic, on the post-shock turbulence statistics. They observed that the introduction of additional acoustic fluctuations upstream of the shock had a negative effect on TKE amplification and a positive effect on transverse vorticity amplification, as compared with a purely solenoidal upstream turbulence. Larsson and Lele [56] considered a wide range of upstream Mach numbers $(1.27 - 6.0)$ and turbulent Mach numbers $(0.16 - 0.38)$ and studied their effect on the downstream turbulent statistics and change in length scales across the shock. Their study showed the need for a finer grid size in the post-shock region highlighting the under-resolved nature of the previous DNS studies of canonical STI. Wrinkling and breaking of the shock for various combinations of mean and turbulent Mach numbers was also studied in detail.

In his study, Donzis [63] defined a parameter $M_t/(M-1) \sim 0.6$ based on dimensional analysis, which differentiated between wrinkled and broken shock regime. A work in continuation by the same author [64] stated the ratio of laminar shock thickness to Kolmogorov length scale as a decisive parameter in predicting the amplification of various turbulent statistics as well as the nature of shock distortions. Larsson et al. [20] presented additional DNS cases with varying Reynolds number and investigated the effect of upstream Mach-, turbulent Mach- and Reynolds number on various turbulent statistics such as TKE amplification and post-shock anisotropy.

They also show for the first time that the influence of upstream Reynolds- and turbulent Mach number is minimal on the turbulence kinetic energy amplification.

Ryu and Livescu [57] carried out a high-resolution DNS study to resolve the shock structure in canonical STI. They studied the effect of the turbulent Mach number on the post-shock streamwise and transverse Reynolds stresses, and on the transverse vorticity variance. The turbulent statistics were analysed for the upstream turbulent Mach number varying between 0.27-0.02, for a given upstream Mach- and Reynolds number. A recent work by Livescu and Ryu [65] featured shock-resolved DNS carried out at Taylor Reynolds number of 180, much higher than the previously considered values, and at upstream Mach number up to 10. The effect of the upstream Mach number on the downstream vortical structures was studied in detail.

2.3.4 RANS modelling

Sinha et al. [5] studied the amplification of turbulence kinetic energy in a canonical shock-turbulence interaction using the RANS approach. RANS models based on eddy viscosity assumption were shown to overpredict the TKE amplification across the shock. They modelled the damping effect of shock oscillation on the TKE amplification using linear interaction analysis results. Implementing the shock-unsteadiness effect improved the TKE amplification to match the DNS trend.

Veera and Sinha [6] considered the presence of incoming temperature fluctuation to model the TKE amplification in canonical shock-turbulence interaction. A budget of the TKE equation was studied using LIA, and the dominant mechanism through which the upstream velocity-temperature correlation affects the TKE amplification were studied. These mechanisms were modelled using the linear theory results, and the final model correctly predicted the amplification of TKE in comparison with the DNS data.

Sinha [7] derived a transport equation for enstrophy in the canonical STI framework. Enstrophy, defined as the mean-square vorticity fluctuation, is directly related to the dissipation rate of turbulence kinetic energy ϵ. The dominant terms responsible for enstrophy amplification were identified and modelled using the linear theory, and the key physics was incorporated in the $k-\epsilon$

framework. The new model predicted the correct amplification in the dissipation rate across the shock for varying upstream Mach number.

Sinha and Balasridhar [66] studied the numerical error arising in the modelled transport equation for k and ϵ applied to canonical shock-turbulence interaction. The error was associated with the nonconservative nature of the source terms in the k and ϵ equations. This error was studied as a function of shock strength, grid resolution and upstream turbulence level. The model equations were then cast into equivalent conservative forms; significant improvement in the model predictions were observed, with the results matching the DNS data and the linear theory.

2.3.5 Application of shock-unsteadiness model to SBLI

The modelling insights obtained in the canonical STI configuration have proven useful in modelling the shock/boundary-layer interactions. Sinha et al. [40] implemented the shock- unsteadiness model [5] in a RANS simulation of a high-speed flow over a compression corner. The production term of the TKE equation was modified in three models, $k-\epsilon$, $k-\omega$ and Spalart-Allmaras, based on the shock-unsteadiness factor. The damping effect of this added flow physics on the TKE amplification led to a correct prediction of the separation region size, wall pressure and skin friction coefficient.

Pasha and Sinha [38] applied the shock-unsteadiness model to the case of an oblique shock interacting with a turbulent boundary layer. The highlight of this work was the implementation of the shock-unsteadiness correction in the presence of multiple shock- and expansion waves. The new model showed an appreciable improvement in the separation region size and the wall pressure prediction over conventional RANS model. Pasha and Sinha [8] studied the hypersonic cone-flare configuration using the shock-unsteadiness model; they considered different flare angles and free stream Mach numbers for the study. The unsteadiness correction was applied to SA and $k-\omega$ model, and significant improvement in the separation size and wall pressure predictions was observed; a modest improvement in the wall heat flux was also seen as compared with the conventional $k-\omega$ model.

Sinha [7] used the insight obtained in modelling the dissipation rate in canonical STI to study the SBLI at a compression corner. The modified SA model showed improved result over the previous shock-unsteadiness correction in predicting the separation region size and the wall pressure. Fedorova and Fedorchenko [67] considered the case of oblique shock impingement on a turbulent boundary layer, and modelled the effect of shock-unsteadiness by varying the conditions at the inlet of the computational domain. Computations were performed to simulate varying shock frequencies and amplitude of oscillation. A modest improvement in the the Stanton number distribution was observed with increasing amplitude of shock oscillation.

Chapter 3

Methodology

3.1 Introduction

Canonical shock-turbulence turbulence interaction (STI) considered in this work involves a steady, one-dimensional, uniform flow carrying vortical turbulence, which is homogeneous and isotropic in nature. Here, the term 'vortical turbulence' indicates flow with vortical perturbations and negligible thermodynamic fluctuations. This turbulence can be viewed as a superposition of two-dimensional planar waves (Fourier modes) with varying wavenumbers and frequencies. A

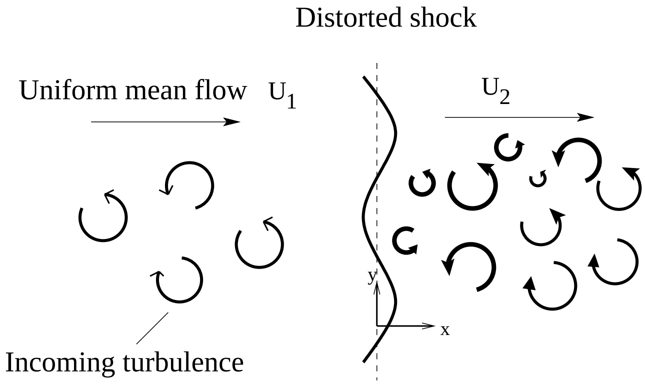

FIGURE 3.1: Schematic shows an incoming turbulence carried by a one-dimensional uniform mean velocity U_1 interacts with a normal shock; the shock gets distorted about a mean location, and the turbulence is amplified as it passes through the shock.

schematic of such a flow is shown in figure 3.1. This problem displays a host of flow phenomena across the shock such as amplification of turbulence kinetic energy, anisotropy, generation of acoustic energy and modification of turbulence length scales.

In this report, we study the turbulent energy flux correlation in the STI framework. As mentioned earlier, turbulent energy flux is an important unclosed term in the Reynolds-averaged Navier-Stokes (RANS) equation. Derivation of the RANS equation from the Navier-Stokes equations, along with the procedure of averaging is described in section 3.2. A detailed description of the LIA, one of the prominent tools of theoretical investigation of STI, is provided in section 3.3. Direct numerical simulation (DNS) has been the most reliable tool in studying STI as it captures all scales of turbulence, thus representing the flow physics accurately. Extensive DNS studies have been carried out in the recent past by several researchers as described in chapter 2. The results of the theoretical analysis in the current work have been compared with results of Larsson et al. [20], who studied large number of STI cases with varying upstream mean Mach number, turbulent Mach number and Reynolds number. Details of this DNS data is presented in section 3.4.

3.2 Governing equations

3.2.1 Instantaneous Navier-Stokes equations

The governing equations for fluid flow are

$$\frac{\partial \rho}{\partial t} + \frac{\partial(\rho u_i)}{\partial x_i} = 0, \tag{3.1}$$

$$\frac{\partial}{\partial t}(\rho u_i) + \frac{\partial}{\partial x_j}(\rho u_i u_j) = -\frac{\partial p}{\partial x_i} + \frac{\partial \tau_{ij}}{\partial x_j}, \tag{3.2}$$

$$\frac{\partial E}{\partial t} + \frac{\partial}{\partial x_j}\left[u_j E\right] = -\frac{\partial}{\partial x_j}\left[u_j p\right] + \frac{\partial}{\partial x_j}(u_i \tau_{ij}) - \frac{\partial q_j}{\partial x_j}, \tag{3.3}$$

where (3.1), (3.2) and (3.3) correspond to the conservation of mass, momentum and total energy, and are derived per unit volume of the fluid. ρ represents the density and u_i represents the velocity along the x_i coordinate. p represents the pressure and τ_{ij} is the viscous stress tensor given by

$$\tau_{ij} = 2\mu\hat{s}_{ij} + \eta\frac{\partial u_k}{\partial x_k}\delta_{ij},$$

where $\hat{s}_{ij}$ is the instantaneous strain rate denoted as $\hat{s}_{ij} = 1/2(\partial u_i/\partial x_j + \partial u_j/\partial x_i)$, η is the second viscosity ($\eta = -2/3\mu$, μ being the dynamic viscosity) and δ_{ij} is the Kronecker's delta. E represents the total energy given by $E = \rho e + (1/2)\rho u_i u_i$, where e is the internal energy given by $e = c_v T$. c_v is the specific heat at constant volume and T is the temperature. $\rho u_i u_i/2$ represents the kinetic energy and q_j is the heat flux vector along the x_j direction.

The first term of the above three equations represents the time rate of change of mass, momentum and total energy of a fluid element. The second term on the left-hand side (LHS) of the above equations represents the net flux of mass, momentum and energy across the fluid element boundary. This term is also known as the convection term. The pressure term existing in the momentum conservation equation represents the force exerted on the fluid element due to the difference in the pressure acting at its boundaries. Similarly, the pressure term in the energy conservation equation represents the rate of work done on the fluid element due to net pressure change at the boundary. The viscous stress term in momentum conservation equation represents the force exerted on the fluid element due to the normal and shear stresses acting at its boundary. The viscous stress term in the energy conservation equation similarly represents the rate of work done on the fluid element due to the normal and shear stresses acting at its boundary. The last term in the energy conservation equation i.e. $\partial q_j/\partial x_j$ represents the net heat flux due to conduction at the boundary of the fluid element.

3.2.2 Averaging

For any instantaneous flow variable f in a turbulent flow,

$$f = \overline{f} + f',$$

where $\overline{f}$ is the mean component and f' is the fluctuation about the mean. The mean component can be obtained by averaging over a sample space. One form of averaging is Reynolds averaging, which can be classified into time, ensemble and spatial averaging. For a turbulent flow having a steady mean component, time averaging can be applied to obtain the averaged value over a specified time interval. For an instantaneous variable $f(\mathbf{x}, t)$, the time-averaged mean value is given by

$$\overline{f}(\mathbf{x}) = \lim_{T\to\infty} \frac{1}{T} \int_{t}^{t+T} f(\mathbf{x}, t)dt,$$

where overbar represents Reynolds averaging, and T is the time interval over which the mean value is calculated. This averaging is generally employed in an incompressible flow, where the number of unclosed correlations in the averaged conservation equations are lesser compared to its compressible counterpart. For compressible flows, any instantaneous variable $f(\mathbf{x}, t)$ can be decomposed as $f(\mathbf{x}, t) = \widetilde{f} + f''$, where $\widetilde{f}$ is the mass-weighted (Favre) average given by

$$\widetilde{f}(\mathbf{x}) = \frac{1}{\overline{\rho}} \lim_{T\to\infty} \frac{1}{T} \int_{t}^{t+T} \rho(\mathbf{x}, t) f(\mathbf{x}, t)dt,$$

and f'' is the Favre fluctuation [68].

3.2.3 Reynolds-averaged Navier-Stokes equations

In order to derive the averaged Navier-Stokes equations, we first write the flow variables in terms of their mean and fluctuating components, i.e.

$$\begin{aligned} \rho &= \overline{\rho} + \rho', \\ p &= \overline{p} + p', \\ u_i &= \widetilde{u}_i + u_i'', \\ T &= \widetilde{T} + T''. \end{aligned}$$

Substituting the above equations into (3.1) and (3.2), and averaging yields

$$\frac{\partial \overline{\rho}}{\partial t} + \frac{\partial (\overline{\rho}\widetilde{u}_i)}{\partial x_i} = 0, \tag{3.5}$$

$$\frac{\partial}{\partial t}(\overline{\rho}\widetilde{u}_i) + \frac{\partial}{\partial x_j}(\overline{\rho}\widetilde{u}_i\widetilde{u}_j) = -\frac{\partial \overline{p}}{\partial x_i} + \frac{\partial}{\partial x_j}\left[\overline{t}_{ij} - \overline{\rho u_j'' u_i''}\right], \tag{3.6}$$

which represent the Reynolds-averaged mass- and momentum conservation equations, respectively. These equations are similar to their instantaneous counterparts except that the instantaneous variables are replaced by the corresponding averaged values. The only term dissimilar from the instantaneous momentum conservation equation is $-\overline{\rho u_j'' u_i''}$. This term represents turbulent mixing caused due to the turbulent momentum being convected by the fluctuating velocity. In analogy with the viscous stress, where the stress induced is due to molecular momentum flux across layers, the stress caused due to the flux of the turbulent momentum is termed as Reynolds stress, and $-\overline{\rho u_j'' u_i''}$ is known as Reynolds stress tensor. It is also represented as $\overline{\rho}\tau_{ij}$ where τ_{ij} is $-\widetilde{u_i'' u_j''}$.

Similarly, upon averaging the instantaneous energy equation (3.3), we get

$$\begin{aligned}\frac{\partial \widetilde{E}}{\partial t} + \frac{\partial}{\partial x_j}\left[\widetilde{u}_j\widetilde{E}\right] = &- \frac{\partial}{\partial x_j}(\overline{p}\widetilde{u}_j) + \frac{\partial}{\partial x_j}\left[-\overline{q}_j - \gamma\overline{\rho u_j'' e''} + \overline{t_{ji}u_i''} - \overline{\rho u_j'' \frac{1}{2} u_i'' u_i''}\right] \\ &+ \frac{\partial}{\partial x_j}\left[\widetilde{u}_i(\overline{t}_{ij} - \overline{\rho u_i'' u_j''})\right],\end{aligned} \tag{3.7}$$

where $\widetilde{E}$ is the averaged total energy given by $\widetilde{E} = \overline{\rho}(\widetilde{e} + \frac{1}{2}\widetilde{u}_i\widetilde{u}_i + \frac{1}{2}\widetilde{u_i'' u_i''})$, which represents the sum of average internal energy, the average mean kinetic energy and the turbulence kinetic energy k. Several terms in this equation are similar to the instantaneous energy conservation equation, with the instantaneous values being replaced by the averaged values.

In the mean energy conservation equation, both the terms on the LHS have analogous terms in the instantaneous energy conservation equation. Also, the terms on the right-hand side (RHS) such as $\partial(\overline{p}\widetilde{u}_j)/\partial x_j$, $\partial\overline{q_j}/\partial x_j$ and $\partial(\widetilde{u}_i\overline{t}_{ij})/\partial x_j$, represent the effect of pressure, heat conduction and viscous stress respectively, and bear analogy to the corresponding terms in the instantaneous energy conservation equation. Apart from these averaged quantities, the energy conservation equation also has additional fluctuation terms such as $\overline{\rho u_j'' e''}$, which represents convection of turbulent internal energy e'', by fluctuating velocity u_j''. This term signifies turbulent mixing of heat, and is denoted as turbulent energy flux vector; this term is the highight of the current study.

The triple velocity correlation term containing $\overline{u_j''\left(\frac{1}{2}\rho u_i'' u_i''\right)}$ represents the convection of kinetic energy $\left(\frac{1}{2}\rho u_i''u_i''\right)$, by fluctuating velocity u_j'', and corresponds to the turbulent diffusion effect. This term can also be written as $\overline{\left(\frac{1}{2}\rho u_i''u_j''\right) u_i''}$, which represents the correlation between the turbulent stress tensor $\left(\frac{1}{2}\rho u_i''u_j''\right)$ and the fluctuating velocity u_i''. The term containing $\overline{t_{ji}u_i''}$ represents correlation between the viscous stress tensor t_{ji} and the fluctuating velocity u_i''. It is analogous to the molecular diffusion term and can therefore be suitably termed as turbulent diffusion term. The last term in the averaged energy conservation equation represents the rate of work done on the fluid element volume due to the Reynolds stress.

The turbulent correlations in equations (3.5), (3.6) and (3.7) represent various physical processes as described above. In Reynolds-averaged Navier-Stokes (RANS) modelling, the physical effect of these correlations on the mean quantities is modelled in terms of the mean variables and appropriate closure coefficients derived from experiments or direct numerical simulation. For example, Reynolds stress -$\overline{\rho u_i''u_j''}$ is modelled as

$$\overline{\rho}\tau_{ij} = -\overline{\rho u_i''u_j''} = 2\mu_T \left(S_{ij} - \frac{1}{3}\frac{\partial \widetilde{u}_k}{\partial x_k}\delta_{ij} \right) - \frac{2}{3}\overline{\rho}k\delta_{ij}.$$

Here, eddy viscosity μ_T is given by

$$\mu_T = C_\mu^0 \rho k^2/\epsilon, \tag{3.8}$$

where $C_\mu^0 = 0.09$ is a closure constant, k is the turbulent kinetic energy, ϵ is the dissipation rate and S_{ij} is the mean strain rate. Similar closure models are proposed for all turbulent correlations in order to solve the set of governing equations.

The turbulent energy flux is also modelled using the gradient diffusion hypothesis as

$$\overline{u''e''} = -\frac{\kappa_T}{\overline{\rho}}\frac{\partial \widetilde{T}}{\partial x}. \tag{3.9}$$

Thermal conductivity κ_T is given by $\kappa_T = \mu_T c_v / Pr_T$, where Pr_T represents the turbulent Prandtl number having a constant value of 0.89 as per Morkovin's hypothesis as shown below.

3.2.4 Morkovin's hypothesis

In a two-dimensional steady compressible boundary layer, the equation for total enthalpy can be written as [69]

$$\rho u\frac{\partial H}{\partial x} + \rho v\frac{\partial H}{\partial y} = \frac{\partial}{\partial y}\left(\frac{\mu}{Pr}\frac{\partial H}{\partial y}\right) + \frac{\partial}{\partial y}\left[\left(1 - -\frac{1}{Pr}\right)\mu u\frac{\partial u}{\partial y}\right], \tag{3.10}$$

where the total enthalpy $H = h + u^2/2$. An approximate assumption for gases would be to consider the Prandtl number equal to unity. This yields a particular solution $H =$ Const. through out the boundary layer. Thus an expression for total temperature fluctuations can be written as

$$T_t'' = T'' + \frac{\widetilde{u}u''}{C_p} = 0. \tag{3.11}$$

From the above equation we can obtain

$$\frac{T''}{\widetilde{T}} = -(\gamma - 1)M^2\frac{u''}{\widetilde{u}},$$

which can alternately be expressed as

$$\frac{\sqrt{\widetilde{T''^2}}}{\widetilde{T}} = -(\gamma - 1)M^2\frac{\sqrt{\widetilde{u''^2}}}{\widetilde{u}}. \tag{3.12}$$

Also from (3.10), we can write

$$\sqrt{\widetilde{T_t''^2}} = \sqrt{\widetilde{\left(T'' + \frac{\widetilde{u}}{C_p}u''\right)^2}},$$

i.e.

$$\sqrt{\widetilde{T_t''^2}} = \left[\widetilde{T''^2} + \frac{\widetilde{u}^2}{C_p^2}\widetilde{u''^2} + 2\frac{\widetilde{u}}{C_p}\widetilde{u''T''}\right]^{1/2}. \tag{3.13}$$

From (3.10) and (3.13), we get

$$\sqrt{\widetilde{T_t''^2}} = \left[2\widetilde{T''^2} + 2\widetilde{T''^2}R_{uT}\right]^{1/2},$$

where $R_{uT} = \widetilde{u''T''} / \left(\sqrt{\widetilde{u''^2}} \sqrt{\widetilde{T''^2}} \right)$. Under the assumption of total temperature fluctuations being negligible, we obtain

$$R_{uT} = -1. \tag{3.14}$$

Also from (3.10),

$$\widetilde{v''T''} = -\frac{\widetilde{u}}{C_p} \widetilde{u''v''}. \tag{3.15}$$

(3.12), (3.14) and (3.15) represent a set of equations termed as strong Reynolds analogy (SRA) and were specified by Morkovin [9]. They have been validated both experimentally and numerically [70].

Turbulent Prandtl number Pr_T is given by

$$Pr_T = \frac{\widetilde{u''v''} \left(\frac{\partial \widetilde{T}}{\partial y} \right)}{\widetilde{v''T''} \left(\frac{\partial \widetilde{u}}{\partial y} \right)}, \tag{3.16}$$

which represents the ratio of turbulent transport of heat to the turbulent transport of momentum. From (3.15) and (3.16) we can obtain

$$Pr_T = \frac{-C_p \left(\frac{\partial \widetilde{T}}{\partial y} \right)}{\widetilde{u} \left(\frac{\partial \widetilde{u}}{\partial y} \right)}. \tag{3.17}$$

Also from our assumption of total enthalpy being constant in the boundary layer, its derivative along wall normal direction yields

$$\frac{\left(\frac{\partial \widetilde{T}}{\partial y} \right)}{\left(\frac{\partial \widetilde{u}}{\partial y} \right)} = -\frac{\widetilde{u}}{C_p}. \tag{3.18}$$

From (3.17) and (3.18) we obtain a value of $Pr_T = 1$. A value of $Pr_T = 0.89$ is found to be suitable for boundary-layer computations, and is generalized to other flows as well.

3.3 Linear Interaction Analysis

The heart of the theoretical analysis is the mathematical description of a planar wave interacting with a normal shock. The procedure adopted here follows the work of Mahesh et al. [19], and the parts that are directly relevant to the current work are presented for completeness. An alternative compact formulation of LIA is presented by Fabre et al. [54].

Linear interaction analysis is based on the assumption that the turbulent fluctuations are small compared to the jump in mean flow quantities across the shock. Ryu and Livescu [57] argued that the deviation from the LIA limit can be quantified by the ratio

$$\frac{\delta}{\eta} = 7.69 \frac{M_t}{M_1 - 1} \frac{1}{\sqrt{Re_\lambda}}, \tag{3.19}$$

where δ is the estimated laminar shock thickness, η is the estimated Kolmogorov length scale, and Re_λ is the Reynolds number based on the Taylor microscale. They then showed how DNS results converged towards the LIA predictions as δ/η was reduced. A slightly different view was taken by Larsson et al. [20], who found excellent agreement between LIA and DNS (for turbulence amplification) even at relatively high values of δ/η (and relatively strong turbulence) once the viscous decay behind the shock was compensated for. This suggests that the viscous effects may be more important than nonlinear effects, at least in the context of the amplification of turbulence kinetic energy. The main conclusion in the context of the present study is that LIA can be expected to be reasonably accurate, but that we should expect discrepancies between the LIA and DNS due to the substantial viscous effects in the latter.

3.3.1 Linearised Euler equations

Consider a three-dimensional turbulent flow field convected by a uniform mean flow. Assuming negligible viscous effects, the instantaneous governing equations can be written as

$$\frac{\partial \rho}{\partial t} + \frac{\partial}{\partial x_i}(\rho u_i) = 0, \tag{3.20}$$

$$\frac{\partial}{\partial t}(\rho u_i) + \frac{\partial}{\partial x_j}(\rho u_i u_j) = -\frac{\partial p}{\partial x_i}, \tag{3.21}$$

$$\frac{\partial E}{\partial t} + \frac{\partial E u_i}{\partial x_i} = -\frac{\partial p u_i}{\partial x_i}, \tag{3.22}$$

where (3.20), (3.21) and (3.22) are the equations for conservation of mass, momentum and energy, respectively.

For a weakly turbulent flow, the mass and the momentum conservation equations can be linearised about the mean flow to give

$$\frac{\partial \rho'}{\partial t} + U_i \frac{\partial \rho'}{\partial x_i} = -\overline{\rho}\left(\frac{\partial u_i'}{\partial x_i}\right), \tag{3.23}$$

$$\frac{\partial u_j'}{\partial t} + U_i \frac{\partial u_j'}{\partial x_i} = -\frac{1}{\overline{\rho}}\frac{\partial p'}{\partial x_j}, \tag{3.24}$$

where U is the mean velocity in x_1 direction. Here, $'$ represents the Reynolds fluctuation and overbar represents the Reynolds average. Conventional Reynolds averaging is used, instead of Favre averaging for compressible flows, because the difference between the two is negligible in the linear framework.

The instantaneous equation of state is given by $p = \rho R T$, where R represents the specific gas constant. Linearising this equation about the mean variables, we obtain

$$\frac{p'}{\overline{p}} = \frac{\rho'}{\overline{\rho}} + \frac{T'}{\overline{T}}. \tag{3.25}$$

The Gibbs equation for entropy can be written as $Tds = dh - Vdp$ where ds represents the change in entropy s, dh represents the change in enthalpy h, V is the specific volume and dp represents the change in pressure. This equation can also be written as

$$\frac{s'}{C_p} = \frac{p'}{\gamma \overline{p}} - \frac{\rho'}{\overline{\rho}}. \tag{3.26}$$

Linearising (3.22) and combining with (3.26), we obtain

$$\frac{\partial s'}{\partial t} + U_i \frac{\partial s'}{\partial x_i} = 0, \tag{3.27}$$

which represents the governing equation for entropy fluctuation. Equations (3.23), (3.24), (3.25), (3.26) and (3.27) are known as linearised Euler equations and govern the fluctuations in a one-dimensional weakly turbulent flow.

3.3.2 Kovasznay modes

Kovasznay [41] showed that for a weakly turbulent flow field being carried by a one-dimensional compressible supersonic mean flow, the turbulence can be decomposed into three distinct disturbance fields governed by three independent differential equations. He named these three "modes" as vorticity, entropy and sound-wave (acoustic) mode. These modes were shown to propagate independently without interacting with each other at low turbulence intensity levels. The three differential equations for these modes can be derived from the linearised Euler equations.

From (3.24) we can derive

$$\frac{\partial}{\partial t}\omega_i' + U\frac{\partial \omega_i'}{\partial x_j} = 0, \tag{3.28}$$

where ω_i is the vorticity along i^{th} direction and is given by $\omega_i = 1/2(\partial u_i/\partial x_j - \partial u_j/\partial x_i)$. Also from (3.23), (3.24) and (3.26), we can derive an equation governing the pressure fluctuations given by

$$\frac{\partial^2 p'}{\partial t^2} + 2U\frac{\partial^2 p'}{\partial x \partial t} - (a^2 - U^2)\frac{\partial^2 p'}{\partial x^2} = 0, \tag{3.29}$$

where a represents the speed of sound.

(3.28), (3.27) and (3.29) can be rewritten as

$$\frac{D}{Dt}(\overline{\omega_i'\omega_i'}) = 0, \tag{3.30}$$

$$\frac{D\overline{s'^2}}{Dt} = 0, \tag{3.31}$$

$$\frac{D}{Dt}\left(\frac{\overline{p'^2}}{2}\right) = -2\gamma\overline{p}\ \overline{p'\frac{\partial u_j'}{\partial x_j}}. \tag{3.32}$$

(3.30), (3.31) and (3.32) are the governing equations for vorticity, entropy and pressure variance. (3.30) and (3.31) show that the vorticity and entropy fluctuations vary independently in the flow and are convected by the uniform mean velocity. (3.32) shows that the rate of change of pressure variance in linear limit is governed by the mean pressure and the correlation between pressure fluctuation and dilatation. Also, the pressure fluctuations are carried at a speed of sound a relative to the mean flow.

From this analysis it is clear that, the velocity fluctuations have independent contributions from the vorticity and the acoustic mode. While the vorticity mode contributes to the rotational component of velocity which is solenoidal in nature, the acoustic mode contributes to the dilatational part of velocity which is irrotational. Temperature and density fluctuations have independent contributions from the acoustic and entropy modes, and pressure fluctuation has contribution from the acoustic mode alone.

3.3.3 Single wave analysis

3.3.3.1 *Incoming purely vortical turbulence*

Consider an incoming purely vortical disturbance that has contribution from vorticity mode alone, i.e., the upstream flow has only solenoidal velocity fluctuations and the thermodynamic fluctuations p_1', ρ_1' and T_1', corresponding to upstream pressure, density and temperature, are assumed to be identically zero. The solenoidal velocity fluctuations associated with the vorticity mode therefore satisfy the linearized Euler equation (3.23),

$$\frac{\partial u_i'}{\partial x_i} = 0. \tag{3.33}$$

One such two-dimensional planar vorticity wave interacting with a nominally normal shock is shown in figure 3.2.

This wave is characterized by a wavenumber k, an angle of incidence ψ and a complex amplitude A_v. The velocity fluctuations in the x and y directions satisfying (3.33) are given by

$$\frac{u_1'}{U_1} = A_v l e^{ik(xm+yl-U_1tm)}, \tag{3.34a}$$

$$\frac{v_1'}{U_1} = -A_v m e^{ik(xm+yl-U_1tm)}, \tag{3.34b}$$

where $l = \sin\psi$, $m = \cos\psi$ and U_1 is the mean velocity upstream of the shock wave. Upon interaction, the shock distorts from its mean position; the unsteady distorted shock wave is given

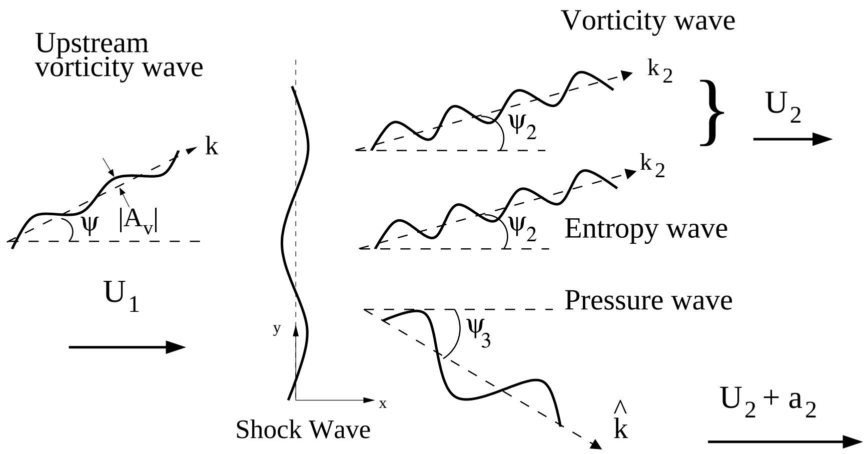

FIGURE 3.2: A single vortical wave interacts with a shock to yield three waves downstream of the shock.

by $\xi(y,t)$. The temporal derivative of the shock deviation ξ_t represents the local streamwise velocity of the shock wave, and the transverse derivative ξ_y describes the angular distortion of the shock.

Ribner [17, 18] showed that in a linear framework, a single vortical wave interacting with the shock gives rise to all three independent disturbance waves namely the vorticity, entropy and acoustic waves as shown in figure 3.2. The generation of these additional disturbances are governed by linearized Rankine-Hugoniot (RH) equations which relate the shock-upstream fluctuations (subscript 1) to the shock-downstream fluctuations (subscript 2).

Rankine-Hugoniot conditions

The instantaneous RH equations are given by

$$\rho_1 u_{n1} = \rho_2 u_{n2}, \tag{3.35a}$$

$$p_1 + \rho_1 u_{n1}^2 = p_2 + \rho_2 u_{n2}^2, \tag{3.35b}$$

$$u_{\hat{t}1} = u_{\hat{t}2}, \tag{3.35c}$$

$$h_1 + \frac{u_{n1}^2}{2} = h_2 + \frac{u_{n2}^2}{2}. \tag{3.35d}$$

Here, u_n and $u_{\hat{t}}$ represent the instantaneous velocities normal and tangential to the moving shock. h is the enthalpy given by C_pT, where C_p is the specific heat at constant pressure. In the inertial frame of reference u_n and $u_{\hat{t}}$ can be written as

$$u_n = U + u' - \xi_t, \tag{3.36a}$$

$$u_{\hat{t}} = v' + U\xi_y. \tag{3.36b}$$

Substituting the above equations in (3.35) and writing the flow variables in terms of their mean and fluctuating components, we obtain

$$(\overline{\rho}_1 + \rho_1')(U_1 + u_1' - \xi_t - (v_1' + U_1\xi_y)) = (\overline{\rho}_2 + \rho_2')(U_2 + u_2' - \xi_t - (v_2' + U_2\xi_y)), \tag{3.37a}$$

$$\begin{aligned}\overline{p}_1 + p_1' + (\overline{\rho}_1 + \rho_1')(U_1 + u_1' - \xi_t - (v_1' + U_1\xi_y))^2 = \\ \overline{p}_2 + p_2' + (\overline{\rho}_2 + \rho_2')(U_2 + u_2' - \xi_t - (v_2' + U_2\xi_y))^2,\end{aligned} \tag{3.37b}$$

$$(U_1 + u_1' - \xi_t)\xi_y + v_1' = (U_2 + u_2' - \xi_t)\xi_y + v_2', \tag{3.37c}$$

$$\begin{aligned}C_p(\overline{T}_1 + T_1') + \frac{1}{2}((U_1 + u_1') - \xi_t)^2 + (v_1' + U_1\xi_y)^2 - 2(U_1 - u_1' - \xi_t)(v_1' + U_1\xi_y) = \\ C_p(\overline{T}_2 + T_2') + \frac{1}{2}((U_2 + u_2') - \xi_t)^2 + (v_2' + U_2\xi_y)^2 - 2(U_2 - u_2' - \xi_t)(v_2' + U_2\xi_y).\end{aligned} \tag{3.37d}$$

Linearising the above set of equations about the mean value and rearranging, we get

$$\frac{u_2' - \xi_t}{U_1} = B\left(\frac{u_1' - \xi_t}{U_1}\right) + \check{B}\left(\frac{T_1'}{\overline{\overline{T}}_1}\right), \tag{3.38a}$$

$$\frac{v_2'}{U_1} = \frac{v_1'}{U_1} + E\xi_y, \tag{3.38b}$$

$$\frac{\rho_2'}{\overline{\overline{\rho}}_2} = C\left(\frac{u_1' - \xi_t}{U_1}\right) - \check{C}\left(\frac{T_1'}{\overline{\overline{T}}_1}\right), \tag{3.38c}$$

$$\frac{p_2'}{\overline{\overline{p}}_2} = D\left(\frac{u_1' - \xi_t}{U_1}\right) - \check{D}\left(\frac{T_1'}{\overline{\overline{T}}_1}\right), \tag{3.38d}$$

where

$$B = \frac{(\gamma-1)M_1^2 - 2}{(\gamma+1)M_1^2}, \qquad \check{B} = \frac{2}{(\gamma+1)M_1^2}, \qquad E = \frac{2(M_1^2-1)}{(\gamma+1)M_1^2}, \tag{3.39a}$$

$$C = \frac{4}{(\gamma-1)M_1^2 + 2}, \qquad \check{C} = \frac{(\gamma-1)M_1^2 + 4}{(\gamma-1)M_1^2 + 2}, \tag{3.39b}$$

$$D = \frac{4\gamma M_1^2}{2\gamma M_1^2 - (\gamma-1)}, \qquad \check{D} = \frac{2\gamma M_1^2}{2\gamma M_1^2 - (\gamma-1)}, \tag{3.39c}$$

M_1 being the upstream Mach number. Note that for purely vortical upstream disturbance, the second term on the right hand side of (3.38a), (3.38c) and (3.38d) is essentially zero ($T_1' = 0$).

Nature of the downstream acoustic wave

The fluctuations in the flow variables downstream of the shock are governed by the linearized Euler equations (3.23) - (3.27). A governing equation for pressure fluctuation obtained from these equations is shown in (3.29). The pressure wave downstream of the shock can be modelled as [19]

$$p' = F(x)e^{(ik(ly - mU_1 t)} \tag{3.40}$$

where $F(x)$ represents the x component of the exponential waveform. Note that the transverse wavenumber as well as the frequency is same as the upstream vorticity wave satisfying the continuity equation. The pressure fluctuation is modelled as a planar waveform by considering $F(x) = \exp(i\widetilde{k}x)$, where $\widetilde{k}$ is the streamwise wavenumber. Substituting this waveform in (3.29) gives

$$\left[\frac{a_2^2}{U_1^2} - \frac{U_2^2}{U_1^2}\right]\tilde{k}^2 + 2km\frac{U_2}{U_1}\tilde{k} - k^2\left[m^2 - l^2\frac{a_2^2}{U_1^2}\right] = 0. \tag{3.41}$$

From the above equation it can be seen that $\widetilde{k}$ takes real values only when

$$\psi < \tan^{-1}\left(\frac{1}{\sqrt{\left(\frac{a_2^2}{U_1^2} - \frac{U_2^2}{U_1^2}\right)}}\right). \tag{3.42}$$

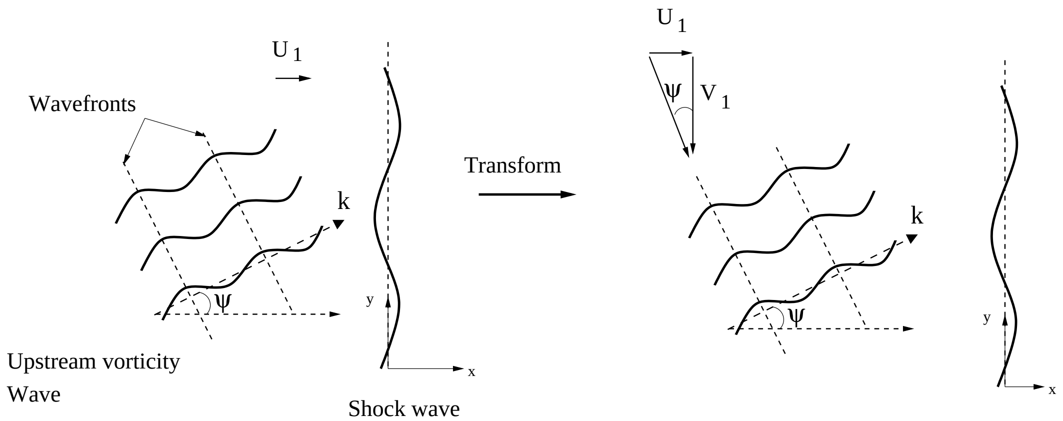

FIGURE 3.3: An unsteady problem of upstream vorticity wave interacting with a normal shock, transformed into a steady interaction with an oblique shock.

Therefore, there exists a critical angle ψ_c above which the streamwise acoustic wavenumber $\widetilde{k}$ assumes a complex value. The acoustic waveform can therefore be written as

$$p' = e^{i\widetilde{k}x} e^{ik(ly - mU_1 t)}, \quad \psi < \psi_c, \tag{3.43a}$$

$$p' = e^{-\widetilde{k}_i x} e^{i\widetilde{k}_r x} e^{ik(ly - mU_1 t)}, \quad \psi > \psi_c. \tag{3.43b}$$

The pressure fluctuation decays exponentially at a rate governed by $\widetilde{k}_i$ when $\psi > \psi_c$ and propagate without decay when $\psi < \psi_c$.

A physical insight into the pressure wave propagation can be gained by considering the transformation suggested by Ribner [17], in which the unsteady interaction of a plane vorticity wave with a normal shock, is transformed into an equivalent steady interaction of the disturbance wave with an oblique shock. This is achieved by adding a mean velocity component, such that the total mean velocity is in the direction parallel to the wavefronts as shown in figure 3.3. In the transformed problem, the shock wave makes an angle ψ with the upstream mean flow, and the flow downstream of the shock can be either subsonic or supersonic depending on the value of ψ. The nature of the acoustic field will change dramatically between these cases.

For small angles ψ (for a fixed M_1), the flow behind the shock is supersonic in the transformed problem. The acoustic waves generated downstream of the shock propagate radially at the speed of sound, while they are convected by the local fluid velocity. A conical pattern of the downstream disturbance is thus formed, as sketched in figure 3.4(a), and the common tangent

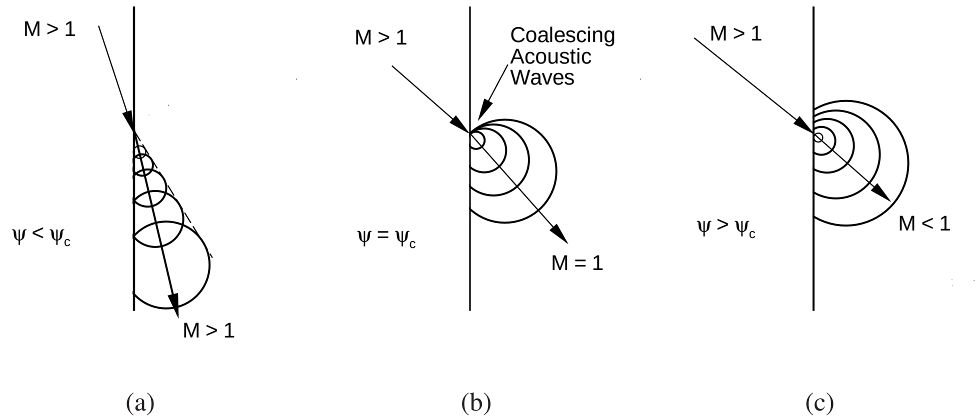

FIGURE 3.4: The acoustic wave patterns downstream of the shock in the transformed coordinate system for three upstream wave angles: (a) $\psi < \psi_c$ (propagating regime); (b) $\psi = \psi_c$ (critical angle); and (c) $\psi > \psi_c$ (decaying regime).

to the circular wave patterns represents the wavefront of the acoustic disturbance. The two-dimensional planar wavefronts propagate with a constant amplitude in the downstream region. This qualitative behaviour is termed as "propagating regime".

For large values of ψ, the flow downstream of the shock is subsonic in the transformed problem. The acoustic waves generated at the shock expand radially outwards at sonic speed while being convected subsonically; this is sketched in figure 3.4(c). The ever expanding circles do not add up along a common tangent, and the amplitude of the acoustic wave decays with distance from the shock. This regime is therefore termed as "decaying regime".

For every upstream Mach number M_1, there exists a critical angle $\psi = \psi_c$, for which the downstream transformed flow is sonic. Geometrically, this is given as [17]

$$\psi_c = \tan^{-1}\left(\frac{rM_2}{\sqrt{1 - M_2^2}}\right), \tag{3.44}$$

where M_2 is the downstream Mach number in the original unsteady (i.e., normal shock) problem and r is the compression ratio. The acoustic waves at the critical angle are sketched in figure 3.4(b). For such a case, the pressure wave patterns not only propagate radially outward with a speed of sound, but are also convected at that speed. The downstream acoustic disturbances therefore accumulate at the shock, leading to high values of downstream fluctuations, including local shock speed and distortion.

Nature of the downstream vorticity/entropy wave

Similar to the upstream vorticity wave, the downstream vorticity and entropy waves are plane waves convected by the downstream mean velocity U_2. They assume the form

$$e^{i\bar{k}x}e^{ik(ly-mU_1t)}, \tag{3.45}$$

where $\overline{k}$ is the streamwise wavenumber of the vorticity/entropy wave. In order to find out $\overline{k}$, the following dispersion relation correlating the upstream and downstream streamwise wavenumbers is used

$$\begin{aligned} \omega &= U_1 km = U_2\overline{k}, \\ \overline{k} &= km\frac{U_1}{U_2} = kmr. \end{aligned}$$

This clearly shows that there is an increase in the downstream wavenumber or decrease in the length scale of fluctuation proportional to r. Therefore, the downstream waveform for the vorticity and entropy wave can be written as

$$e^{ik(mrx+ly-mU_1t)}. \tag{3.46}$$

Final solution

The final waveform of the downstream fluctuating variables are

$$\frac{u_2'}{U_1} = A_v\left[\widetilde{F}e^{i\tilde{k}x}e^{ik(ly-mU_1t)} + \widetilde{G}e^{ik(mrx+ly-mU_1t)}\right], \tag{3.47a}$$

$$\frac{v_2'}{U_1} = A_v\left[\widetilde{H}e^{i\tilde{k}x}e^{ik(ly-mU_1t)} + \widetilde{I}e^{ik(mrx+ly-mU_1t)}\right], \tag{3.47b}$$

$$\frac{p_2'}{\bar{P}_2} = A_v\left[\widetilde{K}e^{i\tilde{k}x}e^{ik(ly-mU_1t)}\right], \tag{3.47c}$$

$$\frac{\rho_2'}{\bar{\rho}_2} = A_v\left[\frac{\widetilde{K}}{\gamma}e^{i\tilde{k}x}e^{ik(ly-mU_1t)} + \widetilde{Q}e^{ik(mrx+ly-mU_1t)}\right], \tag{3.47d}$$

$$\frac{T_2'}{\bar{T}_2} = A_v\left[\frac{\gamma-1}{\gamma}\widetilde{K}e^{i\tilde{k}x}e^{ik(ly-mU_1t)} + \widetilde{Q}e^{ik(mrx+ly-mU_1t)}\right], \tag{3.47e}$$

where $\widetilde{F}$, $\widetilde{H}$ and $\widetilde{K}$ are complex amplitudes associated with the acoustic mode. $\widetilde{G}$ and $\widetilde{I}$ correspond to the vorticity mode, and $\widetilde{Q}$ corresponds to the entropy mode. To obtain an expression for shock speed ξ_t, the waveforms for u_2' and u_1' are substituted in (3.38a) at $x = 0$ to yield

$$\frac{\xi_t}{U_1} = A_v \widetilde{L} e^{ik(ly - mU_1 t)}, \tag{3.48}$$

where $\widetilde{L}$ is the complex amplitude associated with the shock speed. Integrating the above equation and differentiating with y, we get the angular distortion ξ_y as which can be written as

$$\xi_y = -\frac{l}{m} A_v \widetilde{L} e^{ik(ly - mU_1 t)}. \tag{3.49}$$

In order to solve for the post-shock fluctuations, the downstream planar waveforms are substituted in the linearised Rankine-Hugoniot and linearised Euler equations to yield the value of the associated complex amplitudes. The solution obtained for the complex amplitude $\widetilde{L}$ associated with the shock-speed (3.48) is given by

$$\widetilde{L} = \frac{-\cos\psi - \beta D \sin\psi - r\alpha D \cos\psi + Br\cos\psi}{E\tan\psi - \beta D - r(1 - B + \alpha D)\cot\psi}, \tag{3.50}$$

where α and β are given by

$$\alpha = \frac{1}{\gamma M_2^2 r}\left[\frac{k_r}{r\cos\psi - k_r}\right], \quad \beta = \frac{1}{\gamma M_2^2 r}\left[\frac{\sin\psi}{r\cos\psi - k_r}\right]. \tag{3.51}$$

M_2 is the mean flow Mach number downstream of the shock, and $k_r = \widetilde{k}/k$ is the ratio of the streamwise wavenumber of the downstream acoustic wave to the wavenumber of the upstream vorticity wave. The nature of the acoustic wavenumber $\widetilde{k}$ varies based on the angle of incidence of the upstream vorticity wave relative to the critical angle ψ_c given by (3.44). For $0 < \psi < \psi_c$, $\widetilde{k}$ is real and is given by

$$\frac{\widetilde{k}}{k} = \frac{U_1}{U_2}\frac{M_2}{1 - M_2^2}\left[-M_2\cos\psi + \sin\psi\sqrt{cot^2\psi - \frac{U_2^2}{U_1^2}\left(\frac{1}{M_2^2} - 1\right)}\right].$$

For $\psi_c < \psi < \pi/2$, $\widetilde{k}$ is complex ($\widetilde{k} = \widetilde{k}_r + i\widetilde{k}_i$), and its real and imaginary parts are given by

$$\frac{\widetilde{k}_r}{k} = -\frac{U_1}{U_2}\frac{M_2^2}{1-M_2^2}\cos\psi,$$

and

$$\frac{\widetilde{k}_i}{k} = \frac{U_1}{U_2}\frac{M_2}{1-M_2^2}\sin\psi\sqrt{\frac{U_2^2}{U_1^2}\left(\frac{1}{M_2^2}-1\right)-\cot^2\psi}.$$

The complex coefficients corresponding to the downstream velocity and temperature fluctuations (see (3.47)) can be expressed in terms of $\widetilde{L}$ as

$$\widetilde{F} = \alpha D(\sin\psi - \widetilde{L}), \tag{3.52a}$$

$$\widetilde{G} = B\sin\psi + \widetilde{L}(1-B) - \widetilde{F}, \tag{3.52b}$$

$$\widetilde{K} = D(\sin\psi - \widetilde{L}), \tag{3.52c}$$

$$\widetilde{Q} = C(\sin\psi - \widetilde{L}) - \frac{\widetilde{K}}{\gamma}. \tag{3.52d}$$

Using the above complex amplitudes, the value of velocity and temperature fluctuations at any given point in the shock-downstream region can be defined, and the turbulent energy flux can thus be calculated using the expression

$$\overline{u_2'e_2'} = \left(\frac{1}{\gamma-1}\right)\frac{1}{U_1\overline{T}_2}\frac{\left[\overline{u_2'T_2'^*} + \overline{T_2'u_2'^*}\right]}{2(TKE_1/U_1^2)}. \tag{3.53}$$

This corresponds to a single planar wave upstream of the shock wave. The turbulent energy flux is normalized by the upstream turbulent kinetic energy TKE_1 as shown in the above equation, where

$$TKE_1 = \frac{1}{2}\left[\overline{u_1'^2} + \overline{v_1'^2}\right] = \frac{|A_v|^2}{2}U_1^2,$$

where $\overline{u_1'^2} = \overline{u_1'u_1'^*}$ and $\overline{v_1'^2} = \overline{v_1'v_1'^*}$; $*$ indicates the complex conjugate, with the expressions for u_1' and v_1' given in (3.34).

3.3.3.2 *Interaction of a vorticity-entropy wave with shock wave*

For a vorticity-entropy wave interacting with a normal shock, the upstream velocity fluctuations have the planar waveforms as given in (3.34). The upstream temperature fluctuations have the planar waveform as

$$\frac{T_1'}{\overline{T}_1} = -\frac{\rho_1'}{\overline{\rho}_1} = -A_e e^{ik(xm+yl-U_1 tm)}, \tag{3.54}$$

where A_e represents the complex amplitude for the upstream entropy wave. The linearised Rankine-Hugoniot equations relating the fluctuations upstream and downstream of the shock are given by (3.38), with finite T_1' present upstream of the shock.

The expression for the complex amplitude $\widetilde{L}$ taking into account the upstream entropy fluctuations can be written as

$$\widetilde{L} = \frac{-\cos\psi - \beta(D\sin\psi - \check{D}\frac{A_e}{A_v}) + r\cot\psi\left[-\alpha(D\sin\psi - \check{D}\frac{A_e}{A_v}) + B\sin\psi - \check{B}\frac{A_e}{A_v}\right]}{E\tan\psi - \beta D - r\cot\psi(1 - B + \alpha D)}, \tag{3.55}$$

where α and β are given by (3.51). The ratio A_e/A_v can be expressed as $A_r\exp(i\phi_r)$, where A_r and ϕ_r represent the amplitude ratio and the phase difference, respectively. Their expressions are given by [19]

$$A_r = \frac{\sqrt{\overline{\rho_1'^2}}/\overline{\rho}_1}{\sqrt{TKE_1}/U_1}, \quad \phi_r = \cos^{-1}\left[\frac{\overline{u_1'\rho_1'}}{\sqrt{\overline{u_1'^2}}\sqrt{\overline{\rho_1'^2}}}\right]. \tag{3.56}$$

The complex amplitudes that govern velocity and temperature fluctuations are given by $\widetilde{F}$, $\widetilde{G}$, $\widetilde{K}$ and $\widetilde{Q}$ as shown in (3.47), and these can be expressed in terms of $\widetilde{L}$ as

$$\widetilde{F} = \alpha D(\sin\psi - \widetilde{L}) - \alpha\check{D}\frac{A_e}{A_v}, \tag{3.57a}$$

$$\widetilde{G} = B\sin\psi + \widetilde{L}(1 - B) - \widetilde{F} - \check{B}\frac{A_e}{A_v}, \tag{3.57b}$$

$$\widetilde{K} = D(\sin\psi - \widetilde{L}) - \check{D}\frac{A_e}{A_v}, \tag{3.57c}$$

$$\widetilde{Q} = C(\sin\psi - \widetilde{L}) - \frac{\widetilde{K}}{\gamma} - \check{C}\frac{A_e}{A_v}. \tag{3.57d}$$

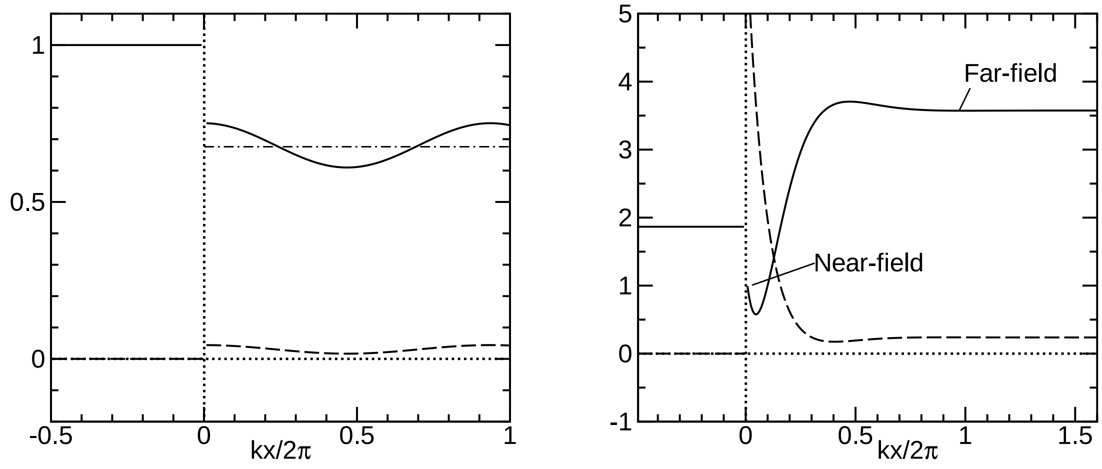

(a) (b)

FIGURE 3.5: Variation of $\overline{u'^2}$ (solid) and $\overline{e'^2}$ (dashed) with streamwise distance for $M_1 = 1.5$ and upstream incidence angle (a) $\psi = 45°$ (propagating regime) and (b) ψ=75° (decaying regime). In the propagating regime, $\overline{u'^2}$ oscillates about a mean value (dash-dot). The velocity fluctuation is normalized by the upstream mean velocity and the energy fluctuation is normalized by the downstream mean temperature and the specific gas constant R. All correlations are further normalized by the upstream TKE.

3.3.4 Results

Figure 3.5 shows the variation of streamwise Reynolds stress $\overline{u'^2}$ and internal energy variance $\overline{e'^2}$ for a purely vortical upstream disturbance interacting with a Mach 1.5 shock wave. The turbulent correlation $\overline{e'^2} = C_v^2\ \overline{T'T'^*}$. Uniform $\overline{u'^2}$ exists prior to the shock, located at x=0. In the absence of thermodynamic fluctuations, $\overline{e'^2}$ is identically zero in the upstream flow. The downstream Reynolds stress has contributions from the refracted vortical wave and the acoustic wave generated at the shock. The two components have different wavenumbers and their correlation exhibits a sinusoidal variation in the downstream flow. This can be prominently seen in figure 3.5(a), where the interaction at $\psi = 45°$ lies in the propagating regime. The downstream waves propagate at a constant amplitude, and the post-shock state remains unchanged far away from the shock (in the linear and inviscid framework). The internal energy variance also shows a sinusoidal trend, but with a relatively small amplitude, behind the shock.

The data plotted in figure 3.5(b) corresponds to $\psi = 75°$, which lies in the decaying regime. The Reynolds stress in this case shows a rapid non-monotonic variation from a low positive value (at x=0) to a high asymptotic level beyond $x \simeq \pi/k$. This rapid rise could be because of the following reason. The velocity fluctuations downstream of the shock have contributions from two modes, acoustic and vortical. Both these components of velocities are negatively correlated to each other, hence having a cancelling effect. However, away from the shock, the acoustic mode decays, and so does the velocity associated with it. What contributes to Reynolds stress in the far-field is the vortical component of velocity, thus attaining a significantly higher level as compared to the near-field; see Mahesh et al. [10] for further details. The amplitudes and correlations obtained immediately behind the shock (taken as a discontinuity) are identified as the near-field. By comparison, the far-field is defined as the asymptotic value obtained away from the shock at distances where the acoustic mode has become negligible in magnitude. We note that the $\overline{e'^2}$ correlation takes a high near-field value just across the shock and exponentially decays to a low far-field value, once again due to the decay of the acoustic part of the internal energy fluctuations.

The LIA results plotted in figure 3.5 are normalized as per Mahesh et al. [10]. The velocity fluctuations, both upstream and downstream, and the shock speed are non-dimensionalized by the upstream mean velocity U_1. The thermodynamic fluctuations downstream of the shock are non-dimensionalized by the respective mean values in the post-shock flow. The specific gas constant R is used to non-dimensionalize specific heats. Further, the magnitude of the downstream fluctuations and the shock speed are proportional to the amplitude of the upstream vortical wave. The correlations plotted in figure 3.5 are therefore normalized by the turbulence kinetic energy upstream of the shock wave. The same is true for other correlations presented in the following chapters. In the absence of a physical shock thickness in LIA, the pre-shock disturbance wave length $2\pi/k$ serves as the governing characteristic length. This is used to normalize the streamwise coordinate in figure 3.5 and all the other subsequent figures.

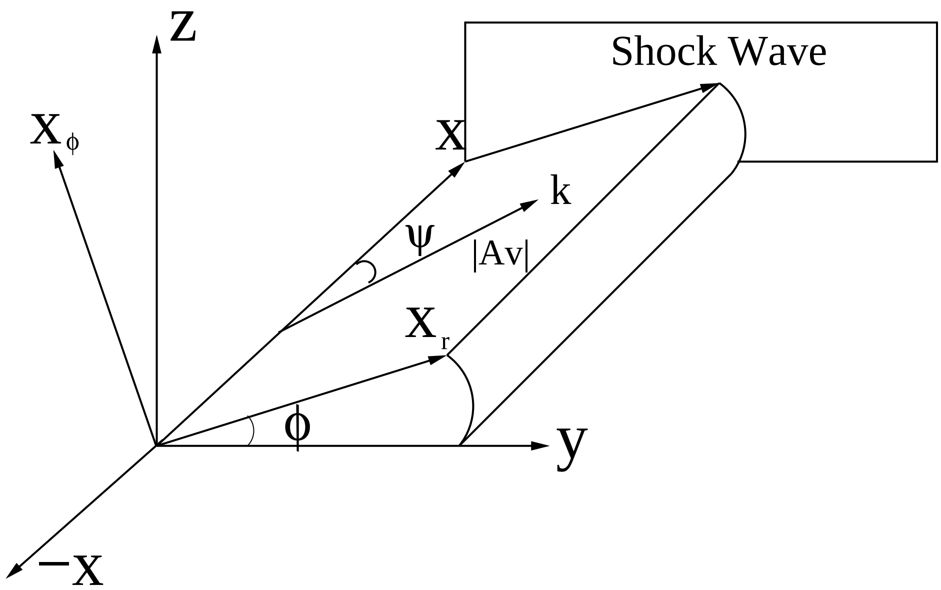

FIGURE 3.6: Plane wave in the $x - x_r$ plane normal to the shock.

3.3.5 Three-dimensional spectrum

Consider a three-dimensional space upstream of the shock wave as shown in figure 3.6. Here x-axis corresponds to the shock-normal direction, and y and z correspond to the shock-parallel direction. $x - x_r$ is a plane making an angle ϕ to the $x - y$ plane and axisymmetric about the x axis. Now consider a vortical wave having wavenumber k in the $x - x_r$ plane, making an angle ψ to the x axis. The amplitude of the vortical wave is represented by $|A_v|$.

The interaction of this single vorticity wave with the shock can be treated as a two-dimensional interaction in the $x - x_r$ plane. The Reynolds stress upstream of the shock along x and x_r direction is represented by E^1_{11} and E^1_{rr}, respectively. Here superscript 1 corresponds to the values upstream of the shock. For the given configuration,

$$E^1_{11} + E^1_{rr} = |A_v|^2. \tag{3.58}$$

Now consider this single vorticity wave as part of a spectrum of waves comprising a three-dimensional isotropic turbulence. The Reynolds stress contribution from an individual wave of wavenumber k for this upstream turbulence takes the expression

$$E^1_{ij} = \frac{E(k)}{4\pi k^2}\left(\delta_{ij} - \frac{k_i k_j}{k^2}\right), \tag{3.59}$$

where $E(k)$ is the upstream energy spectrum, and from the figure 3.6 the components of wavenumber k along x, y and z direction are

$$k_1 = k\cos\psi; \quad k_2 = k\sin\psi\cos\phi; \quad k_3 = k\sin\psi\sin\phi. \tag{3.60}$$

Substituting (3.60) in (3.59), an expression for the total Reynolds stress upstream of the shock can be written as

$$E_{11}^1 + E_{22}^1 + E_{33}^1 = 2\frac{E(k)}{4\pi k^2}, \tag{3.61}$$

where E_{22}^1 and E_{33}^1 are the Reynolds stresses along y and z directions, respectively. Also from from figure 3.6,

$$E_{11}^1 = |A_v|^2 \sin^2\psi,$$

and from (3.59),

$$E_{11}^1 = \frac{E(k)}{4\pi k^2}\sin^2\psi.$$

Comparing the above two equations,

$$\frac{E(k)}{4\pi k^2} = |A_v|^2.$$

For the upstream isotropic turbulence,

$$E_{11}^1 + E_{22}^1 + E_{33}^1 = E_{11}^1 + E_{rr}^1 + E_{\phi\phi}^1, \tag{3.62}$$

where $E_{\phi\phi}$ is the component normal to the $x - x_r$ plane along x_ϕ direction. From (3.62), (3.61) and (3.58),

$$E_{\phi\phi}^1 = |A_v|^2, \tag{3.63}$$

and this component of Reynolds stress remains unchanged across the shock for the given two-dimensional interaction.

The streamwise and transverse Reynolds stress downstream of the shock in the $x - x_r$ plane are represented by E_{11} and E_{rr}, respectively. They can be derived from (3.47) as

$$\frac{E_{11}}{U_1^2} = \left[\mid \widetilde{F} \mid^2 + \mid \widetilde{G} \mid^2 + \widetilde{F}\widetilde{G}^* e^{i(\tilde{k}-kmr)x} + \widetilde{F}^* G e^{-i(\tilde{k}-kmr)x} \right] |A_v|^2, \tag{3.64}$$

$$\frac{E_{rr}}{U_1^2} = [\mid \widetilde{H} \mid^2 + \mid \widetilde{I} \mid^2 + \widetilde{H}\widetilde{I}^* e^{i(\tilde{k}-kmr)x} + \widetilde{H}^* \widetilde{I} e^{-i(\tilde{k}-kmr)x}]|A_v|^2, \tag{3.65}$$

where the complex coefficients $\widetilde{F}$, $\widetilde{G}$, $\widetilde{H}$ and $\widetilde{I}$ are functions of the upstream Mach number M_1, the incidence angle of the disturbance ψ and the complex amplitudes A_v and A_e. The downstream transverse stresses can be written as

$$E_{22} + E_{33} = E_{rr} + E_{\phi\phi}, \tag{3.66}$$

where E_{rr} and $E_{\phi\phi}$ can be obtained from (3.65) and (3.63), respectively. The turbulent statistics behind the shock for the full upstream spectrum can be obtained by integrating over all the upstream wavenumbers for varying values of ψ and ϕ considering the integral volume

$$d^3\mathbf{k} = k^2 \sin\psi d\psi d\phi dk. \tag{3.67}$$

Integrating the energy spectra E_{11} over the integral volume, we obtain the three-dimensional streamwise Reynolds stress downstream of the shock i.e.,

$$\frac{\overline{u_2'^2}}{U_1^2} = \int_{k=0}^{\infty} \int_{\psi=\frac{-\pi}{2}}^{\frac{\pi}{2}} \int_{\phi=0}^{2\pi} E_{11}\, k^2\, \sin\psi\ d\phi\, d\psi\, dk. \tag{3.68}$$

The above integral is symmetric about ψ, and the solution is independent of ϕ. Thus the expression simplifies to

$$\frac{\overline{u_2'^2}}{U_1^2} = 4\pi \int_{k=0}^{\infty} \int_{\psi=0}^{\frac{\pi}{2}} E_{11}\, k^2\, \sin\psi\ d\psi\, dk. \tag{3.69}$$

In a similar manner, the transverse Reynolds stress can be obtained by integrating (3.66) i.e.,

$$\frac{\overline{v_2'^2}}{U_1^2} = \frac{\overline{w_2'^2}}{U_1^2} = \frac{4\pi}{2} \int_{k=0}^{\infty} \int_{\psi=0}^{\frac{\pi}{2}} \left[E_{rr} + \frac{E(k)}{4\pi k^2} \right] k^2\, \sin\psi\ d\psi\, dk. \tag{3.70}$$

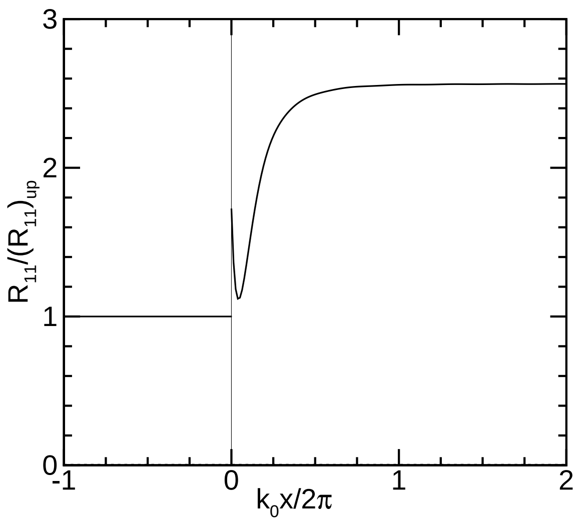

FIGURE 3.7: Streamwise variation of $\overline{u'^2}$ for a purely vortical upstream turbulence with $M_1 = 1.50$. The shock is located at $x = 0$.

An expression for the three-dimensional value of $\overline{u_2' e_2'}$ can be obtained as

$$(\overline{u_2' e_2'})_{3D} = 4\pi \int_0^{\pi/2} \int_0^{\infty} (\overline{u_2' e_2'})_{2D}\, k^2 \,\sin\psi \, dk \, d\psi \,, \tag{3.71}$$

where $(\overline{u_2' e_2'})_{2D}$ is given by (3.53). The three-dimensional energy spectrum tensor $E(k)$ is defined using the von Karman spectrum [71]

$$E(k) \sim \frac{\left(\frac{k}{k_0}\right)^2}{\left[\left(\frac{k}{k_0}\right)^2 + \frac{5}{6}\right]^{\frac{11}{6}}}, \tag{3.72}$$

where k_0 represents the wavenumber corresponding to the peak energy level. The effect of the upstream energy spectrum on the downstream turbulence statistics is shown in the next chapter.

A representative three-dimensional LIA result for the streamwise variation of $\overline{u'^2}$ is shown in figure 3.7 for the case of $M_1 = 1.50$. The shock is located at $k_0 x/2\pi = 0$, and before the shock a constant value of $\overline{u'^2}$ is observed. Across the shock, there is a non-monotonic variation of the correlation attributed to the decay in the acoustic energy. Note that, this variation is qualitatively similar to the corresponding two-dimensional result for a higher incidence angle shown in figure 3.5(b). Similar three-dimensional values for the correlations $\overline{e'^2}$ and $\overline{u'e'}$ can be obtained downstream of the shock for varying values of upstream Mach number.

3.4 DNS data analysis

3.4.1 DNS methodology

Larsson et al. [20] studied the interaction of homogeneous isotropic turbulence with a nominally normal shock using DNS. They solved the compressible Navier-Stokes equations for a perfect gas. All scales of turbulence were computed but the shock waves were captured numerically. The effectiveness of the shock capturing simulation is demonstrated in Larsson [72]. They employed different numerical schemes to solve for the different regions of the domain. The narrow regions around the shock waves used a fifth-order accurate weighted essentially non-oscillatory (WENO) scheme with Roe flux splitting, and a sixth-order accurate central difference scheme in the split form by Ducros et al. [73] was used in the rest of the domain. Time advancement was carried out using a fourth-order accurate explicit Runge-Kutta scheme. To obtain the inflow turbulent condition, isotropic turbulence was first generated in periodic boxes, which were blended together [56] and convected by mean velocity. The inflow turbulence satisfied the conditions proposed by Ristorcelli and Blaisdell [74]. Further description can be found in Larsson et al. [20] and Larsson and Lele [56]. The data used in the current work is also used to reproduce the earlier works of Larsson et al. [20], such as Reynolds stress evolution and its budget. This is carried out in order to verify the correctness in the use of the data.

3.4.2 Details of DNS data

Simulations were performed for 20 cases, each varying in either upstream Mach number, turbulent Mach number or Reynolds number as shown in table 3.1. While the upstream Mach number ranged from 1.06 to 6, turbulent Mach number for these cases were between 0.15 and 0.38. Further, two cases of upstream Reynolds number based on Taylor-scale (Re_λ) were considered for the study. These cases highlighted the effect of shock strength, upstream turbulent intensity and viscous mechanisms on the shock-turbulence interaction.

The DNS solution is obtained in terms of flow files, each file corresponding to a particular time step. The values of conserved variables ρ, ρu, ρv, ρw and $\rho E_\circ$ at all grid points in the domain

M_1	M_t	Re_λ	δ/η	$R_{kk}/(2U_1^2)$	$k_0 L_\epsilon$	A_r	X
1.28	0.15	38	0.69	7.3×10^{-3}	3.9	0.030	3.8×10^{-3}
1.28	0.22	39	0.97	7.3×10^{-3}	3.9	0.042	7.6×10^{-3}
1.28	0.26	38	1.15	7.3×10^{-3}	4.0	0.051	1.1×10^{-2}
1.28	0.31	38	1.34	7.3×10^{-3}	3.8	0.057	1.6×10^{-2}
1.50	0.15	38	0.38	5.3×10^{-3}	3.9	0.036	3.8×10^{-3}
1.50	0.22	39	0.53	5.3×10^{-3}	4.3	0.048	6.9×10^{-3}
1.50	0.31	39	0.75	5.3×10^{-3}	4.1	0.066	1.6×10^{-2}
1.50	0.37	39	0.91	5.3×10^{-3}	4.2	0.079	2.4×10^{-2}
1.87	0.22	39	0.31	6.9×10^{-3}	3.8	0.059	6.7×10^{-3}
1.87	0.31	39	0.43	6.9×10^{-3}	4.0	0.082	1.5×10^{-2}
2.50	0.22	40	0.18	4.0×10^{-3}	4.3	0.083	7.0×10^{-3}
3.50	0.16	40	0.07	2.1×10^{-3}	4.1	0.080	3.5×10^{-3}
3.50	0.23	41	0.10	2.1×10^{-3}	4.3	0.111	6.4×10^{-3}
4.70	0.23	42	0.07	1.2×10^{-3}	4.3	0.138	6.4×10^{-3}
6.00	0.23	42	0.05	0.7×10^{-3}	4.4	0.193	7.5×10^{-3}
1.50	0.14	73	0.26	4.7×10^{-3}	3.0	0.032	2.1×10^{-3}
3.50	0.15	74	0.05	0.9×10^{-3}	2.9	0.076	2.0×10^{-3}

TABLE 3.1: List of the DNS cases from Larsson et al. [20] used in the present study. The values correspond to the location immediately upstream of the mean shock wave. The ratio of shock thickness δ to Kolmogorov length scale η obtained by using (3.19) are given. The peak wavenumber k_0 is used to normalize the dissipation length scale L_ϵ. A_r (calculated using (3.56)) denotes the amplitude ratio of the upstream entropy wave and the upstream vorticity wave. X represents the ratio of the upstream turbulence kinetic energy associated with the acoustic fluctuations to the total turbulence kinetic energy present upstream of the shock.

are stored in the each of the file at different time intervals. Here, ρ represents the instantaneous density and u, v and w represent the instantaneous velocity in x, y and z direction. Total energy E_o is expressed in the form $\rho E_o = p/(\gamma - 1) + (1/2)\rho(u^2 + v^2 + w^2)$ with p being the instantaneous pressure. The number of flow files available for computing the turbulent statistics for each of the cases is shown in table 3.1.

3.4.3 Computing of statistics

For computing the turbulent statistics for a given case, the following procedure is adopted. First, mean variables such as $\overline{\rho}$, $\widetilde{u}$ and $\widetilde{T}$ are computed by averaging over the transverse direction (along y and z direction) and over different flow files. The fluctuating component of the flow variables at all the points in the transverse plane ($y - z$ plane) is calculated by subtracting the

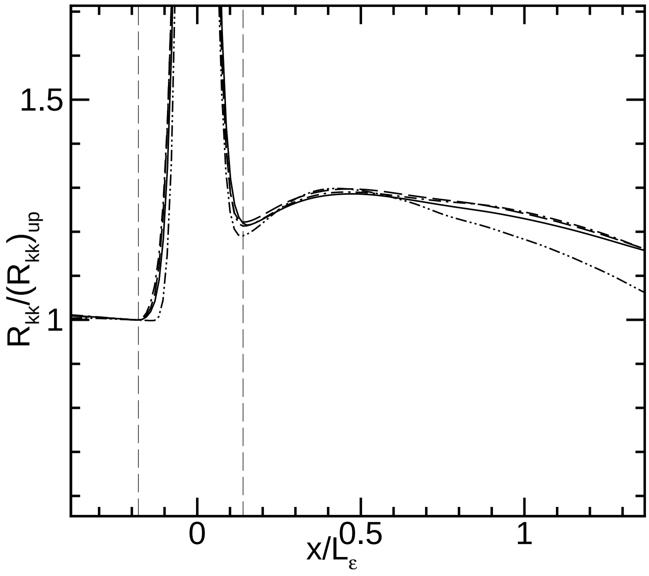

FIGURE 3.8: Streamwise variation of total Reynolds stress R_{kk} obtained by averaging over varying time period : $0.3\tau_L$ (dash dot dot), $0.6\tau_L$ (dash dot), $0.9\tau_L$ (dash) and $1.2\tau_L$ (solid), where τ_L is the time taken for convection of one isotropic box of length 2π through the shock for the case of $(M_1, M_t, Re_\lambda) = (1.5, 0.15, 38)$. The two vertical lines near $x/L_\epsilon = 0$ indicate the mean shock thickness for the 120 files case.

instantaneous value with its corresponding mean value, for example, $u' = u - \widetilde{u}$. A turbulent correlation can then be found by taking the product of the fluctuations (e.g. $u'u'$) and averaging the quantity over the transverse plane for different flow files. This provides a time- and space-averaged correlation (e.g. $\overline{u'u'}$) which varies along streamwise direction alone.

The mean variables as well as the turbulent correlations obtained using the flow files are tested for statistical convergence by using higher number of flow files for computing the average quantities. As an example, the streamwise variation of the total Reynolds stress R_{kk} is computed using varying number of flow files (30, 60, 90 and 120) as shown in figure 3.8 for the case of $(M_1, M_t, Re_\lambda = 1.5, 0.15, 40)$. Higher number of files corresponds to larger time period over which the averaging is performed. As mentioned, the turbulence isotropic boxes are blended and passed with the convective mean velocity through the shock. The averaging time associated with 120 flow files is approximately equal to the time required for one full box with streamwise length of 2π to be convected through the shock.

The value of R_{kk} is normalized by its value just upstream of the shock. The shock is centered at $x = 0$, and the streamwise distance is normalized by the dissipation length scale L_ϵ. The mean shock thickness indicated by the two vertical lines can be obtained by studying the dilatation of velocity. Regions with negative value of $\overline{\partial u_i/\partial x_i}$ represent the region of shock oscillation. As seen in the figure, the value of R_{kk} gets amplified across the shock and non-monotonically increases to a peak value before decaying. Using 30 files for statistical averaging is seen to yield slightly deviant trend especially in the downstream decay rate. A good match is observed when 60, 90 and 120 flow files are used to obtain the value of the Reynolds stress.

3.4.4 Computing of budget

Analyzing a budget of the transport equation for turbulent correlation helps in identifying the important physical mechanisms responsible for its evolution. A budget of turbulent energy flux is studied in detail in the next chapter. The methodology involved in computing the budget is described in the current section with the help of the transport equation for total Reynolds stress R_{kk}.

The various physical mechanisms that contribute to evolution of Reynolds stress can be studied by analysing its transport equation given by [20]

$$\partial_t(\overline{\rho}R_{ij}) + \partial_k(\overline{\rho}R_{ij}\widetilde{u}_k) = P_{ij} + T_{ij}^{(tt)} + \Pi_{ij}^{(pw)} + \Pi_{ij}^{(pd)} + \Pi_{ij}^{(pt)} + V_{ij}^{(vt)} + D_{ij}, \tag{3.73}$$

where

$$\begin{aligned}
P_{ij} &= -\overline{\rho}R_{jk}\partial_k\widetilde{u}_i - \overline{\rho}R_{ik}\partial_k\widetilde{u}_j, \\
T_{ij}^{(tt)} &= -\partial_k(\overline{\rho u_i'' u_j'' u_k''}), \\
\Pi_{ij}^{(pw)} &= -\overline{u_j''}\partial_i\overline{p} - \overline{u_i''}\partial_j\overline{p}, \\
\Pi_{ij}^{(pd)} &= \overline{p'\partial_i u_j''} + \overline{p'\partial_j u_i''}, \\
\Pi_{ij}^{(pt)} &= -\partial_i(\overline{p'u_j''}) - \partial_j(\overline{p'u_i''}), \\
V_{ij}^{(vt)} &= \partial_k(\overline{u_j''\sigma_{ik}} + \overline{u_i''\sigma_{jk}}), \\
D_{ij} = -\overline{\rho}\epsilon_{ij} &= -\overline{\sigma_{ik}\partial_k u_j''} - \overline{\sigma_{jk}\partial_k u_i''}.
\end{aligned}$$

The first and second term on the left hand side (LHS) of (3.73) represent the temporal and the convection term. The terms on the right hand side (RHS) are production, turbulent transport, pressure work mechanism, pressure-strain correlation, pressure-velocity transport, viscous transport and viscous dissipation, respectively. Here, σ_{ik} represents the viscous stress tensor given by $\sigma_{ik} = 2\mu\hat{s}_{ij} - 2\mu/3(\partial u_k/\partial x_k)\delta_{ij}$, where $\hat{s}_{ij}$ is the instantaneous strain-rate tensor expressed as $\hat{s}_{ij} = 1/2(\partial u_i/\partial x_j + \partial u_j/\partial x_i)$.

For the case of canonical STI, the mean flow is one-dimensional and uniform both upstream and downstream of the shock. Therefore $\partial\widetilde{f}/\partial x \approx \partial\widetilde{f}/\partial y \approx \partial\widetilde{f}/\partial z \approx 0$, where $\widetilde{f}$ is any mean variable. Also, the averaged turbulent statistics are steady and one-dimensional, which yields $\partial\overline{g}/\partial t \approx \partial\overline{g}/\partial y \approx \partial\overline{g}/\partial z = 0$ where $\overline{g}$ is any averaged turbulent quantity. The governing equation for Reynolds stress (3.73) thus reduces to [20]

$$\partial_1(\overline{\rho}\widetilde{u}_1 R_{kk}) = -2\overline{\sigma_{kj}\partial_j u_k''} + 2\overline{p'\partial_k u_k''} - 2\partial_1\overline{p'u_1''} - \partial_1\overline{\rho u_k'' u_k'' u_1''} + 2\partial_1\overline{u_k''\sigma_{k1}}, \tag{3.74}$$

where the terms on the RHS are viscous dissipation, pressure-strain correlation, pressure-velocity transport, turbulent transport and viscous transport, respectively.

The contribution from each of these mechanisms towards Reynolds stress can be found out by computing the budget for (3.74) using the DNS data. To compute the derivatives in the domain, a sixth order central differencing scheme is employed. The derivatives at the corner cells along the transverse direction in the domain are computed using periodic boundary conditions. A forward or backward differencing scheme is applied to get the derivatives at the corner cells in the streamwise direction.

Figure 3.9 shows the streamwise budget of the Reynolds stress equation (3.74) for the case of $(M, M_t, Re_\lambda) = (1.5, 0.15, 38)$, with the shock centered at $x/L_\epsilon = 0$. Just behind the shock, both, the pressure-strain and the pressure-velocity terms have positive contribution to the Reynolds stress, and their contribution decreases to negligible values within a distance of $x/L_\epsilon = 1$. The viscous dissipation term has a large negative contribution to the Reynolds stress through out the downstream region, and the decay rate of the Reynold stress for $x/L_\epsilon \geq 1$ is governed primarily by the viscous dissipation mechanism. The turbulent transport and viscous tranport terms have negligible contribution to the budget. This can be seen from the calculation

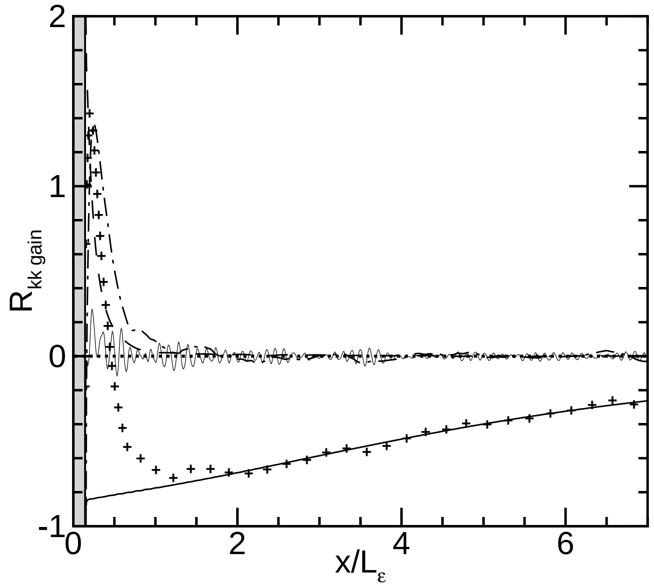

FIGURE 3.9: Reynolds stress budget (Equation 3.74) for $(M, M_t, Re_\lambda) = (1.5, 0.15, 38)$. Viscous dissipation (solid), pressure-strain (dashed), pressure-velocity (dash-dot), sum of first three RHS terms (symbol) and sum of first three RHS terms plus the mean convection (thin solid line around zero). All terms are normalized by the viscous dissipation term taken just behind the shock. The grey strip shows the region of unsteady shock movement.

of budget error (sum of the first three terms in the RHS of (3.74) plus the mean convection) in figure 3.9. Individually also, these terms are verified to be small (not shown in the figure).

The results obtained from DNS have influence of undesired acoustic frequencies that are generated as part of the solution. Effect of these frequencies on the turbulent statistics can be countered by spatial filtering, which involves averaging over a prescribed filter width. The filter width assumed along a streamwise direction is shown in figure 3.10, with x indicating the normalized distance from the shock.

The filter width increases parabolically from zero at $x = 0$ to a value of 1.4 at $x = 2$. The filter width is kept low near the shock as the statistics vary rapidly just behind the shock. For the rest of the domain beyond $x = 2$, the filter width is kept constant at 1.4. These filter values are chosen such that the physics represented by the turbulent statistics remain unchanged. The filtered value of a turbulent quantity at a particular point along streamwise direction is obtained by averaging the correlation over the corresponding filter width. The mean shock region (near $x = 0$) and the sponge region (towards the end of domain) are excluded while calculating the filtered quantities.

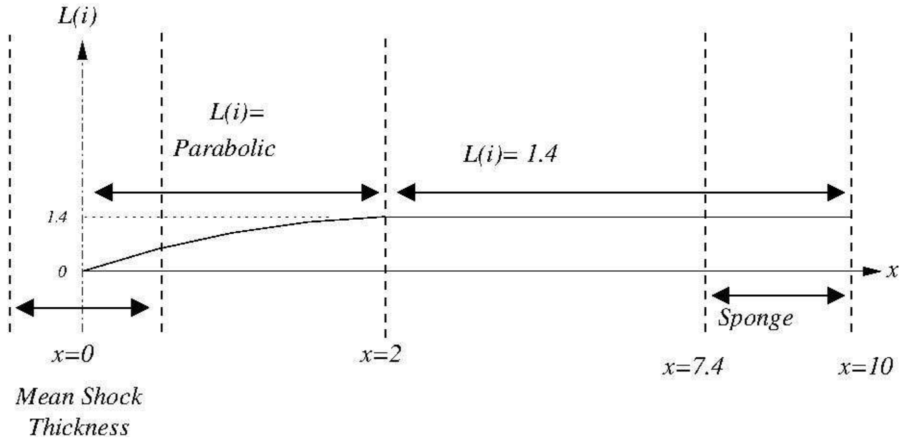

FIGURE 3.10: Change in the filter width $L(i)$ for varying normalized streamwise distance x.

3.5 Summary

In this chapter, formulation of linear interaction analysis is described in detail. A two-dimensional planar disturbance wave interacting with the shock is first studied, and the methodology for calculating the downstream turbulent statistics is highlighted. Next, a three-dimensional isotropic turbulence interacting with a shock is analyzed by superposing the two-dimensional interaction results for varying upstream wavenumbers and incidence angles. DNS data from Larsson et al. [20] is described in section 3.4. Post-processing this data to compute the turbulent statistics and the budget of a turbulent quantity is also described. These techniques are employed in studying the turbulent energy flux in the subsequent chapters.

Chapter 4

Analysis of Turbulent Energy Flux

4.1 Introduction

In this chapter we first study the elementary interaction of a single planar vortical wave with a normal shock. The effects of upstream mean flow Mach number and the wave incidence angle on the turbulent energy flux are investigated. Three-dimensional statistics, computed by integrating the single-wave contributions, are analysed for varying shock strengths. The energy flux correlation is also decomposed into its vortical, entropy and acoustic components to explain its behaviour downstream of the shock wave.

The results pertaining to two-dimensional single-wave interaction and those for three-dimensional spectrum upstream of the shock are described in sections 4.2 and 4.3, respectively. The linear theory results for three-dimensional turbulence are compared with DNS data for canonical STI in section 4.4. The DNS data is further analyzed to compute the budget of the turbulent energy flux transport equation in order to elucidate the dominant physical mechanisms behind a shock wave. Finally, the key observations from this work are stated in section 4.5.

4.2 Single-wave interaction results

A normalised expression for turbulent energy flux can be calculated using (3.53). Unless specified otherwise, all values of turbulent energy flux described in this work are normalised in this manner. Figure 4.1(a) shows the streamwise variation of the turbulent energy flux for purely vortical disturbances incident at 45 and 60 degrees, on a Mach 1.5 normal shock wave. The energy flux values upstream of the shock are identically zero, as expected for a purely vortical disturbance field interacting with a shock wave. In reality, a small value of turbulent energy flux can be expected even when the turbulence is largely vortical as will be shown in section 4.4. Both cases are in the propagating regime ($\psi < \psi_c$ for M_1 = 1.5), and the energy flux correlation shows no streamwise decay. The qualitative trend is similar to that presented in figure 3.5(a). For the lower incidence angle of $45°$, the downstream energy flux varies sinusoidally about a small positive mean, with the highest positive value obtained at the shock wave. The post-shock value attained at x=0 is the near-field energy flux correlation. For the $60°$ case, the correlation has peak negative value at the shock wave, and it oscillates about a negative mean far-field value. The sign of the correlation determines the direction of internal energy transfer due to turbulent mixing. Positive values of near-field $\overline{u_2'e_2'}$ indicate energy transfer away from the shock, as in the case of $\psi = 45°$. By comparison, a negative turbulent energy flux, for $\psi = 60°$, implies that the turbulent energy transfer is back towards the shock wave.

The turbulent energy flux generated by interactions in the decaying regime are shown in figure 4.1(b). The data corresponds to incidence angles of 70 and 80 degrees for an upstream Mach number of 3, where a stronger shock wave generates much higher energy flux values than those in figure 4.1(a). For $\psi = 70°$, the correlation starts with a negative near-field value just across the shock, shows a rapid increase to a positive peak followed by a non-monotonic decay to an asymptotic far-field value. We note that the net energy transport in the shock-normal direction is proportional to the streamwise derivative of the turbulent energy flux. Decaying interactions yield a high gradient in $\overline{u'e'}$ behind the shock, which can lead to a rapid redistribution of the post-shock energy in this region. This is in contrast to the energy flux generated by interactions in the propagating regime, where the sinusoidal variation of $\overline{u'e'}$ about a uniform mean value results in zero net transport of energy over a wavelength.

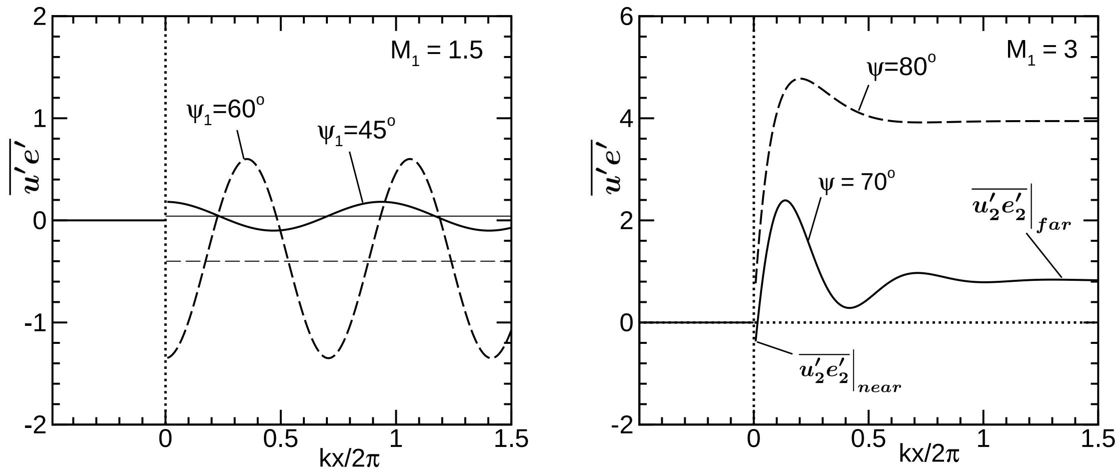

(a) (b)

FIGURE 4.1: Streamwise variation of $\overline{u'e'}$ generated by a planar vortical wave interacting with a normal shock: (a) propagating regime, and (b) decaying regime. The velocity fluctuation is normalized by the upstream mean velocity and the energy fluctuation is normalized by the downstream mean temperature and the specific gas constant R. All correlations are further normalized by the upstream TKE.

The variation of turbulent energy flux for $\psi = 80°$ is similar to that described above. The correlation has a higher peak value followed by a relatively higher far-field level compared to that at the lower incidence angle. Unlike the 70° case, $\overline{u'e'}$ is positive immediately behind the shock for the 80° interaction. Thus, the energy flux correlation takes distinct positive and negative values in the near-field and far-field for the different cases presented above. Its magnitude also changes significantly depending on the strength of the shock wave and the angle of incidence of the upstream disturbance wave. In the subsequent part, we study the variations in $\overline{u'e'}$ over the entire ψ range for varying M_1. The wave patterns generated at the shock and their contribution towards the energy flux correlation, both in the near-field and the far-field, are presented in detail.

4.2.1 Near-field analysis

Figure 4.2(a) shows the near-field values of the turbulent energy flux for a range of upstream Mach numbers and incidence angles. The critical angle ψ_c, given by (3.44), is plotted as a function of M_1, and peak negative values of the turbulent energy flux are observed in the vicinity of

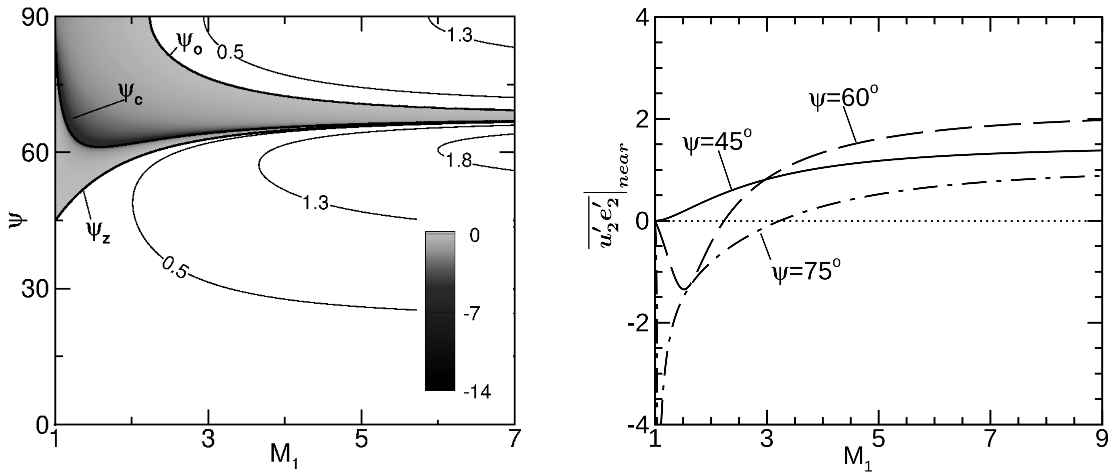

(a) (b)

FIGURE 4.2: Near-field turbulent energy flux generated by a single-wave interaction. (a) contours of $\overline{u_2'e_2'}$ across the $M_1 - \psi$ domain, with negative correlation shown in grey scale. The critical angle ψ_c separating the propagating from decaying regimes is plotted along with the angles ψ_z and ψ_o, for which the correlation is zero in the propagating and decaying regimes, respectively. (b) Variation of near-field $\overline{u_2'e_2'}$ for three representative incidence angles. Normalization as described in figure 4.1.

this curve (darker shade). This is because of the high values of the velocity and the temperature fluctuations generated by interactions at the critical angle, as discussed in the previous section.

The zone of the negative correlation is bounded by the ψ_z curve in the propagating regime and by the $\psi_\circ$ curve in the decaying regime. The flow physics at the incidence angles, ψ_z and $\psi_\circ$, are described subsequently. The unshaded part of $M_1 - \psi$ domain in figure 4.2(a) corresponds to positive $\overline{u_2'e_2'}$ immediately behind the shock. A few representative contour lines are plotted for reference, and it is noted that the positive values of the energy flux are much smaller in magnitude than the peak negative values obtained at the critical incidence angle.

The variation of the energy flux correlation with Mach number is plotted for three representative values of the incidence angle in figure 4.2(b). This corresponds to the data extracted along $\psi =$ constant lines in figure 4.2(a). The case with $\psi = 45°$ shows positive turbulent energy flux for the entire range of Mach numbers, with $\overline{u_2'e_2'}$ reaching an asymptotic value at high Mach numbers. The energy flux correlation takes vanishingly small values in the limit $M_1 \to 1$, as negligible temperature fluctuations are generated across a very weak shock wave. For $\psi = 60°$ case, the energy flux correlation is negative for relatively weak shocks ($M_1 < 2.25$), and increases to a positive limiting value as $M_1 \to \infty$. Both $\psi = 45°$ and $\psi = 60°$ are lower than the least value of $\psi_c \sim 61°$ (obtained at Mach 1.5) and therefore lie in the propagating regime for all Mach numbers.

The near-field turbulent energy flux for $\psi = 75°$ plotted in figure 4.2(b) shows large negative values in the vicinity of Mach 1. This is because of the fact that the critical angle ψ_c equals $75°$ for $M_1 = 1.04$, and a peak negative value of $\overline{u_2'e_2'} = -4.77$ is obtained at this Mach number. The correlation magnitude then drops rapidly to zero in the limit $M_1 \to 1$. Note that the $75°$ interactions for $M_1 > 1.04$ lie in the decaying regime, and both positive and negative turbulent energy flux values are generated depending on the mean flow Mach number. Negative $\overline{u_2'e_2'}$ correlation are confined to Mach numbers below 3 and positive values are obtained for stronger shock waves.

Nature of fluctuations in the propagating regime

Consider a plane vorticity wave incident at $45°$ on a Mach 1.5 shock wave. For this case, LIA predicts that all three downstream waves (vorticity, entropy and acoustic) are in phase with each other and with the upstream vorticity wave. The downstream disturbances such as u_2' and e_2', with contributions from the three modes, are also in phase with the upstream streamwise fluctuation u_1'. This can be seen in figure 4.3(a) where u_1' is plotted along with u_2' and e_2' as a function of time in the immediate vicinity ($x = 0$) of the instantaneous shock wave. For this interaction, the correlation $\overline{u_2'e_2'}$ is positive, as both the constitutive fluctuations are in phase.

Figure 4.3(b) plots the LIA solution for the fluctuations at x=0 for ψ = 60° and M_1=1.5. In this case, the velocity fluctuations, u_2' and u_1', are in phase with each other, but e_2' has an opposite phase to the velocity fluctuations. Thus, the correlation $\overline{u_2'e_2'}$ takes a negative value with the constituting fluctuations having a phase difference of π. Note that the post-shock u' and e' fluctuations are exactly in opposite phase for all propagating interactions with $\psi > \psi_z$, whereas the downstream fluctuations are in phase for lower angles of incidence ($\psi < \psi_z$). The ψ_z curve in the $M_1 - \psi$ plot in figure 4.2(a) thus demarcates the single-wave interactions that generate positive and negative energy flux correlations in the propagating regime.

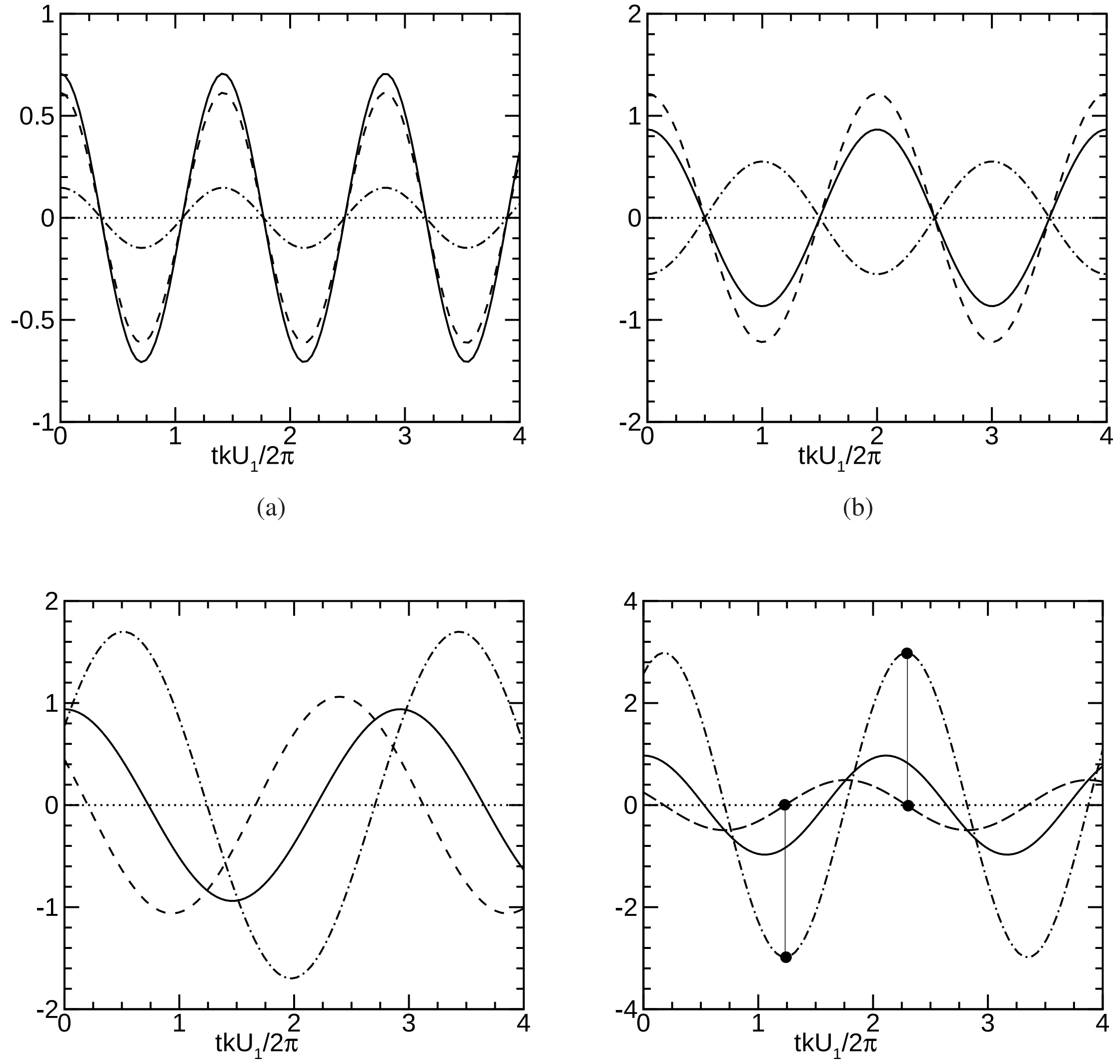

(a) (b) (c) (d)

FIGURE 4.3: Near-field variation of the fluctuating variables with time: u_1'(solid), u_2'(dashed) and e_2'(dash-dotted). (a) $\psi = 45°$, (b) $\psi = 60°$ and (c) $\psi = 70°$ for the case of $M_1 = 1.5$, and (d) $\psi = \psi_\circ = 76.3°$ at $M_1 = 3$. Velocity fluctuations are normalized by the upstream mean velocity and energy fluctuation is normalized by the downstream mean temperature and R. All fluctuations are normalized by $|A_v|$.

Interestingly, plane wave vortical disturbances incident on a shock at an angle of ψ_z generate vanishingly small energy flux downstream. For this unique angle ψ_z, it is found that the shock oscillations are in phase with the upstream velocity fluctuations, and the instantaneous shock speed matches the fluctuating streamwise velocity ($\xi_t = u_1'$). Thus, there are no apparent streamwise disturbances in the flow relative to the unsteady shock, and the shock-normal velocity fluctuations pass unchanged through the shock wave ($u_1' = u_2'$). The vorticity wave refracts through the shock and there is a change in the transverse velocity fluctuations. No acoustic or entropy waves are generated behind the shock for this case of $\psi = \psi_z$, resulting in a zero value of $\overline{u_2'e_2'}$.

An analytical expression for ψ_z can be obtained by equating the expressions for the shock speed and the streamwise velocity fluctuation just ahead of the shock. (3.34a) and (3.48) thus yield for $x = 0$

$$\sin\psi = \widetilde{L}. \tag{4.1}$$

The full expression for $\widetilde{L}$ is provided in (3.50). In the current limiting case of $\psi = \psi_z$ with $\alpha = 0$ and $\beta = \tan\psi/(\gamma M_2^2 r^2)$, the expression for $\widetilde{L}$ reduces to

$$\widetilde{L} = \frac{-\cos\psi - \beta D \sin\psi + rB\cos\psi}{E\tan\psi - \beta D - r(1-B)\cot\psi}. \tag{4.2}$$

Substituting the above expression in (4.1) results in

$$E\tan^2\psi_z = (r-1),$$

which simplifies to

$$\psi_z = \tan^{-1}\sqrt{r}. \tag{4.3}$$

Thus, ψ_z is a function of the mean density ratio across the shock wave, which in turn depends on the upstream mean flow Mach number and the ratio of specific heats. It starts from a value of $45°$ for $M_1 = 1$ and asymptotes to a value close to ψ_c in the limit of $M_1 \to \infty$ (see figure 4.2(a)). Thus, a vorticity wave incident at angles less than $45°$ generates positive $\overline{u_2'e_2'}$ behind the shock for all Mach numbers. Also, in the hypersonic limit, almost all the waves in the propagating regime, except for a small range near ψ_c, result in a positive energy flux correlation

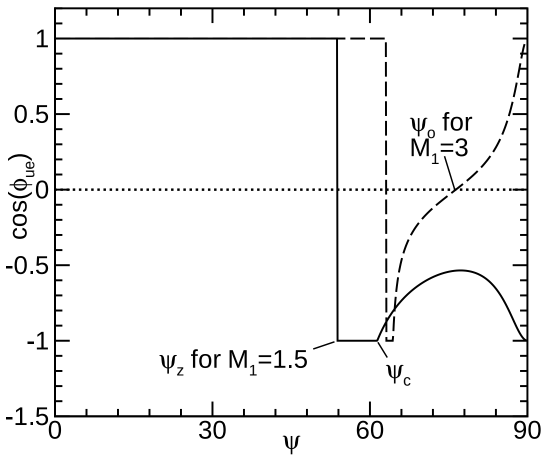

FIGURE 4.4: Cosine of phase difference between near-field u_2' and e_2' for an upstream Mach number of $M_1 = 1.5$ (solid) and $M_1 = 3$ (dashed) as a function of upstream wave angle.

in the near-field.

The temporal variation of u_2' and e_2' plotted in figure 4.3 provides further insight into the energy transfer taking place immediately behind the shock wave. The data for $\psi = 45°$ shows that positive streamwise velocity fluctuations are concurrent with locally higher internal energy, thus resulting in an energy transfer in the positive x direction, i.e. away from the shock wave. For the $60°$ incidence angle, on the other hand, higher streamwise velocity transports locally cooler fluid, with negative internal energy fluctuation, in the positive x direction. This is equivalent to an effective turbulent energy flux back towards the shock wave. For the special case of ψ_z without any entropy and acoustic waves generated at the shock, the downstream internal energy is uniform and the velocity fluctuations have no effect on the energy transport in the shock-normal direction.

Nature of fluctuations in the decaying regime

Figure 4.3(c) plots u_1', u_2' and e_2' at the shock as a function of time for $\psi = 70°$ at Mach 1.5, which lies in the decaying regime. In this case, the downstream streamwise velocity fluctuations appear to lag behind its upstream counterpart, while the post-shock internal energy fluctuations lead the upstream wave. The energy flux correlation is given by

$$\overline{u_2'e_2'} = |u_2'||e_2'|\cos\phi_{ue},$$

where ϕ_{ue} is the phase difference between the near-field streamwise velocity and internal energy fluctuations. The variation of $\cos\phi_{ue}$ with the upstream incidence angle is plotted in figure 4.4 for two Mach numbers. In the propagating regime, the velocity and the energy fluctuations are either in phase ($\psi < \psi_z$) or exactly in opposite phase ($\psi > \psi_z$). By comparison, the phase difference ϕ_{ue}, for interactions in the decaying regime, varies continuously over a range of values. For the case of $M_1 = 1.5$, when the incidence angle is increased beyond ψ_c, the phase difference decreases from π to reach a minimum value before increasing back to π for $\psi = 90°$. The correlation $\overline{u_2'e_2'}$ is negative for all decaying interactions at this Mach number (see figure 4.2(a)), and this is true for relatively weak shocks ($M_1 < 2.2$).

At higher Mach numbers, the correlation switches back from negative to positive values at a high upstream incidence angle. This can be seen for the case of $M_1 = 3$, where the phase difference ϕ_{ue} crosses $\pi/2$ at an incidence angle of $\psi_\circ$, and decreases further to zero at $\psi = 90°$. The disturbance waves plotted for $\psi = \psi_\circ = 76.3°$ at $M_1 = 3$ in figure 4.3(d) show this effect clearly. The nodes in the downstream velocity wave in this case coincide with the peaks in the internal energy wave, and vice-versa. The near-field energy flux correlation thus vanishes, in spite of the large internal energy fluctuations generated by the shock. This is unlike the ψ_z incidence angle in the propagating regime, where a zero energy flux is caused by the fact that no energy fluctuations are generated at the shock wave.

At the critical angle of incidence, the near-field turbulent energy flux is negative for all Mach numbers. For this case, the complex coefficients used in defining the downstream streamwise velocity and the temperature fluctuations, namely, $\widetilde{F}$, $\widetilde{G}$, $\widetilde{K}$ and $\widetilde{Q}$ (Eqn. (3.52)), have the following form

$$\begin{aligned} \widetilde{F} &= \frac{D\sin\psi_c}{\gamma r}, \qquad & \widetilde{G} &= \left(2 - B - \frac{D}{\gamma r}\right)\sin\psi_c, \\ \widetilde{K} &= -(D\sin\psi_c), \qquad & \widetilde{Q} &= \left(\frac{D}{\gamma} - C\right)\sin\psi_c, \end{aligned} \tag{4.4}$$

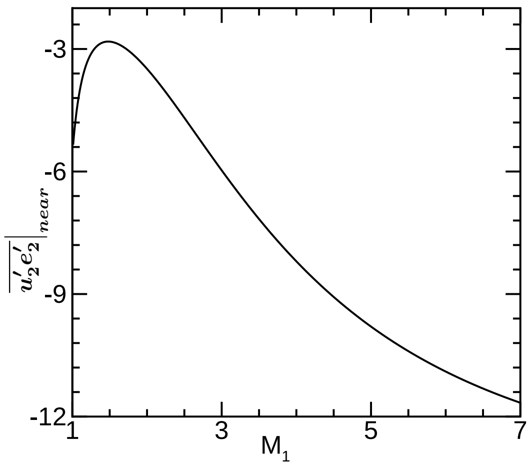

FIGURE 4.5: Near-field peak negative turbulent energy flux generated by single-wave interaction at the critical angle, plotted as a function of upstream Mach number. Normalization as described in figure 4.1.

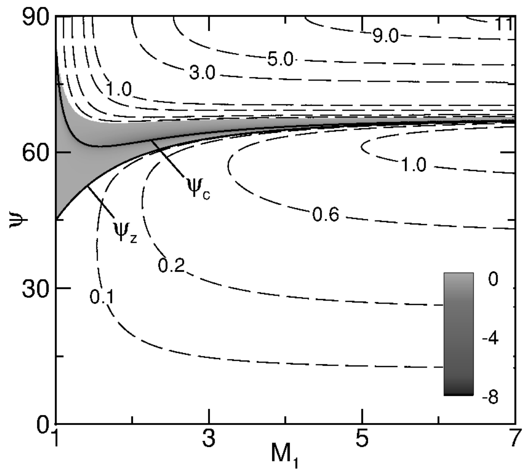

FIGURE 4.6: Far-field turbulent energy flux correlation obtained for varying upstream Mach number and wave incidence angle. Normalization as described in figure 4.1.

where the Rankine-Hugoniot coefficients are given in (3.38), and ψ_c can be calculated from (3.44) for a given upstream mean flow Mach number. The near-field value of the $\overline{u_2'e_2'}$ correlation, thus computed, is plotted for a range of upstream Mach numbers in figure 4.5 and it shows a non-monotonic behaviour leading to a limiting value for $M_1 \to \infty$.

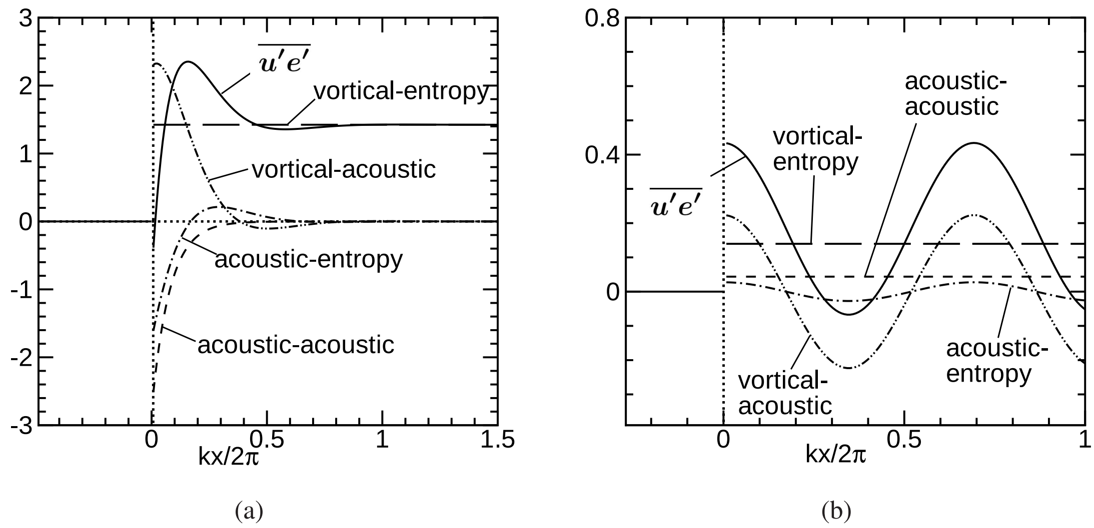

FIGURE 4.7: Modal decomposition of $\overline{u_2'e_2'}$ for the case of $M_1 = 2$ (a) $\psi = 75°$ (decaying regime) and (b) $\psi = 45°$ (propagating regime). Normalization as described in figure 4.1.

4.2.2 Far-field analysis

The far-field values of the turbulent energy flux obtained from LIA applied to single plane waves interacting with normal shock are plotted in figure 4.6. As earlier, the shaded part of the $M_1 - \psi$ domain indicates the region of negative $\overline{u_2'e_2'}$, and the positive values are shown using representative contour lines. The critical angle ψ_c is also shown, with $\psi < \psi_c$ representing the propagating regime. The far-field value of $\overline{u_2'e_2'}$ for a wave in the propagating regime is taken as the mean value about which the sinusoidal variation exists. This is based on the fact that the oscillating part of the correlation gets statistically cancelled in the far-field for a collection of waves representing a turbulence field.

The far-field results are qualitatively similar to the near-field energy flux plotted in figure 4.2(a). Peak negative values of the turbulent energy flux are obtained in the vicinity of the ψ_c curve, but the correlation is lower in magnitude than the corresponding near-field value. In the propagating regime, interactions with $\psi < \psi_z$ result in positive $\overline{u'e'}$ in the far-field, similar to the near-field trend; the correlation magnitudes are once again smaller than the near-field levels. By comparison, high positive values of the far-field $\overline{u'e'}$ are obtained in the decaying regime, with the largest energy flux generated for interactions at $90°$ incidence for any given Mach number.

Figure 4.7 shows a Kovasznay mode decomposition of the energy flux correlation for a single-wave interaction with a Mach 2 shock wave. As per (3.47), the streamwise velocity u_2' has contributions from the acoustic and the vortical waves, and e_2' has contributions from the acoustic and the entropy waves. Thus, the energy flux correlation can be decomposed into four parts

$$\overline{u_2'e_2'} = \left(\overline{u_2'e_2'}\right)_{aa} + \left(\overline{u_2'e_2'}\right)_{ae} + \left(\overline{u_2'e_2'}\right)_{va} + \left(\overline{u_2'e_2'}\right)_{ve}, \tag{4.5}$$

where subscripts aa, ae, va and ve correspond to acoustic-acoustic, acoustic-entropy, vortical-acoustic and vortical-entropy components, respectively, and they are given by

$$\left(\overline{u_2'e_2'}\right)_{aa} = \frac{1}{2\gamma}(\widetilde{F}\widetilde{K}^* + \widetilde{K}\widetilde{F}^*)\exp[i(\widetilde{k} - \widetilde{k}^*)x], \tag{4.6a}$$

$$\left(\overline{u_2'e_2'}\right)_{ae} = -\frac{1}{2(\gamma-1)}\left[\widetilde{F}\widetilde{Q}^*\exp[i(\widetilde{k} - kr\cos\psi)x] + \widetilde{Q}\widetilde{F}^*\exp[i(kr\cos\psi - \widetilde{k}^*)x]\right], \tag{4.6b}$$

$$\left(\overline{u_2'e_2'}\right)_{va} = \frac{1}{2\gamma}\left[\widetilde{K}\widetilde{G}^*\exp[i(\widetilde{k} - kr\cos\psi)x] + \widetilde{G}\widetilde{K}^*\exp[i(kr\cos\psi - \widetilde{k}^*)x]\right], \tag{4.6c}$$

$$\left(\overline{u_2'e_2'}\right)_{ve} = -\frac{1}{2(\gamma-1)}\left[\widetilde{G}\widetilde{Q}^* + \widetilde{Q}\widetilde{G}^*\right]. \tag{4.6d}$$

The streamwise variation of the four components of the energy flux correlation is shown in figure 4.7(a) for the $\psi = 75°$ decaying interaction. The vortical-acoustic component takes high values just behind the shock, while the acoustic-entropy and the acoustic-acoustic components of $\overline{u_2'e_2'}$ attain peak negative values in the near-field. All three components with contribution from the acoustic mode decay to negligible values in the far-field. By comparison, the vortical-entropy component takes a constant positive value in the downstream flow. The far-field energy flux correlation generated at the shock thus equals the non-zero vortical-entropy component. As earlier, the positive vortical-entropy contribution to $\overline{u_2'e_2'}$ implies energy transfer away from the shock, but a zero gradient in the streamwise direction suggests that there is no net build-up of internal energy due to this effect. On the other hand, the rapidly varying acoustic components of the turbulent energy flux can result in a local energy accumulation or depletion behind the shock wave.

The modal decomposition of the turbulent energy flux for a propagating interaction at $\psi = 45°$ is

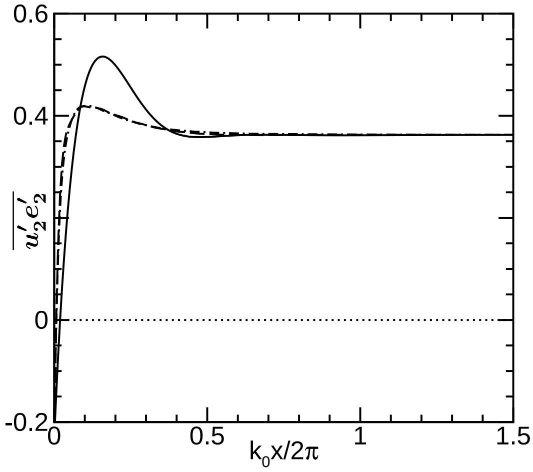

FIGURE 4.8: Turbulent energy flux along streamwise direction for $M_1 = 2$ (spectrum 1: solid, spectrum 2: dashed, spectrum 3: dash-dotted). Normalization as described in figure 4.1.

shown in figure 4.7(b). In this case, the vortical-entropy and the acoustic-acoustic components are both constant and positive in the downstream region. The sum of these two components yield the far-field value of $\overline{u_2'e_2'}$. The vortical-acoustic and the acoustic-entropy components exhibit a sinusoidal variation about a zero mean and therefore do not contribute to the far-field value. Note that the vortical-entropy component is the dominant contributor to the far-field energy flux; its value is substantially lower in this case than that in the interaction at $\psi = 75°$.

4.3 Three-dimensional isotropic spectrum

An expression for the downstream $\overline{u_2'e_2'}$ for a three-dimensional isotropic spectrum of planar waves is given by (3.71). This equation along with (3.47) yields

$$(\overline{u_2'e_2'})_{3D} = 4\pi \int_0^{\pi/2} \int_0^{\infty} \left[\left(\frac{\widetilde{Z}_1 + \widetilde{Z}_4}{2\gamma} \right) - \left(\frac{\widetilde{Z}_2 + \widetilde{Z}_3}{2(\gamma - 1)} \right) \right] |A_v|^2 k^2 \, \sin\psi \, d\psi \, dk, \tag{4.7}$$

where

$$\begin{aligned}
\widetilde{Z}_1 &= \left(\widetilde{F}\widetilde{K}^* + \widetilde{F}^*\widetilde{K}\right)\exp\left[i\left(\widetilde{k} - \widetilde{k}^*\right)x\right],\\
\widetilde{Z}_2 &= \widetilde{G}\widetilde{Q}^* + \widetilde{G}^*\widetilde{Q},\\
\widetilde{Z}_3 &= \widetilde{F}\widetilde{Q}^*\exp\left[i\left(\widetilde{k} - kr\cos\psi\right)x\right] + \widetilde{F}^*\widetilde{Q}\exp\left[-i\left(\widetilde{k}^* - kr\cos\psi\right)x\right],\\
\widetilde{Z}_4 &= \widetilde{G}\widetilde{K}^*\exp\left[-i\left(\widetilde{k}^* - kr\cos\psi\right)x\right] + \widetilde{G}^*\widetilde{K}\exp\left[i\left(\widetilde{k} - kr\cos\psi\right)x\right].
\end{aligned}$$

The coefficients $\widetilde{F}$, $\widetilde{K}$, $\widetilde{G}$ and $\widetilde{Q}$ are functions of ψ, γ and M_1, and are independent of the wavenumber k and $\widetilde{k}$. The spatial inhomogeneity in the turbulent energy flux is therefore due to the exponential terms in the above expression. These represent either the sinusoidal variation of the energy flux correlation about the far-field mean value or an exponential decay behind the shock wave. At $x = 0$, the inhomogeneous parts drop out, such that the terms $\widetilde{Z}_1$, $\widetilde{Z}_2$, $\widetilde{Z}_3$ and $\widetilde{Z}_4$ are independent of the wavenumber and the integral can be split into two parts,

$$(\overline{u_2'e_2'})_{3D} = \int_0^{\pi/2}\left[\frac{1}{2\gamma}\left(\widetilde{Z}_1 + \widetilde{Z}_4\right) - \frac{1}{2(\gamma-1)}\left(\widetilde{Z}_2 + \widetilde{Z}_3\right)\right]\sin\psi d\psi\int_0^\infty E\left(k\right)dk, \tag{4.8}$$

where the amplitude of the upstream velocity disturbance $|A_v|$ is written in terms of the three-dimensional energy spectrum $E(k)$

$$|A_v|^2 = \frac{E(k)}{4\pi k^2}. \tag{4.9}$$

The turbulent energy flux immediately behind the shock thus depends only on the integral of the energy spectrum, which is equivalent to twice the turbulent kinetic energy in the upstream flow. Also, the far-field value of the energy flux correlation consists of only the homogeneous part, and is independent of the upstream spectrum shape specified in the problem. This is true for any second order correlation, and is mentioned by Mahesh et al. [45] for the turbulence kinetic energy generated by the interaction of a field of acoustic waves with a normal shock.

On the other hand, the peak positive turbulent energy flux generated by the shock is sensitive to the spectrum shape. Figure 4.8 shows the data computed using three spectra, namely, a low

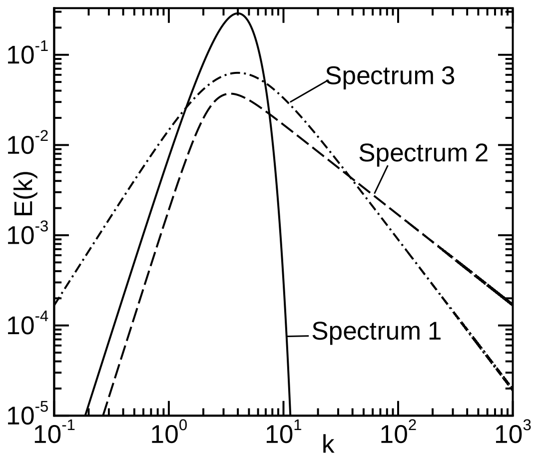

FIGURE 4.9: The energy distribution for varying wavenumbers shown for spectrum 1 : Mahesh et al. [19], spectrum 2 : Larsson et al. [20] and spectrum 3 : von Karman spectrum.

Reynolds number spectrum taken from Mahesh et al. [19]

$$\text{Spectrum 1: } E(k) \sim \left(\frac{k}{k_0}\right)^4 e^{-2\left(\frac{k}{k_0}\right)^2}, \tag{4.10}$$

the spectrum obtained from the DNS data of Larsson et al. [20] at $Re_\lambda = 75$

$$\text{Spectrum 2: } E(k) \sim \frac{\left(\frac{k}{k_0}\right)^4}{\left[\left(\frac{k}{k_0}\right)^4 + 0.32\right]^{1.29}}, \tag{4.11}$$

and the von Karman spectrum [71] given by

$$\text{Spectrum 3: } E(k) \sim \frac{\left(\frac{k}{k_0}\right)^2}{\left[\left(\frac{k}{k_0}\right)^2 + \frac{5}{6}\right]^{\frac{11}{6}}}, \tag{4.12}$$

where k_0 represents the wavenumber corresponding to the peak energy level. The spectrum shapes are shown in figure 4.9, where the area under each curve is normalized to unity. The DNS spectrum is comparable to the von Karman spectrum in terms of its peak energy at $k_0 \sim 4$ and the energy at high wavenumbers. By comparison, the low Re spectrum is devoid of high wavenumber content.

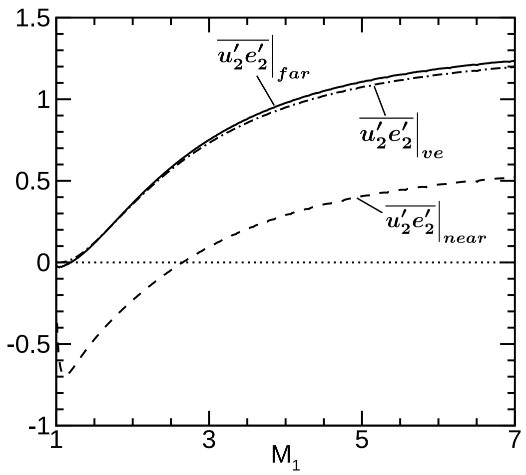

FIGURE 4.10: The near-field (dashed) and far-field (solid) $\overline{u_2'e_2'}$ for a three-dimensional isotropic spectrum for varying upstream Mach numbers. Also shown is the variation of vortical-entropy component of $\overline{u_2'e_2'}$. Normalization as described in figure 4.1.

The streamwise variations of the turbulent energy flux for Mach 2 are qualitatively similar for the three spectra. Spectrum 1 yields a higher peak energy flux, possibly because of higher energy over a limited range of wavenumbers, as compared to the other two spectra. The von Karman spectrum results are practically identical to those obtained using the DNS spectrum. It is therefore used for further analysis and comparison with the DNS data.

The three-dimensional near-field and far-field values of the turbulent energy flux are plotted as a function of the upstream Mach number in figure 4.10. The near-field values are positive at high Mach numbers, where the majority of the planar waves interacting with the shock generate positive energy flux correlation. Only a small fraction of the waves, incident close to ψ_c, result in negative correlation (see figure 4.2(a)). For low Mach numbers, a substantial range of incidence angles ($\psi > \psi_z$) result in negative energy flux behind the shock. Moreover, the higher incidence angles have a larger contribution to the spectrum integral due to the $\sin\psi$ factor in (3.71). The near-field turbulent energy flux computed for the three-dimensional spectrum, therefore, takes negative values for $M_1 < 2.7$. The correlation reaches its minimum value close to Mach 1, and vanishes in the limit $M_1 \to 1$, being physically consistent with interactions for very weak shock waves.

The far-field turbulent energy flux is positive except for a small range $1 < M_1 < 1.2$, and it is

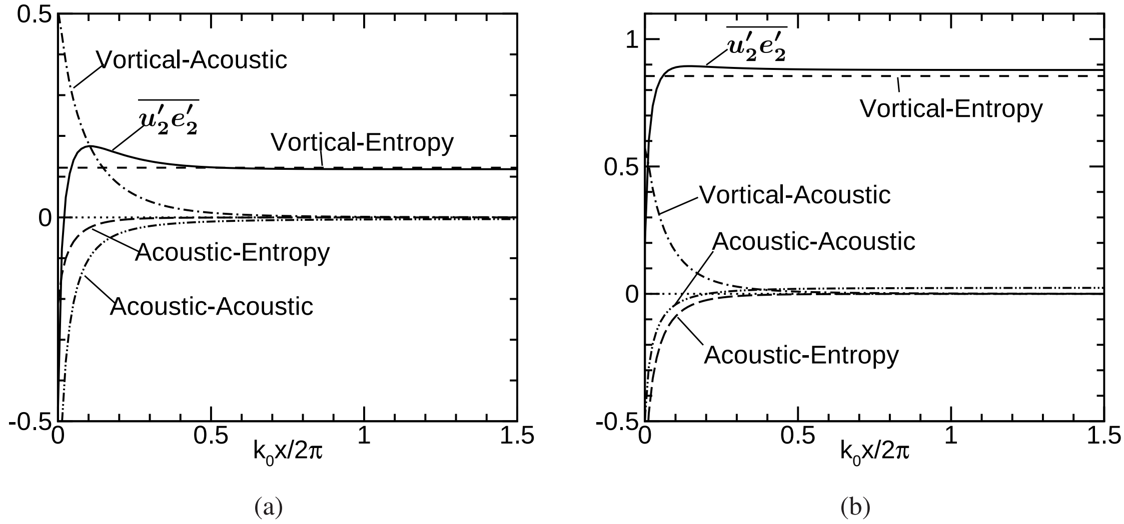

FIGURE 4.11: Variation of $\overline{u_2'e_2'}$ along streamwise direction for an upstream Mach number of (a) $M_1 = 1.50$ and (b) $M_1 = 3.50$. Also shown are the four components of $\overline{u_2'e_2'}$ as per (4.5). Normalization as described in figure 4.1.

significantly higher than the near-field value for all Mach numbers. The far-field correlation is close to the three-dimensional vortical-entropy component plotted in figure 4.10. The contribution from the acoustic mode is negative, and it accounts for the difference between the far-field and the near-field values of the correlation. Downstream of the shock, the acoustic components decay to negligible values within a distance of about one wavelength corresponding to the most energetic wavenumber (see figure 4.11(a)). The variation of the three-dimensional turbulent energy flux with the streamwise distance shown here is qualitatively similar to the decaying single-wave interaction shown in figure 4.7(a). The transient peak is, however, less pronounced in the three-dimensional result, possibly because of averaging over a large number of planar wave interactions with different wavelengths.

Comparison of the streamwise variation of the turbulent energy flux at two Mach numbers (figure 4.11 (a) and (b)) brings out some key differences. Immediately behind the shock, the acoustic components of the turbulent energy flux have larger magnitudes in the Mach 1.5 interactions, whereas the vortical-entropy component is dominant at Mach 3.5. The three acoustic terms give a net negative contribution to the energy flux, which is comparable at both the Mach cases. On the other hand, the significantly higher positive vortical-entropy component at $M_1 = 3.5$ results in a positive near-field value of $\overline{u_2'e_2'}$. Also, note that the transient peak is absent in the Mach 3.5

interaction, resulting in a monotonic rise from a low near-field value to the far-field asymptotic level. Further, there is a small non-zero acoustic-acoustic contribution to the turbulent energy flux at high Mach numbers, and it reflects in the difference between the far-field value and the vortical-entropy component plotted in figure 4.10.

The three-dimensional results show some of the same physical trends observed in the single wave interactions. This includes the high-gradient in $\overline{u'e'}$ in the acoustic-adjustment region behind the shock, which can influence the dip in the total energy. The mean energy conservation equation downstream of a steady one-dimensional shock wave can be written as

$$\overline{\rho}\,\overline{u}\frac{\partial \overline{E}}{\partial x} = \frac{\partial}{\partial x}\left(\overline{p}\,\overline{u}\right) - \gamma\frac{\partial}{\partial x}\left(\overline{\rho}\,\overline{u'e'}\right) + \text{ other terms,} \tag{4.13}$$

neglecting the difference between the Reynolds- and Favre averaging. Here, $\overline{E}$ is the total mean energy of the gas (sum of mean internal energy, mean kinetic energy and turbulence kinetic energy); $\overline{p}$, $\overline{u}$ and $\overline{\rho}$ are the mean pressure, velocity and density, respectively. Decrease in $\overline{u'e'}$ with distance from the shock can thus locally increase $\overline{E}$, and vice-versa. A local peak in $\overline{u'e'}$ could imply a possible dip in the total energy of a turbulent flow, all other factors held constant. It is shown that the high-gradient and non-monotonic behaviour of the turbulent energy flux is due to the decay of the acoustic contributions in the energy flux correlation. The turbulent kinetic energy behind the shock also shows a similar qualitative behaviour, once again due to the decay of acoustic disturbances generated at the shock [10].

4.4 Comparison with DNS data

In this section, the theoretical LIA results obtained for the three-dimensional interaction are compared with the DNS data of Larsson et al. [20]. The cases considered are listed in table 3.1, and range from low supersonic Mach numbers to hypersonic values. The turbulent Mach number $M_t = \sqrt{R_{kk}}/\widetilde{a}$ and the Reynolds number based on the Taylor micro-scale Re_λ are listed for each interaction, where R_{kk} is twice the turbulent kinetic energy and $\widetilde{a}$ is the Favre-averaged speed of sound. Table 3.1 also lists the estimated ratio of the laminar shock thickness to the Kolmogorov scale δ/η, which was shown by Ryu and Livescu [57] to describe the deviation

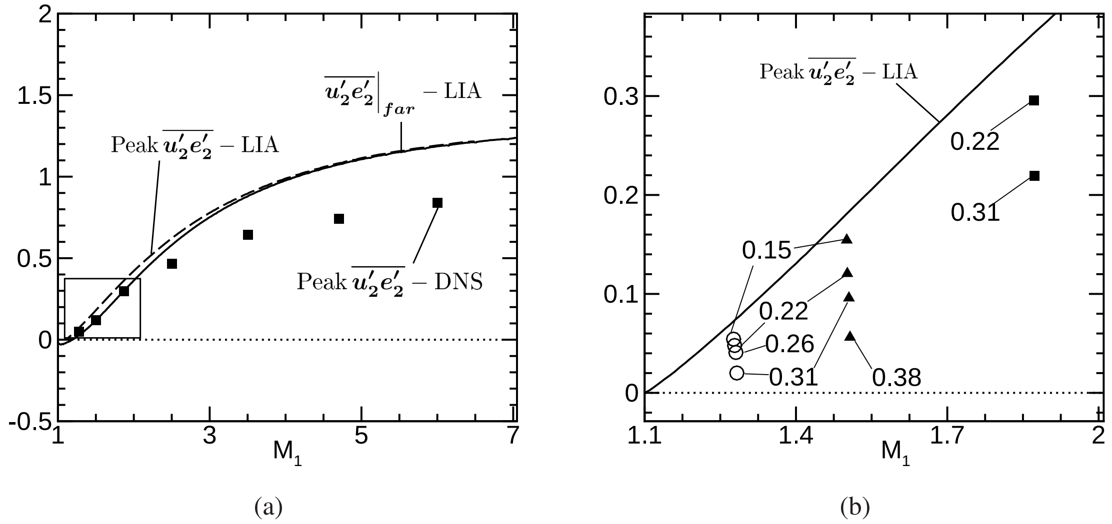

FIGURE 4.12: Variation of $\overline{u_2'e_2'}$ with upstream Mach number as per LIA (lines) and DNS (symbols). (a) DNS data corresponds to $M_t = 0.22$ and $Re_\lambda = 40$. (b) Magnified view highlighting the effect of M_t on the peak DNS $\overline{u_2'e_2'}$ for three Mach numbers (M_1=1.27 (circle), 1.50 (gradient) and 1.87 (square)) at $Re_\lambda = 40$. Normalization as described in figure 4.1.

away from the ideal LIA limit. This ratio is less than 1.4 for all cases considered here, and much less than that for most cases. For this range of δ/η values, Ryu and Livescu [57] found their DNS to operate in a regime converging towards the LIA result but with some effects of either nonlinearity or (more plausibly) viscous decay behind the shock. The same conclusion was reached in Larsson et al. [20], where the DNS cases used here were found to agree well with LIA but with clear viscous effects. This sets the context for our comparison between LIA and DNS in this section.

Figure 4.12(a) plots the peak turbulent energy flux behind the shock wave as a function of the upstream mean Mach number. Note that the peak LIA value is identical to the asymptotic far-field $\overline{u_2'e_2'}$ for high Mach numbers. In accordance with the normalization employed for LIA, the energy flux correlation obtained from DNS is normalized by the upstream mean velocity U_1, the downstream mean temperature $\overline{T}_2$, the specific gas constant R and the turbulence kinetic energy just upstream of the shock wave. We compare the DNS data for the Favre-correlation $\widetilde{u''e''}$ with the theoretical results for $\overline{u'e'}$ obtained from LIA. There is negligible difference between the two averaging procedures, when computed using the DNS data sets (details provided subsequently).

The variation of the peak turbulent energy flux with Mach number follows identical trends in

DNS and LIA. There is also a good quantitative match at low Mach numbers. All the DNS data plotted in the figure correspond to a value of $M_t = 0.22$, and the effect of varying upstream M_t on the post-shock statistics is discussed subsequently. Both DNS and LIA yield a finite limiting value of the normalized turbulent energy flux at high Mach numbers, i.e.

$$\lim_{M_1 \to \infty} \overline{u_2' e_2'} = \text{Const.},$$

which implies that the dimensional turbulent energy flux is proportional to the upstream mean velocity and the post-shock mean temperature. The high Mach number asymptotic value of the turbulent energy flux therefore scales as M_1^3 for a fixed upstream temperature $\overline{T}_1$ (as $U_1 = M_1\sqrt{\gamma R T_1}$ and $\overline{T}_2/\overline{T}_1 \propto M_1^2$ for $M_1 \to \infty$). This is consistent with the linear inviscid formulation of LIA, where the temperature fluctuations T_2' are proportional to the mean temperature $\overline{T}_2$ and all velocity fluctuations, including u_2', scale with U_1. Thus the peak turbulent energy flux obtained from DNS follows a high-Mach number scaling as per the linear inviscid framework. The data is, however, about 25% lower in magnitude than the LIA prediction.

Figure 4.12(b) shows the effect of turbulent Mach number M_t on the peak values of energy flux behind the shock wave. The DNS peak turbulent energy flux approaches the LIA prediction as the upstream turbulence intensity decreases for three upstream Mach numbers M_1 = 1.28, 1.5 and 1.87. Similar trend is also observed at $M_1 = 3.5$ (data not shown). This is in consonance with the results presented by Ryu and Livescu [57], where post-shock (streamwise and transverse) Reynolds stresses are found to match LIA results in the limit of $M_t \to 0$, even at low Reynolds numbers.

We next compare the streamwise variation of the turbulent energy flux obtained from DNS and LIA in figure 4.13. The Mach number of the interaction is 1.5 and DNS data corresponding to two Reynolds numbers is used for comparison. The shock is located at $x = 0$ with the two vertical lines representing the DNS unsteady shock movement region. The streamwise distance is normalized by the dissipation length scale L_ϵ, calculated just upstream of the shock as

$$L_\epsilon = (R_{kk}/2)^{3/2}/\epsilon, \tag{4.14}$$

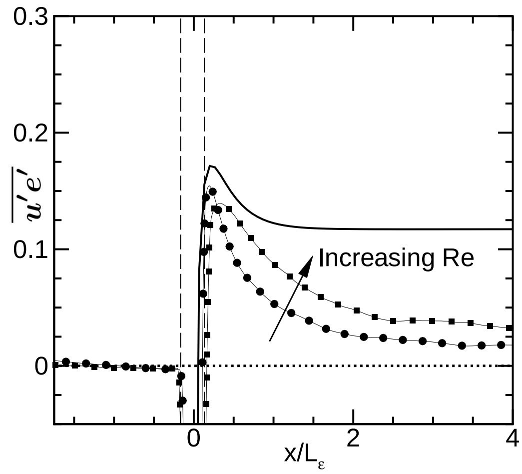

FIGURE 4.13: Streamwise variation of turbulent energy flux for $M_1 = 1.50$ from LIA (lines) and $(M_1, M_t) = (1.50, 0.15)$ from DNS (symbols). Effect of Reynolds number is also shown with $Re_\lambda = 40$ (circle) and $Re_\lambda = 75$ (square). $x = 0$ represents the center of the mean shock thickness, and the vertical lines near $x = 0$ represent the mean shock thickness region. Normalization as described in figure 4.1.

where ϵ is the turbulence dissipation rate, and the values of $k_0 L_\epsilon$ are listed in table 3.1. In the absence of viscous dissipation in the linear theory, the most energetic wavenumber (k_0) in the upstream turbulence is used to obtain the characteristic length. It is converted to an equivalent dissipation length scale for LIA using the value of $k_0\, L_\epsilon \approx 3 - 4$ obtained in the DNS study [20].

DNS data at both $Re_\lambda = 40$ and 75 have large negative values of the turbulent energy flux in the region of the unsteady shock wave. Starting from negative values at the shock, the energy flux correlation increases to peak positive values just behind the shock. The DNS trend is thus qualitatively similar to the variation of the energy flux obtained from the linear theory. This, along with the comparison of the peak values described earlier, indicates that LIA is possibly capturing some of the key physical processes involved in the generation of turbulent energy flux at a shock wave. Following the positive peak, the DNS energy flux reduces to low values away from the shock that is far below the far-field asymptotic $\overline{u'e'}$ predicted by the linear inviscid theory. This is because of the fact that LIA is based on inviscid approximations, while there are considerable viscous effects in the DNS computations performed at relatively low Reynolds numbers. Increasing the Reynolds number in the DNS, however, results in the data approaching the LIA results that are representative of the infinite Reynolds number limit.

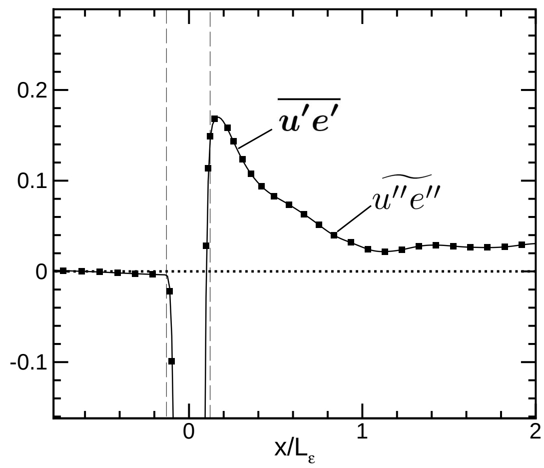

FIGURE 4.14: DNS streamwise variation of Favre-averaged (line) and Reynolds-averaged (symbol) turbulent energy flux for the case of $(M_1, M_t, Re_\lambda) = (1.5, 0.15, 38)$. $x = 0$ represents the center of the mean shock thickness, and the vertical lines near $x/L_\epsilon = 0$ represent the mean shock thickness region. Normalization as described in figure 4.1.

The higher Reynolds number case has a slight dip in the peak positive $\overline{u'e'}$ as compared to the corresponding lower Reynolds number value. This could be attributed to the fact that the $Re_\lambda = 75$ case has a broader spectrum as compared to the lower Reynolds number simulation. Reduction of the peak energy flux for a spectrum with energy distributed over a wider range of scales has been reported in figure 4.8. We also note that the streamwise location of the peak turbulent energy flux for the two Reynolds numbers are close to each other, when normalized by the dissipation length scale. This is not the case when the Kolmogorov length scale is used for normalization. The close match in the peak energy flux value as well as its location for the two Reynolds number cases highlight the fact that the near-field energy flux value is governed by large-scale inviscid processes. We further investigate the physical mechanisms responsible for the post-shock $\overline{u'e'}$ variation by studying the budget of its transport equation in section 4.4.2.

Figure 4.14 shows the DNS streamwise variation of turbulent energy flux computed using Reynolds fluctuations/averaging compared with Favre fluctuations/averaging for the case of $(M_1, M_t, Re_\lambda) = (1.50, 0.15, 38)$. Both forms yield identical results, and this similarity is observed for other turbulent statistics as well.Thus, a closer comparison between the DNS and LIA results is possible.

4.4.1 Effect of upstream thermodynamic fluctuations

The LIA model used here assumes a purely vortical incoming turbulence field, but the more realistic situation (both in canonical DNS and in more realistic flows) is to have a mixture of vortical, acoustic and entropy fluctuations. The purpose of this section is to roughly estimate the importance of these additional effects.

4.4.1.1 Upstream entropy mode

Larsson and Lele [56] report small but finite pressure, temperature and density fluctuations upstream of the shock, with magnitudes

$$\frac{\rho'_{rms}}{\overline{\rho}_1 M_t^2} = 0.44 \pm 0.01\,, \quad \frac{p'_{rms}}{\gamma P_1 M_t^2} = 0.39 \pm 0.02\,, \quad \frac{T'_{rms}}{(\gamma-1)\overline{T}_1 M_t^2} = 0.38 \pm 0.02, \tag{4.15}$$

for the majority of the cases listed in table 3.1. The entropy fluctuations in the DNS were extracted in the present study and found to be of magnitude

$$\frac{s'_{rms}}{c_p M_t^2} = 0.1 \pm 0.01, \tag{4.16}$$

where c_p is the specific heat at constant pressure. Entropy fluctuations are modeled in the linearized density field in LIA, and thus we use the amplitude $\rho'_{rms,\mathrm{LIA}} = s'_{rms}\overline{\rho}_1/c_p$ to model the entropy fluctuations in the LIA (with details given in section 3.3.3.2). While the phase difference between the vortical and entropy modes could be extracted from the DNS, in this particular flow configuration that phase difference has no physical meaning and is solely an artefact of the inflow condition. However, in many realistic flows, most notably in boundary layers, there is a specific favored correlation between these modes. In light of this, we consider a whole range of phase angles and focus on the bounding cases.

In figure 4.15, we compare the streamwise turbulent energy flux generated from a pure vorticity interaction with a case having finite upstream entropy fluctuations. The results are for the case of $M_1 = 3.50$, and two cases of upstream entropy fluctuations are considered - with $\phi_r = 0^o$ and $\phi_r = 180^o$, for the same amplitude. Other angles also have been studied to confirm that the

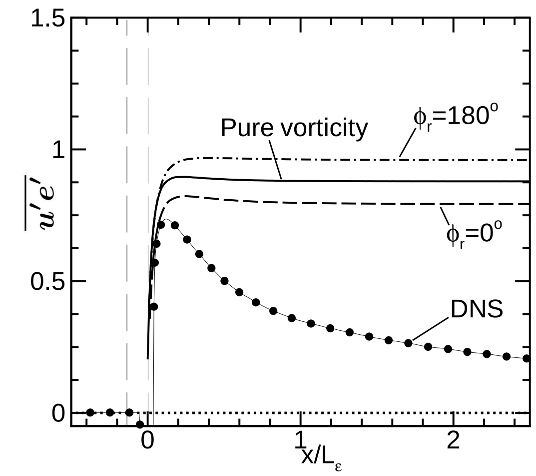

FIGURE 4.15: Streamwise variation of turbulent energy flux for $M_1 = 3.50$ from LIA (solid line), LIA with added upstream entropy fluctuations with $\phi_r = 0^o$ and $\phi_r = 180^o$ (dashed lines), and DNS (symbols) at $(M_1, M_t, Re_\lambda) = (3.50, 0.16, 40)$. The amplitude ratio A_r for the upstream entropy case is provided in table 3.1. $x = 0$ represents the center of the mean shock thickness, and the vertical lines near $x = 0$ represent the mean shock thickness region. Normalization as described in figure 4.1.

above two values of ϕ_r are the extreme bounds. Figure also shows the DNS data corresponding to $M_t = 0.16$ and $Re_\lambda = 40$. A value of $\phi_r = 0$ corresponds to a negative correlation between the velocity and energy fluctuation upstream of the shock. Such an upstream correlation yields a value of the downstream turbulent energy flux which is closer to the DNS value. For this ϕ_r value, an increase in the value of A_r (increase in the relative magnitude of the upstream entropy wave) further reduces the value of the turbulent energy flux. Upstream velocity and energy fluctuations that are opposite in phase ($\phi_r = 180^o$) have an amplifying effect on the turbulent energy flux correlation; a similar amplification is observed for the downstream energy variance as well (data not shown here) when $\phi_r = 180^o$. A single Mach number case has been shown here, and the trends are similar for other Mach numbers as well.

4.4.1.2 Upstream acoustic mode

The acoustic and the vorticity mode upstream of the shock travel at different speeds and are not correlated to each other. Therefore, the turbulent energy flux generated by a combined field of acoustic and vorticity modes can be studied by first analysing the independent interaction of

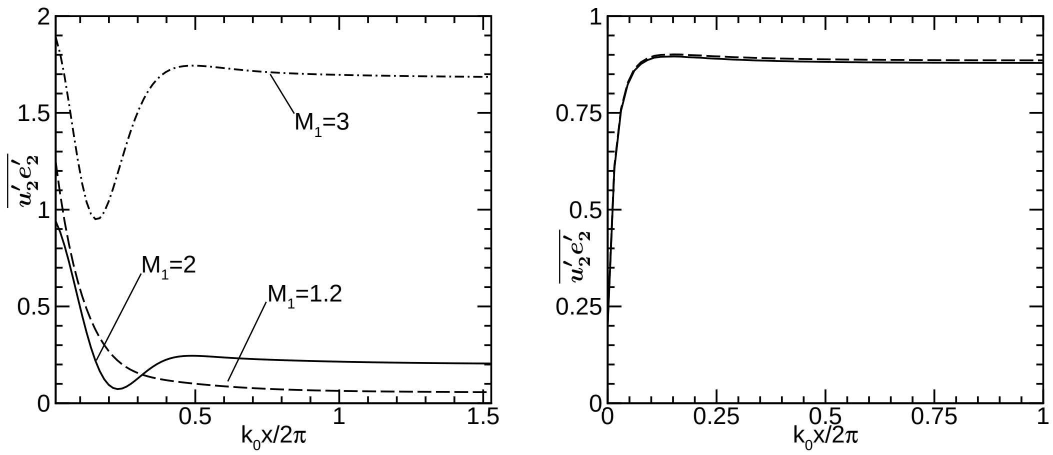

FIGURE 4.16: LIA results for streamwise variation of turbulent energy flux with added acoustic modes. (a) Purely acoustic fluctuations. (b) Comparison between purely vortical (solid) and combined acoustic/vortical (dashed) at $M_1 = 3.50$, where the relative amplitude of the acoustic field is the estimated upper bound for the DNS case at $(M_t, Re_\lambda) = (0.16, 40)$. Normalization as described in figure 4.1.

acoustic waves with the shock. The procedure is similar to that of vorticity waves interacting with the shock and is given elaborately in Moore [46] and Mahesh et al. [19]. The necessary details are provided in the appendix A.

Figure 4.16(a) plots the streamwise variation of the shock-normal turbulent energy flux when a purely acoustic field interacts with a shock wave (located at $x = 0$). The turbulent energy flux is normalized by the upstream turbulence kinetic energy of the acoustic disturbances, and the streamwise distance is normalized using the most energetic wavenumber k_0 in the upstream turbulence. We see a monotonic decay in the energy flux correlation at low Mach numbers ($M_1 = 1.2$), and a non-monotonic variation for higher mach numbers. Similar behaviour was reported by Mahesh et al. [45] in the streamwise variation of downstream TKE for the pure acoustic interaction. As earlier, the rapid variation in the turbulent energy flux near the shock can be attributed to the decaying acoustic waves generated at the shock wave. The far-field value of the correlation is largely due to the entropy and vorticity modes, and its magnitude increases upon increasing the upstream Mach number. The normalized turbulent energy flux is found to be of order 1 in the near-field, and is comparable in magnitude to that in the case of vorticity waves interaction with a shock (figure 4.11).

The turbulent energy flux generated by the combined post-shock interaction of the vortical and acoustic field is given by

$$\frac{\overline{u_2'e_2'}}{TKE_{total}} = \frac{\overline{u_2'e_2'}_{2vort} + \overline{u_2'e_2'}_{2ac}}{TKE_{vort} + TKE_{ac}}, \tag{4.17}$$

where subscript $vort$ is associated with the correlations obtained from the pure vortical interaction, and subscript ac corresponds to the pure acoustic interaction, both studied independently. The above equation can be written as

$$\frac{\overline{u_2'e_2'}}{TKE_{total}} = (1-X)\frac{\overline{u_2'e_2'}_{2vort}}{TKE_{vort}} + X\frac{\overline{u_2'e_2'}_{2ac}}{TKE_{ac}}, \tag{4.18}$$

where X represents the ratio of dilatational turbulence kinetic energy associated with the acoustic mode to the total turbulence kinetic energy in the combined vortical-acoustic turbulence. This is similar to the form used by Mahesh et al. [45] to study the effect of a combined field of vorticity and acoustic disturbances on the TKE evolution behind a shock wave.

The value of X is not trivial to extract from the DNS data, since a Helmholtz decomposition is complicated by the non-periodic shock-normal direction. An upper bound on X can be found by assuming that the upstream turbulence is purely acoustic, for which [45]

$$\frac{TKE_{ac}}{U_1^2} = \frac{1}{2}\left(\frac{1}{\gamma M_1}\right)^2 \frac{\overline{p_1'^2}}{P_1^2}, \tag{4.19}$$

where the pressure variance $\overline{p_1'^2}$ just before the shock is taken from the DNS data, as per (4.15). Since the pressure fluctuations in reality also have a hydrodynamic contribution (the "pseudo-sound", from the vortical fluctuations; see Ristorcelli and Blaisdell [74]), this formula clearly overestimates TKE_{ac}. For the DNS cases in this study, we find the bound $X \lesssim 10^{-3}$ to 10^{-2} as given in table 3.1.

Figure 4.16(b) shows the streamwise variation of the turbulent energy flux values when the upstream turbulence has a combination of vortical and acoustic disturbances. The results correspond to Mach number of 3.5, and the combined interaction results are obtained by using (4.18). The turbulent Mach number is 0.16 and it gives a value of $X = 3.5 \times 10^{-3}$. The turbulent energy flux obtained for the combined interaction is almost identical to that for the purely vortical disturbances upstream of the shock wave.The upstream acoustic mode has negligible effect, and is primarily because of the low value of the dilatational to total turbulent kinetic energy ratio. This may not be the case for flows with significant acoustic mode contribution, i.e. dilatational velocity field, upstream of the shock. Examples include turbulent free shear layers and their interaction with shock waves, in practical applications like underexpanded jets.

Further, high-speed boundary layers are known to have significant entropy fluctuations in addition to a vortical velocity disturbance field. As per Morkovin's hypothesis, the ratio of temperature to velocity fluctuations scale as the square of the mean flow Mach number. The sign of the velocity-temperature correlation is also known to strongly influence shock-turbulence interaction [6]. Negative correlation yields higher TKE amplification at the shock compared to that in the case of positively correlated vorticity-entropy disturbances in the upstream flow [10]. Velocity and temperature fluctuations in high-speed boundary layers are usually negatively correlated, but the correlation may be positive for highly-cooled walls. These can have significant effect on the turbulent energy flux generated by a shock wave. The presence of mean shear and shock curvature in realistic flows can bring in additional effects not considered in this work.

4.4.2 Transport equation for turbulent energy flux

To derive the transport equation for the energy flux correlation, we start with the instantaneous momentum and energy conservation equations given by

$$\frac{\partial}{\partial t}(\rho u_i) + \frac{\partial}{\partial x_j}(\rho u_i u_j) = -\frac{\partial p}{\partial x_i} + \frac{\partial \tau_{ij}}{\partial x_j}, \tag{4.20}$$

$$\frac{\partial}{\partial t}(\rho e) + \frac{\partial}{\partial x_j}(\rho e u_j) = -p\frac{\partial u_i}{\partial x_i} - \frac{\partial q_j}{\partial x_j} + \tau_{ij}\frac{\partial u_i}{\partial x_j}, \tag{4.21}$$

where τ_{ij} is the viscous stress tensor and q_j is the heat conduction flux given by $q_j = -\kappa\partial T/\partial x_j$, κ being the conductivity of the fluid. In this section 4.4.2, for the sake of brevity, we use tensor notations to denote the terms. Subscripts 1, 2 and 3, wherever applicable, correspond to x, y and z directions, respectively. The first and the second terms on the right-hand side (RHS) of (4.21) represent the pressure-dilatation and the conduction mechanisms, while the third term represents viscous dissipation. A moment of (4.20) with e'' can be added to a moment of (4.21) with

u'' and then Reynolds averaged to yield a transport equation for $\overline{\rho u''e''}$. Details are provided in Hanifi et al. [75].

For the canonical case under consideration, $\partial\overline{f}/\partial y = \partial\overline{f}/\partial z = 0$, where $\overline{f}$ is any mean quantity. The gradient of the mean quantity along the streamwise direction is negligible away from the shock, i.e. $\partial\overline{f}/\partial x \approx 0$. Also, the averaged turbulent statistics are steady and one dimensional, which yields $\partial\overline{g}/\partial t = \partial\overline{g}/\partial y = \partial\overline{g}/\partial z = 0$ for any turbulent correlation $\overline{g}$. The governing equation for the streamwise energy flux thus reduces to

$$\begin{aligned}\overline{\rho}\widetilde{u}\frac{\partial}{\partial x}\widetilde{u''e''} = &\underbrace{\overline{e''\frac{\partial\tau_{1j}}{\partial x_j}}}_{\substack{\text{Vis. diffusion}\\ \text{and dissipation}}} - \underbrace{\overline{e''\frac{\partial p}{\partial x}}}_{\text{Press. energy}} - \underbrace{\overline{pu''\frac{\partial u_j''}{\partial x_j}}}_{\text{Pressure-dilatation.}} - \underbrace{\overline{u''\frac{\partial q_j}{\partial x_j}}}_{\text{Conduction}} \\ &+ \underbrace{\overline{u''\tau_{jk}\frac{\partial u_j''}{\partial x_k}}}_{\text{Vis. dissipation}} - \underbrace{\frac{\partial}{\partial x}\overline{\rho e''u''u''}}_{\text{Turbulent transp.}},\end{aligned} \tag{4.22}$$

The first two terms on the RHS are the correlation of the viscous stress and the pressure gradient with internal energy fluctuation. The former represents viscous diffusion and dissipation mechanism, while the latter corresponds to pressure-energy effect. The third, fourth and fifth terms are correlation of pressure-dilatation, heat conduction and viscous dissipation with the streamwise velocity fluctuation. The last term represents the turbulent transport of the energy flux correlation.

4.4.2.1 Budget using DNS data

The budget of the above transport equation is computed for the case of $(M_1,\, M_t,\, Re_\lambda) = (1.5,\, 0.15,\, 40)$, and the data is presented in figure 4.17(a). A total of 120 flow field realizations at different time instances are used to compute the time-averaged turbulence statistics, and statistical convergence is checked for. It is found that the pressure-energy and the pressure-dilatation terms identified in (4.22) are the major contributors to the evolution of $\widetilde{u''e''}$. The viscous diffusion and dissipation terms, as well as the conduction and turbulent transport terms, are comparatively negligible, and are not shown in the figure. The difference between the LHS and the RHS of the transport equation is shown as error in figure 4.17 (thin solid line around

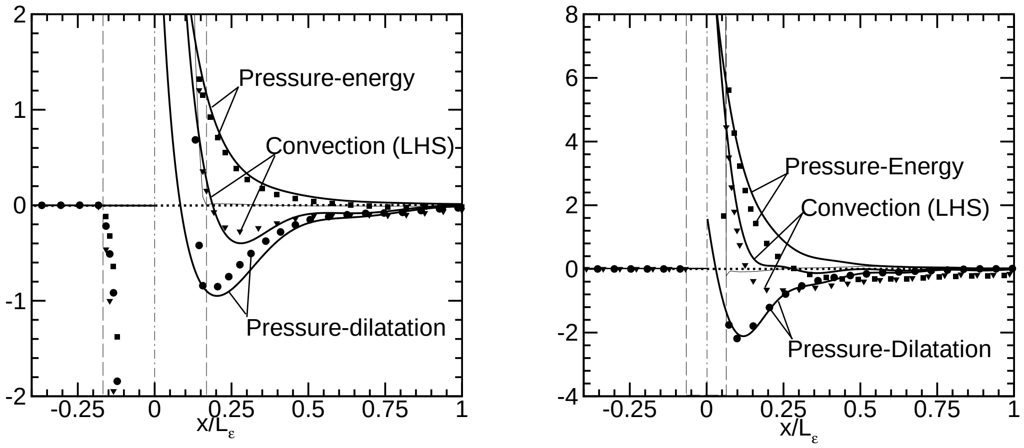

(a) (b)

FIGURE 4.17: Budget of transport equation for the turbulent energy flux from DNS data (symbols) and LIA (lines) corresponding to (a) $(M_1,\ M_t,\ Re_\lambda)\ =\ (1.5,\ 0.15,\ 40)$ (b) $(M_1,\ M_t,\ Re_\lambda) = (3.5,\ 0.15,\ 40)$. The vertical dashed lines at near $x/L_\epsilon = 0$ (dashed) represent end of the mean shock thickness region. The error in the DNS budget is also shown (thin solid line around zero). Normalization as described in figure 4.1.

zero). It has a negligible value outside the mean shock thickness region where the DNS results are compared with linear theory.

The pressure-energy term has a peak positive contribution close to the shock and drops to low values in the far-field. The pressure-dilatation term also has a peak positive contribution at the shock; it attains a minimum (negative) value behind the shock before decaying to zero. The convection term (left-hand side) in (4.22) is a resultant of the pressure-energy and the pressure-dilatation contributions. It takes a positive value in the near-field, which corresponds to a rapid increase in the energy flux behind the shock. The zero-crossing of the LHS term corresponds to the peak positive $\overline{u_2'e_2'}$. Subsequent negative values of the convection term indicate a decay of the correlation to low levels in the far-field.

Pressure-dilatation term in the energy conservation equation (4.21) represents the work done by pressure forces in compressing/expanding the gas. A locally high pressure associated with negative dilatation, such that $p(\partial u_i'/\partial x_i) < 0$, increases internal energy. How this increase in the energy is transferred by turbulent velocity fluctuations is governed by the term $\overline{pu''(\partial u_j''/\partial x_j)}$ in the turbulent energy flux equation (4.22). The fact that the correlation is negative implies that the internal energy fluctuations generated by the pressure-dilatation work are convected, on an average, in the negative x-direction. It therefore contributes as a negative source term in the transport equation for turbulent energy flux. The pressure-dilatation term can be split into two parts based on the mean and the fluctuating pressure as

$$\overline{pu''\frac{\partial u_j''}{\partial x_j}} = \overline{p}\,\overline{u''\frac{\partial u_j''}{\partial x_j}} + \overline{p'u''\frac{\partial u_j''}{\partial x_j}}\,.$$

The major contribution to the budget is from the first part, which is proportional to the mean pressure downstream of the shock. The second part, involving a higher-order correlation, is comparatively small in magnitude. The pressure-dilatation effect on the turbulent energy flux is therefore determined primarily by the $\overline{u''(\partial u_j''/\partial x_j)}$ correlation. The data shows that positive velocity fluctuations are associated with local expansion of the the fluid element. Similarly, lower streamwise velocity is statistically correlated with locally compressed fluid. The $\overline{u''(\partial u_j''/\partial x_j)}$ correlation can be expanded as

$$\overline{u''\frac{\partial u_j''}{\partial x_j}} = \frac{\partial}{\partial x}\frac{\overline{u''^2}}{2} + \overline{\frac{\partial v''}{\partial y}u''} + \overline{\frac{\partial w''}{\partial x}u''},$$

where the first term on the RHS can be argued to be positive in the acoustic-adjustment region behind the shock. It represents the buildup of streamwise Reynolds stress as a result of the acoustic decay, and can be seen clearly in figure 3.5(b).

The physics behind the pressure-energy term in (4.22) can be elucidated as follows. Pressure gradient in a flow can accelerate or decelerate a fluid element. Locally negative pressure gradient would generate positive streamwise velocity fluctuations, all other factors held constant. This when correlated with locally high internal energy ($e'' > 0$) would contribute to positive turbulent energy flux. The region ($0 < x/L_\epsilon < 1$) considered for budget calculation is dominated by the acoustic mode. The thermodynamic fluctuations can therefore be assumed to be approximately isentropic, i.e., $p'/(\gamma\overline{p}) \simeq T'/((\gamma-1)\overline{T})$, such that the pressure-energy term can be written as

$$-\overline{e''\frac{\partial p'}{\partial x}} = -C_v\overline{T'\frac{\partial p'}{\partial x}} = -\frac{1}{\gamma\overline{p}}\frac{\partial}{\partial x}\left(\frac{\overline{p'^2}}{2}\right),$$

once again neglecting the differences between Favre and Reynolds averaging. Large pressure fluctuations are generated by interactions at high incidence angles. In the decaying regime, the pressure-variance decreases exponentially to small values within one integral length scale. The pressure-energy source term shows identical trends, suggesting that it is dominated by the acoustic mode.

4.4.2.2 Linear inviscid approximations

A transport equation for the turbulent energy flux in the linear inviscid framework can be derived from the linearised Euler equations given by

$$\frac{\partial u'}{\partial t} + \overline{u}\frac{\partial u'}{\partial x} = -\frac{1}{\overline{\rho}}\frac{\partial p'}{\partial x},$$

$$\frac{\partial e'}{\partial t} + \overline{u}\frac{\partial e'}{\partial x} = -\frac{\overline{p}}{\overline{\rho}}\left(\frac{\partial u_j'}{\partial x_j}\right),$$

where the viscous and the conduction effects have been neglected in line with the LIA assumptions, and the higher-order terms are also assumed to be small. A transport equation for the turbulent energy flux can be derived from the above equations using the steps outlined earlier for the derivation of (4.22)

$$\overline{\rho}\,\overline{u}\frac{\partial}{\partial x}\overline{u'e'} = -\underbrace{\overline{e'\frac{\partial p'}{\partial x}}}_{\text{Press. energy}} - \underbrace{\overline{\overline{p}u'\frac{\partial u_j'}{\partial x_j}}}_{\text{pressure-dilatation}}. \tag{4.23}$$

The two terms on the RHS are the pressure-energy and pressure-dilatation terms, which are almost identical to their counterparts in (4.22). Again, the differences due to Favre and Reynolds fluctuations are found to be minimal from the DNS data. The viscous, conduction and turbulent transport terms seen in (4.22) are absent here due to the linear inviscid assumptions.

Using LIA with purely vortical upstream turbulence, we plot the budget of (4.23) in figure 4.17(a) for the region downstream of the shock corresponding to the case of $M_1 = 1.5$. We use the von Karman spectrum (4.12) to compute the budget. We observe no substantial difference when the DNS spectrum (4.11) is used instead. There is a good qualitative as well as quantitative match with DNS. The pressure-energy term shows a similar variation as its DNS counterpart, assuming high positive value just behind the shock and monotonically decreasing to negligible levels downstream. The dilatation term from LIA also shows a trend similar to that observed in the DNS data, with a slightly higher negative peak. As a result, the convective term (LHS) has a more pronounced negative peak in LIA than DNS.

The budget of $\overline{u'e'}$ transport equation for Mach 3.5 case (in figure 4.17(b)) shows the same qualitative trends as the lower Mach number budget. The magnitude of the terms are, however, significantly larger and they lead to a higher post-shock turbulent energy flux. We also find that the convection and pressure-energy terms in DNS take identical negative values beyond $x/L_\epsilon = 0.5$, while the pressure-dilatation term is close to zero. The LIA data matches the DNS pressure-dilatation term closely. The linear theory also reproduces the qualitative trends observed in the DNS budget, except for the convection term. The DNS data shows a prominent zero crossing of LHS, which corresponds to the peak $\overline{u'e'}$ at $x/L_\epsilon \simeq 0.12$. LIA prediction for this case has no noticeable peak in the post-shock energy flux profile, as noted earlier. The trends in DNS budget shown in figure 4.17 continue further downstream up to $x/L_\epsilon \sim 2$, beyond which budget data is not available. In particular, the pressure-energy and pressure-dilatation terms have dominant contributions, although with lower magnitudes, and the viscous diffusion/dissipation as well as the conduction terms are relatively small.

4.4.3 Integrated budget

The cumulative contribution of each of the mechanisms to the value of the turbulent energy flux in the region downstream of the shock, can be found out by integrating the transport equation, as carried out for Reynolds stresses in Larsson et al. [20]. The integrated form of (4.22) can be written as

$$\begin{aligned}\left(\widetilde{u_2''e_2''}\right)_x = \left(\widetilde{u_2''e_2''}\right)_{\varsigma=x^*} + \frac{1}{\overline{\rho}\widetilde{u}}\left[\int_{\varsigma=x^*}^{x}(\text{Press.-energy})\,\mathrm{d}\varsigma + \int_{\varsigma=x^*}^{x}(\text{Press.-Dil.})\,\mathrm{d}\varsigma\right] + \\ \frac{1}{\overline{\rho}\widetilde{u}}\left[\int_{\varsigma=x^*}^{x}(\text{Remainder})\,\mathrm{d}\varsigma\right].\end{aligned} \tag{4.24}$$

Here, $\varsigma = x^*$ indicates the point where the mean shock thickness ends (the vertical line at x/L_ϵ=0.16 and 0.06 in figures 4.17(a) and 4.17(b)). The remainder in the above equation represents the terms that have relatively smaller contribution to the budget, for example, the viscous

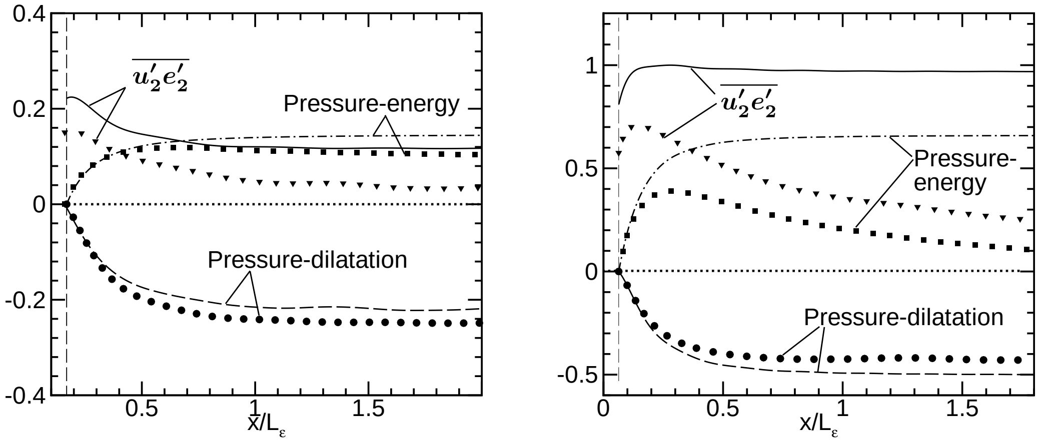

FIGURE 4.18: Integrated budget of transport equation for the turbulent energy flux from DNS (symbols) and LIA considering upstream entropy fluctuations (lines) corresponding to (a) $(M_1,\ M_t,\ Re_\lambda) = (1.5,\ 0.15,\ 40)$ and (b) $(M_1,\ M_t,\ Re_\lambda) = (3.5,\ 0.15,\ 40)$. The vertical line at $x/L = 0$ (dashed) represents end of the mean shock thickness, and the value of $\overline{u_2'e_2'}$ at this point is also shown (dash dot dot). Normalization as described in figure 4.1.

dissipation and conduction terms. The budget of (4.24) computed using the DNS data is plotted in figure 4.18 (symbols) for Mach 1.5 and 3.5 cases. A similar integrated budget of (4.23) computed using LIA for the two Mach numbers is shown for comparison (lines).

The pressure-dilatation term has a negative cumulative effect and it saturates to a constant level due to vanishingly small magnitude of the source term away from the shock. There is a fairly good match between the LIA and DNS values of the integrated pressure-dilatation term, at both Mach numbers. On the other hand, the pressure-energy term has a positive cumulative contribution, with DNS assuming a lower value than the corresponding LIA result. The integrated effect reaches a peak value behind the shock and decreases further downstream, indicating that the pressure-energy term is negative in the far-field. The slope of the integrated pressure-energy term matches the decay rate of the DNS turbulent energy flux away from the shock. This trend is more prominent at the higher Mach number, and implies that the pressure-energy mechanism is primarily responsible for the discrepancy between LIA and DNS in the far-field.

The budget data shows that modeling of the $\overline{u'e'}$ transport equation should focus on the dominant effects of pressure-energy and pressure-dilatation terms, and can neglect the smaller effects of viscosity and non-linear turbulence-turbulence interactions. The linear inviscid theory captures these inviscid phenomena and can be exploited for developing closure models for the source terms. A similar approach was employed for the study of turbulence kinetic energy amplification across a shock wave [5]. The linear inviscid mechanism of shock-unsteadiness damping was found to play a key role and was modeled based on LIA data. The shock-unsteadiness model was subsequently incorporated into one- and two-equation turbulence models, and successfully applied to shock-boundary layer interactions [8]. Note that LIA is able to match the pressure-dilatation effect in the budget of $\overline{u'e'}$ transport equation. The pressure-energy term is systematically overpredicted, the discrepancy increasing with Mach number, and a suitable correction to the LIA-based closure model may be required.

4.5 Summary

This chapter presents a detailed study of the turbulent energy flux generated across a shock wave using linear interaction analysis and direct simulation data. The canonical interaction of homogeneous isotropic turbulence with a nominally normal shock wave is considered, and a purely vortical disturbance field is assumed upstream of the shock. We focus on the streamwise component of the turbulent energy flux and investigate the physics governing its magnitude and direction relative to the shock wave. In the linear theory framework, the upstream disturbance field is Fourier decomposed into two-dimensional planar vorticity waves, each of which interact independently with the shock.

The elementary interaction of individual vorticity waves provide fundamental understanding about the turbulent energy flux generated at the shock wave. The energy flux correlation is a strong function of the shock strength and the incidence angle of the upstream disturbance wave. At low Mach numbers, the majority of the waves yield negative $\overline{u'e'}$ in the near-field, which implies energy transfer back towards the shock wave. The trend is opposite at high Mach numbers, where the near-field turbulent energy transfer is mostly directed away from the shock. Vorticity waves incident at small angles relative to the shock wave lead to propagating disturbances, with slowly varying turbulent energy flux behind the shock. On the other hand, plane wave interactions at high incidence angles result in rapid post-shock variation of $\overline{u'e'}$.

Starting from a low near-field level, the correlation increases to a positive peak value, because of the decay of the negatively correlated acoustic-mode contributions.

Three-dimensional statistics computed by superposition of the individual single-wave solutions also show a rapid variation of the turbulent energy flux. It occurs in the acoustic-adjustment region behind the shock, and is identical to the trends observed in DNS data for a range of shock strengths, turbulent Mach number and Reynolds number based on Taylor microscale. The downstream turbulent energy flux in the DNS attains peak positive value followed by a decay to low levels far away from the shock. In the absence of viscous effects, the linear theory predicts high asymptotic values of the energy flux in the far-field. The far-field correlation is primarily composed of the vortical and entropy components of the disturbance field, while the near-field is dominated by the acoustic mode generated at the shock wave. A budget computed using DNS data shows that the peak values of the energy flux correlation is governed by the pressure-energy and pressure-dilatation source terms in the $\overline{u'e'}$ transport equation. These are dominated by the acoustic mode, which is linear and inviscid in nature, and are reproduced well by linear interaction analysis. There is negligible effect of viscous and non-linear terms in the transport equation to the overall budget.

The effect of entropy and acoustic disturbances in the incoming turbulence on the post-shock turbulent heat flux is estimated using LIA. The focus is on estimating the magnitudes of these effects rather than the exact values, since different realistic flows have different levels and correlations among the different disturbances. Despite clearly over-estimating the amount of acoustic waves present in the DNS, LIA still suggests that the influence of these acoustic waves on the post-shock turbulent heat flux is minimal. The entropy disturbances, on the other hand, are shown to potentially affect the post-shock heat flux by about 10% for the specific DNS case assessed here; this case had almost isentropic incoming turbulence, and thus the effect should be larger in flows with significant entropy disturbances, such as boundary layer flows.

Overall, the linear theory is able to predict the peak turbulent heat flux in the DNS for weak shocks, and the Mach number scaling of $\overline{u'e'}$ in the hypersonic limit. There is also a qualitative match between LIA and DNS data for the entire range of shock strengths. In addition, LIA is able to capture the dominant acoustic mechanism in the budget that are responsible for the rapid post-shock variation of the turbulent energy flux. Advanced physics-based turbulence models can thus be developed based on the linear inviscid theory to predict the peak positive turbulent energy flux behind a shock wave. When applied to shock-boundary layer interaction, the positive values of the energy flux correlation would imply turbulent transfer of internal energy away from the shock. For cases, where an oblique shock is inclined towards the wall, this can add significantly to the wall heat transfer rate. Examples include the reattachment shock in a compression corner interaction. Further, the peak energy flux correlation occurs within one integral length scale of the downstream flow. This corresponds to about one boundary layer thickness past the reattachment point, which is often the region with highest heat transfer to the vehicle surface.

Chapter 5

Modelling of Turbulent Energy Flux

5.1 Introduction

Turbulent energy flux features as an important unclosed correlation in the the Reynolds-averaged mean conservation equation, and assumes high values in shock/boundary-layer interaction. Its conventional modelling in terms of constant turbulent Prandtl number Pr_T is physically inconsistent in the region of strong gradients such as shock waves. A variable Pr_T model proposed by Xiao et al. [11] solves additional differential equations calculate Pr_T at each location in the flow field, which in turn is used to find the turbulent energy flux. Although this modelling approach improves the wall hear flux prediction in shock/boundary-layer interaction, it is still overpredicted in comparison to the experimental data. Bowersox [15] proposed an algebraic model for the turbulent energy flux in supersonic flows, but the model is limited to zero-pressure-gradient boundary layers without shock waves. To the best of our knowledge, there is no direct study which involves modelling of the turbulent energy flux across the shock.

For their ease of implementation, algebraic heat flux models are preferred in computational fluid dynamics (CFD), and are in use in most Reynolds-averaged Navier-Stokes (RANS) simulations. In the current work, we formulate an algebraic model based on the stress limiter approach to predict the peak turbulent energy flux in the shock-region. We also pursue a modelling approach based on the transport equation for turbulent energy flux. Linearized Rankine-Hugoniot

M_1	M_t	Re_λ	$R_{kk}/(2U_1^2)$	$\kappa_\circ L_\epsilon$	$k_0 \times 10^2$	$\epsilon_0 \times 10^3$	$k_1 \times 10^2$	$\epsilon_1 \times 10^3$	$\kappa_\circ \delta_s$
1.28	0.22	38	7.3×10^{-3}	3.9	2.98	1.17	2.42	0.92	1.75
1.50	0.22	38	5.3×10^{-3}	3.9	2.88	1.12	2.42	0.92	1.30
1.87	0.22	39	6.9×10^{-3}	3.8	2.78	1.08	2.42	0.92	1.18
2.50	0.22	40	4.0×10^{-3}	4.3	2.69	1.03	2.42	0.92	0.86
3.50	0.22	40	2.1×10^{-3}	4.3	2.61	1.00	2.42	0.92	0.45
4.70	0.23	42	1.2×10^{-3}	4.3	2.56	0.97	2.42	0.92	0.43
6.00	0.23	42	0.7×10^{-3}	4.4	2.53	0.96	2.42	0.92	0.36

TABLE 5.1: DNS cases from Larsson et al. [20] with mean Mach number, turbulent Mach number and Reynolds number listed at a location just upstream of the shock. The peak wavenumber $\kappa_\circ$ is used to normalize the dissipation length scale L_ϵ and the DNS mean shock thickness δ_s. Also given are the non-dimensional values of turbulence kinetic energy k and dissipation rate ϵ at the inlet station (subscript 0) and just before the shock (subscript 1).

conditions are used to identify the dominant terms in the transport equation contributing to the generation of the turbulent energy flux. The unknown correlations are further modelled based on the linear theory results. The resulting model equation for turbulent energy flux is solved along with the transport equation for turbulence kinetic energy k and its dissipation rate ϵ, to give the jump in energy flux across the shock and its downstream decay. A good match in the streamwise evolution is found upon comparison with the DNS data for a range of upstream Mach numbers.

The chapter is organised as follows. Section 5.2 shows the results obtained for turbulent energy flux using the conventional eddy diffusivity model and realizability models in a canonical STI configuration. An improved algebraic model and a differential-equation based model are discussed in section 5.3.

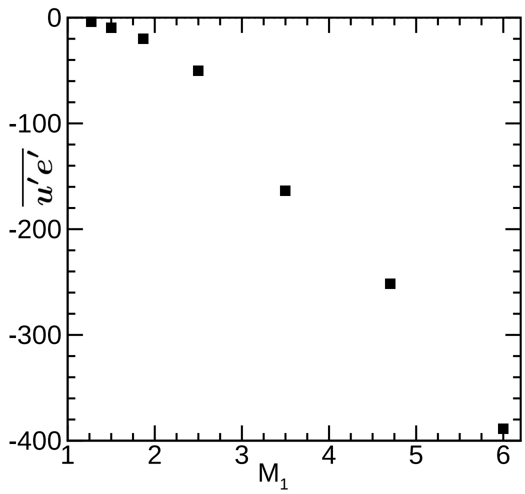

FIGURE 5.1: Peak turbulent energy flux for varying upstream Mach numbers as predicted by conventional model with the shock-thickness taken from the DNS data. The results correspond to turbulent Mach number $M_t = 0.22$ just before the shock. The velocity fluctuations are normalized by the upstream mean velocity and the energy fluctuations are normalized by the product of the downstream mean temperature and the specific gas constant R. The correlation is further normalized by upstream turbulence kinetic energy.

5.2 Existing models for turbulent energy flux

5.2.1 Conventional Modelling

The turbulent energy flux is conventionally modelled using the gradient diffusion hypothesis described in (3.9) as

$$\overline{u'e'} = -\frac{\kappa_T}{\overline{\rho}} \frac{\partial \widetilde{T}}{\partial x}, \tag{5.1}$$

where thermal conductivity κ_T is modelled as $\kappa_T = \mu_T c_v / Pr_T$. In order to compute for the energy flux correlation in the given model problem, the mean flow variables are prescribed as hyperbolic tangent profiles across the shock, with the shock thickness obtained from the DNS data. The values of k and ϵ used in the expression for eddy viscosity are obtained by solving the corresponding differential equations [5] using a fourth order Runge-Kutta (RK4) method, with the inlet boundary condition specified from the DNS data. The resulting values for k and ϵ match well with DNS as reported in earlier works [5, 7].

The value of the energy flux obtained using (3.9) is zero in the region upstream and downstream of the shock due to uniform mean flow temperature on either side of the normal shock. However,

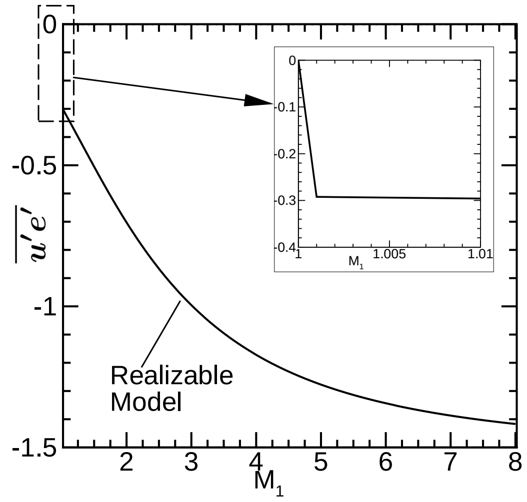

FIGURE 5.2: Variation of peak turbulent energy flux with upstream Mach number as predicted by realizable model with shock thickness taken from the DNS data. The peak value is independent of the shock thickness, which is indicative of a grid-independent solution in a CFD simulation. Normalisation as described in figure 5.1.

the energy flux assumes a peak negative value in the region of the shock, and the peak values obtained for a range of upstream Mach number are shown in figure 5.1. In the limit of $M_1 \to 1$, the value of the energy flux predicted by the model reduces to zero, and with increasing Mach number, the magnitude of the negative peak rises to a value that is almost two orders of magnitude higher than the post-shock DNS predictions. Also, in a CFD framework, this formulation yields a grid-dependent value of the energy flux in the region of the shock From (3.9), $\overline{u'e'} \sim \Delta\widetilde{T}/\delta_s \sim \Delta\widetilde{T}/\Delta x$, where $\Delta\widetilde{T}$ is the jump in the mean temperature across the shock, δ_s is the mean shock thickness and Δx is the local grid resolution. Increasing the grid point density (decreasing Δx) therefore increases the magnitude of the negative peak.

5.2.2 Realizable Model

In canonical shock-turbulence interaction, the Reynolds stress as predicted by the conventional model is given by [5]

$$\overline{\rho u'u'} = -\frac{4}{3}\mu_T\frac{\partial\widetilde{u}}{\partial x} + \frac{2}{3}\overline{\rho}k. \tag{5.2}$$

This modelling approach leads to unphysically high values of TKE in the region of shock due to its proportionality with the mean velocity gradient. The realizability correction limits the value of eddy viscosity in the region of shock through the form $c_\mu = \min(c_\mu^o, \sqrt{c_\mu^o}/s)$ [2], where $s = S/(\epsilon/k)$, $S = \sqrt{(2S_{ij}S_{ji} - (2/3)S_{kk}^2)}$ and $S_{ij} = (\partial\widetilde{u}_i/\partial x_j + \partial\widetilde{u}_j/\partial x_i)/2$. In the region of high gradients such as shock $c_\mu = (\sqrt{c_\mu^o}\epsilon)/(Sk)$ and therefore

$$\mu_T = \frac{\sqrt{3c_\mu^o}}{2}\frac{\overline{\rho}k}{\left|\frac{\partial\widetilde{u}}{\partial x}\right|}. \tag{5.3}$$

Thus the expression for energy flux given by (3.9) reduces to

$$\overline{u'e'} = -\frac{\sqrt{3c_\mu^0}}{2}\frac{kc_v}{Pr_T\left|\frac{\partial\widetilde{u}}{\partial x}\right|}\frac{\partial\widetilde{T}}{\partial x}, \tag{5.4}$$

in the shock region.

The value of TKE as well as the mean variables required for the above formulation are obtained as described in the previous section. Similar to the conventional model, the realizable model yields a zero value of energy flux outside the region of shock. However, inside the shock region, a peak negative value is obtained as per (5.4). This peak energy flux value for varying Mach number is plotted in figure 5.2. For almost all Mach numbers, the realizable model predicts a negative energy flux in the shock region, but the magnitude is restricted due to the realizability constraint, and is of the same order as the post-shock DNS value. Contrary to the eddy viscosity formulation, the realizability limiter yields a peak value of energy flux which is independent of the shock thickness assumed. This is because $\overline{u'e'} \sim (\Delta\widetilde{T}/\delta_s)/(\Delta\widetilde{u}/\delta_s) \sim \Delta\widetilde{T}/\Delta\widetilde{u}$, assuming k to be finite, as predicted in Sinha et al. [5]. Thus, in a real CFD simulation, the peak value in the shock region will be insensitive to grid refinement. In the limit of $M_1 \to 1$, the realizable model switches to the conventional model formulation and predicts a value of zero energy flux as shown in the inset figure. In the limit of $M_1 \to \infty$, the model saturates to a negative limiting value, a trend similar to the DNS data, but opposite in sign.

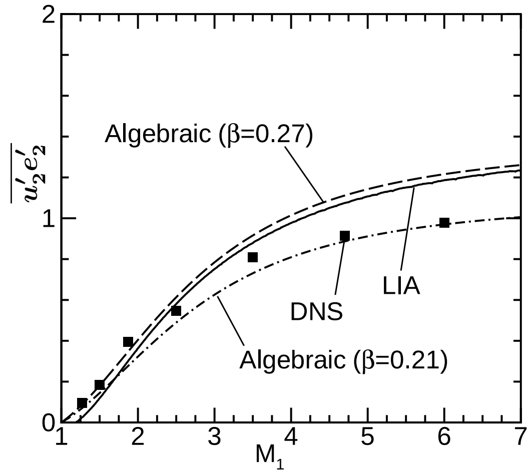

FIGURE 5.3: Variation of $\overline{u'e'}$ with upstream Mach number as per new algebraic formulation. Also seen are the DNS values of energy flux extrapolated to the shock center and the far-field LIA results. Normalisation as described in figure 5.1.

5.3 New physics-based models

5.3.1 Algebraic heat flux limiter model

We use linear interaction analysis results to propose an algebraic model for turbulent energy flux at the shock as

$$\overline{u'e'} = \beta \frac{kc_v}{\left|\frac{\partial \widetilde{u}}{\partial x}\right|} \frac{\partial \widetilde{T}}{\partial x}. \tag{5.5}$$

This form is similar to the realizability constraint shown in (5.3), with β as an unknown modelling parameter. From the mean energy conservation equation across the shock, we can write

$$\widetilde{u} \left|\frac{\partial \widetilde{u}}{\partial x}\right| = c_p \frac{\partial \widetilde{T}}{\partial x}, \tag{5.6}$$

where c_p is the specific heat at constant pressure. Substituting the above equation in (5.5) yields

$$\overline{u'e'} = \frac{\beta k \widetilde{u}}{\gamma}, \tag{5.7}$$

where the turbulent energy correlation is seen to be proportional to turbulent kinetic energy. This is physically consistent with the linear theory results that show all correlations generated across the shock to be directly proportional to the upstream TKE.

Further, the normalised expression for energy flux can be written as

$$\overline{u'e'}|_{Norm.} = \frac{\overline{u'e'}}{R\widetilde{u}_1 \widetilde{T}_2 \frac{k_1}{\widetilde{u}_1^2}}, \tag{5.8}$$

where R is the specific gas constant. The energy flux is normalized in this manner throughout this work, and the subscript $Norm.$ is dropped for convenience. Using (5.7) with the upstream values of k and U, along with (5.8), simplifies the above expression to

$$\overline{u'e'} = \beta \frac{M_1^2}{T_r}, \tag{5.9}$$

where T_r is the mean temperature ratio across the shock. In the high Mach number regime, this ratio is proportional to M_1^2, and the above expression obtains a limiting value

$$\overline{u'e'} = \beta \frac{(\gamma+1)^2}{2\gamma(\gamma-1)}. \tag{5.10}$$

A similar trend is observed in DNS and LIA, where the peak turbulent energy flux saturates at high Mach numbers. In order to find the value of the modelling parameter β, we equate (5.10) to the LIA far-field limiting value of 1.4. This gives a value of $\beta = 0.27$ for $\gamma = 1.4$. However, in the limit of $M_1 \to 1$, the energy flux attains a value equal to 0.27, which is physically incorrect. On the contrary, the energy flux predicted by the conventional model in the $M_1 \to 1$ limit is zero (as $\overline{u'e'}$ is proportional to the mean temperature gradient), which is consistent with the DNS and LIA predictions. We therefore propose a low Mach number correction of the form

$$\beta' = (1 - e^{1-M_1})\beta, \tag{5.11}$$

which yields $\beta' = 0$ as $M_1 \to 1$ and $\beta' \to \beta$ as $M_1 \to \infty$.

Figure 5.3 shows the model predictions of the peak turbulent energy flux for a range of upstream Mach numbers. Also shown in the figure are the downstream DNS values of energy flux extrapolated to the shock center and the far-field LIA values. The model matches well with DNS for $M_1 < 2$, and for higher Mach numbers, it is close to LIA and overpredicts the DNS values. The modelling parameter β can also be obtained upon equating (5.9) to the value of turbulent energy flux at high Mach number $M_1 = 6$. This yields a value of $\beta = 0.21$, and the resulting turbulent energy flux value for a range of upstream Mach number is also shown in figure 5.3. This trend is slightly lower than the DNS and LIA couterpart for most Mach numbers.

5.3.2 Differential-equation based model

In this section, we propose a differential-equation based model to predict the turbulent energy flux in STI. The model development is based on the linear theory approximations, and it builds on the fact that the peak turbulent energy flux behind the shock is reproduced well by LIA. The model is developed in two parts. The first part attempts to predict the peak turbulent energy flux generated behind the shock, and the second part reproduces the decay of the energy flux further downstream. The model is developed in conjunction with the model equations for TKE and its dissipation rate proposed by Sinha et al. [5]. The closure coefficients are obtained from the LIA results, as in the earlier works [5–7], and the model predictions are compared with available DNS data [20].

The equation for the conservation of total enthalpy across the shock wave can be written in terms of the shock-normal velocity component u_n as

$$\frac{\partial h_e}{\partial x} + u_n \frac{\partial u_n}{\partial x} = 0, \tag{5.12}$$

where h_e is the enthalpy. For an unsteady distorted shock wave of the form presented in figure 3.1, $u_n \simeq \overline{u} + u' - \xi_t$, which assumes small deviation of the shock wave from its mean location. Here, ξ represents the shock displacement from its mean position, and ξ_t represents the local streamwise velocity of the shock wave; see Sinha [7] for further details. Linearising the above equation in terms of fluctuations in enthalpy h' and streamwise velocity u', we get

$$\frac{\partial h'}{\partial x} + \overline{u}\frac{\partial u'}{\partial x} + u'\frac{\partial \overline{u}}{\partial x} - \xi_t \frac{\partial \overline{u}}{\partial x} = 0. \tag{5.13}$$

Taking a moment with u' and Reynolds averaging yields a differential equation for the energy flux correlation.

$$\gamma \frac{\partial}{\partial x}\overline{u'e'} = -\overline{u'^2}\frac{\partial \overline{u}}{\partial x} + \overline{u'\xi_t}\frac{\partial \overline{u}}{\partial x} - \overline{u}\frac{\partial}{\partial x}\frac{\overline{u'^2}}{2} + \overline{h'\frac{\partial u'}{\partial x}}, \tag{5.14}$$

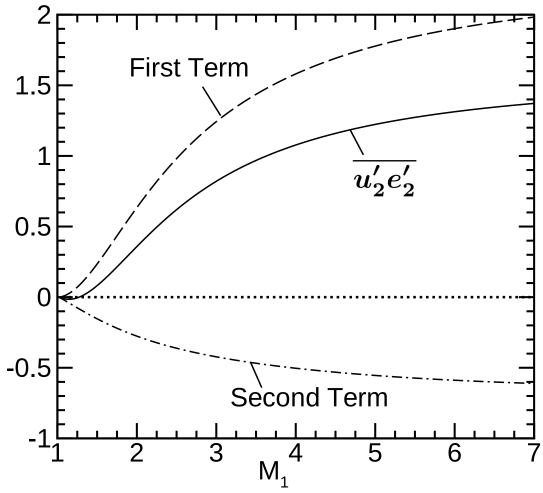

FIGURE 5.4: Variation of $\overline{u'_2e'_2}$ with upstream Mach number as predicted by (5.15) along with the individual contributions of the source terms. Normalisation as described in figure 5.1.

where the enthalpy fluctuations are replaced by the internal energy fluctuations via $h' = \gamma e'$. The first term on the RHS represents the generation of turbulent energy flux due to mean compression in the shock wave, and the second term brings in the shock-unsteadiness effect. The change in the streamwise Reynolds stress across the shock contributes to the turbulent energy flux via the third term on the RHS. The last term is a correlation of the enthalpy fluctuations with the change in the streamwise velocity fluctuations across the shock.

The first two source terms are analogous to the production and the shock-unsteadiness damping terms in the TKE equation presented in Sinha et al. [5]. We follow their modelling approach to write $\overline{u'\xi_t} = b_1\overline{u'^2}$, which is based on the assumption that the unsteady shock oscillations are caused by the incoming velocity fluctuations. The streamwise Reynolds stress is then closed in terms of the turbulence kinetic energy by considering its isotropic form i.e., $\overline{u'^2} = 2k/3$ [5]. The final model equation for the turbulent energy flux thus takes the form

$$\frac{\partial}{\partial x}\left(\overline{u'e'}\right) = -\frac{2(1-b_1)}{3\gamma}k\frac{\partial \overline{u}}{\partial x} - \frac{1}{3\gamma}\overline{u}\frac{\partial k}{\partial x}, \tag{5.15}$$

where $b_1 = 0.4 + 0.6\exp(2(1 - M_1))$. The last term is dropped from the equation for want of an adequate closure approximation.

The value of turbulent energy flux is obtained by numerically integrating (5.15) over prescribed hyperbolic tangent shock profiles of the mean variables. Figure 5.4 shows the value of turbulent energy flux obtained across the shock for varying upstream Mach numbers. The correlation takes a value of zero as $M_1 \to 1$, which is physically consistent with negligible turbulent energy flux across very weak shocks. With increase in upstream Mach number, the energy flux gradually rises to saturate in the $M_1 \to \infty$ limit. The contribution of both the terms on the RHS of (5.15) are also shown in the figure. While the first model term in the above equation generates a positive turbulent energy flux across the shock wave, the second term has a negative contribution to the energy flux correlation. The magnitude of the first term is significantly higher than the second for all upstream Mach numbers, therefore yielding a positive value of the energy flux.

Now consider the differential equation governing the jump in TKE at the shock given by the shock-unsteadiness model [5]

$$\overline{\rho}\widetilde{u}\frac{\partial k}{\partial x} = -\frac{2}{3}\overline{\rho}k\frac{\partial \widetilde{u}}{\partial x}(1-b_1). \tag{5.16}$$

Also, from the mean energy conservation equation across the shock, we can write

$$\widetilde{u}\left|\frac{\partial \widetilde{u}}{\partial x}\right| = c_p\frac{\partial \widetilde{T}}{\partial x}. \tag{5.17}$$

Using the above two equations, (5.15) can be written as

$$\frac{\partial}{\partial x}\left(\overline{u'e'}\right) = c_{ue}\left(\frac{k}{\widetilde{\overline{u}}}\right)c_p\frac{\partial \widetilde{T}}{\partial x}, \tag{5.18}$$

where $c_{ue} = 4(1-b_1)/(9\gamma)$ and $\widetilde{u} \simeq \overline{u}$. This equation is compact with only one modelled term governing the value of energy flux across the shock. Moreover, similar to the conventional form discussed earlier, the energy flux is modelled in terms of the gradient in the mean temperature.

Figure 5.5 compares the energy flux values as predicted by (5.18) for varying upstream Mach numbers with the far-field LIA results and the downstream DNS values of energy flux extrapolated to the shock center. The model prediction attains a value of zero as $M_1 \to 1$ and saturates to a positive limiting value at high Mach numbers similar to the DNS and LIA results. A good match is observed with the LIA results, and the model overpredicts in comparison with the DNS data for higher upstream Mach numbers.

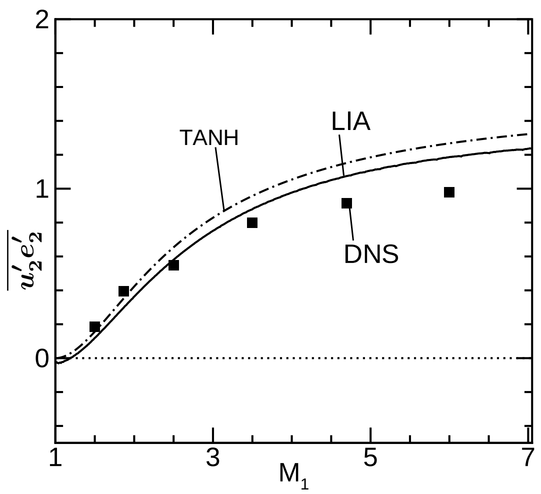

FIGURE 5.5: Variation of $\overline{u_2'e_2'}$ with upstream Mach number as predicted by (5.18) using the Runge-Kutta integration method (denoted as TANH). Also shown are the corresponding DNS values extrapolated to shock center and far-field LIA results. Normalisation as described in figure 5.1.

In order to model the decay in the turbulent energy flux behind the shock, we look at the mechanisms responsible for its post-shock evolution. Quadros et al. [76] study the budget of $\overline{u'e'}$ transport equation in the linear inviscid framework, which yields

$$\overline{\rho}\,\widetilde{u}\frac{\partial}{\partial x}\overline{u'e'} = \underbrace{-\ \overline{e'\frac{\partial p'}{\partial x}}}_{\text{Press. energy}}\ \underbrace{-\ \overline{p}\,\overline{u'\frac{\partial u_j'}{\partial x_j}},}_{\text{pressure-dilatation}} \tag{5.19}$$

i.e., the post-shock turbulent energy flux is determined by the pressure-energy and pressure-dilatation mechanisms. In the region behind the shock ($0 < x/L_\epsilon < 1$), these processes are dominated by the acoustic mode, for which the thermodynamic fluctuations can be assumed to be approximately isentropic. Therefore, the pressure-energy term can be written as [76]

$$-\overline{e'\frac{\partial p'}{\partial x}} = -\frac{1}{\gamma\overline{\rho}}\frac{\partial}{\partial x}\left(\frac{\overline{p'^2}}{2}\right),$$

which corresponds to the streamwise variation of pressure variance. The pressure-dilatation term in (5.19) is proportional to the mean post-shock pressure, and the $\overline{u'(\partial u_j'/\partial x_j)}$ correlation can be expanded as

$$\overline{u'\frac{\partial u_j'}{\partial x_j}} = \frac{\partial}{\partial x}\frac{\overline{u'^2}}{2} + \overline{u'\frac{\partial v'}{\partial y}} + \overline{u'\frac{\partial w'}{\partial x}}.$$

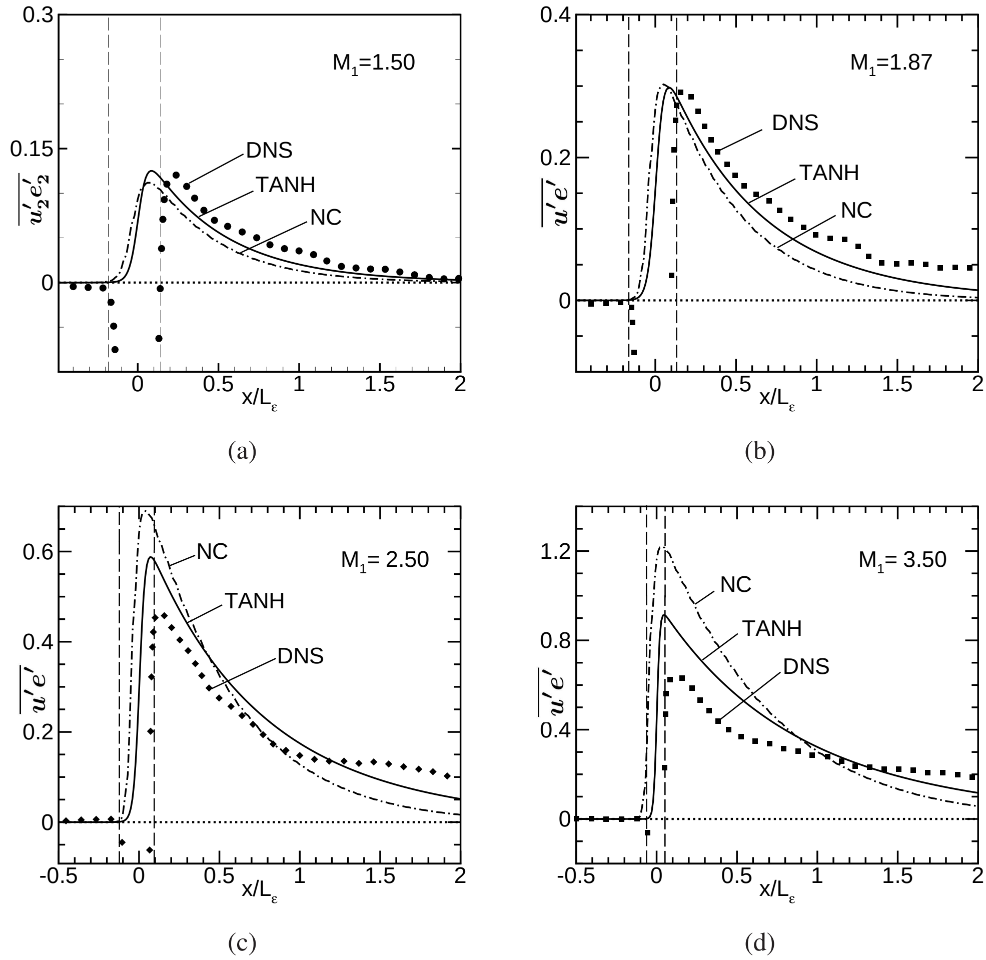

FIGURE 5.6: Streamwise variation of $\overline{u'e'}$ as computed using Runge-Kutta method (line, denoted as TANH) and the Lax-Friedrich scheme (dash-dot) for the nonconservative (NC) form of transport equation, compared with the DNS data (symbols) for four upstream Mach numbers. The vertical lines near $x/L_\epsilon = 0$ represent the mean shock thickness. Normalisation as described in figure 5.1.

The first term on the RHS represents the buildup of streamwise Reynolds stress as a result of the acoustic decay, and can be argued to be positive in the acoustic-adjustment region behind the shock.

Data from DNS and LIA (see chapter 6) show that the pressure variance $\overline{p'^2}$ decays exponentially behind the shock, and the same can be expected for $\overline{u'e'}$. This decay can be modelled by adding a term proportional to $-\overline{u'e'}/L$ to the RHS of the $\overline{u'e'}$ transport equation. Here, the characteristic decay length scale L is taken as the dissipation length scale L_ϵ, which is representative of the large acoustic scales in the turbulence field. The full model equation for the energy flux thus takes the following form

$$\frac{\partial}{\partial x}\left(\overline{u'e'}\right) = c_{ue}\left(\frac{k}{\widetilde{u}}\right)c_p\frac{\partial \widetilde{T}}{\partial x} - c_2\frac{\overline{u'e'}}{L_\epsilon}, \tag{5.20}$$

where $c_2 = 0.3 + 3\exp(1 - M_1)$ is a modelling parameter based on the DNS data.

Figure 5.6 shows the streamwise variation of the turbulent energy flux for four upstream Mach numbers, obtained by numerically integrating (5.20) using the fourth-order Runge-Kutta (RK4) method. The shock is specified as a hyperbolic tangent profile of the mean flow variables; it is centered at $x = 0$, with the thickness obtained from the DNS data (shown using two vertical lines). The turbulent energy flux in the incoming flow is set to zero for the purely vortical turbulence upstream of the shock wave.

The model predicts a peak positive value of the correlation across the shock, and we observe a good match between the model prediction and the DNS data for M_1 = 1.5 and 1.87. For the Mach 2.5 case, the model overpredicts the peak $\overline{u'e'}$ observed in DNS, but matches the post-shock decay rate up to $x = L_\epsilon$. At the highest Mach number interaction considered here ($M_1 = 3.5$), the model overpredicts the peak value as well as the decay rate behind the shock for $x < L_\epsilon$. Further downstream, we see a systematic under-prediction for all Mach numbers, and it is most prominent for the Mach 2.5 case. This can be attributed to the fact that the majority of the pressure fluctuations decay within $x \simeq L_\epsilon$, and further decay of $\overline{u'e'}$ is possibly governed by viscous dissipation. The current model, without any viscous effects, is unable to reproduce $\overline{u'e'}$ outside the acoustic decay region behind the shock.

5.4 Numerical simulation

The model predictions presented above are obtained by numerically integrating the model equations for specified mean flow profiles across a shock wave. The integration step size is kept small so that the results are devoid of numerical error. On the other hand, in computational fluid dynamic simulations presented below, the mean flow variables at a shock wave are computed as part of the solution, and are prone to numerical error. In this section, we assess the effect of the numerical error on the turbulent energy flux prediction and device ways to eliminate them.

5.4.1 Numerical methodology

We solve the one-dimensional Reynolds-averaged Navier-Stokes equations for the mean flow, and the shock-unsteadiness k-ϵ model from Sinha et al. [5] is used for turbulence closure. The diffusive fluxes are neglected because their contribution is expected to be small in the current shock-turbulence interaction [66]. The governing equations are cast in a non-dimensional form, where the upstream mean speed of sound and mean density are taken as the characteristic quantities. The most energetic wave number $\kappa_0 = 4$ in the incoming turbulence field is taken as the characteristic length scale.

The mean conservation equations along with the $k-\epsilon$ and $\overline{u'e'}$ model equations are solved using the finite volume approach, where the equations are written in a vector form.

$$\frac{\partial}{\partial t}\underbrace{\left\{\begin{matrix} \overline{\rho} \\ \overline{\rho}\,\widetilde{u} \\ \widetilde{E} \\ \overline{\rho}\,k \\ \overline{\rho}\,\overline{\epsilon} \\ \overline{\rho}\,\overline{u'e'} \end{matrix}\right\}}_{\text{[U]}} + \frac{\partial}{\partial x}\underbrace{\left\{\begin{matrix} \overline{\rho}\,\widetilde{u} \\ \overline{\rho}\,\widetilde{u}^2 + \overline{p} \\ \widetilde{u}(\widetilde{E} + \overline{p}) \\ \overline{\rho}\,\widetilde{u}\,k \\ \overline{\rho}\,\widetilde{u}\,\epsilon \\ \overline{\rho}\,\widetilde{u}\,\overline{u'e'} \end{matrix}\right\}}_{\text{[F]}} = \underbrace{\left\{\begin{matrix} 0 \\ 0 \\ 0 \\ -(2/3)\overline{\rho}k(\partial\widetilde{u}/\partial x)(1 - b_1') - \overline{\rho}\epsilon \\ -(2/3)c_1\overline{\rho}\epsilon(\partial\widetilde{u}/\partial x) - c_{\epsilon 2}\overline{\rho}(\epsilon^2/k) \\ c_{ue}(k/\widetilde{u})c_p(\partial\widetilde{T}/\partial x) - c_2(\overline{u'e'}/L_\epsilon) \end{matrix}\right\}}_{\text{[S]}}. \tag{5.21}$$

Here, [U] is the vector of the conserved variables, [F] is the vector containing the inviscid fluxes and [S] is the vector containing the source terms, where tilde represents Favre averaging and $\widetilde{E}$ is the mean total energy.

The inviscid fluxes at cell faces are evaluated using the Lax-Friedrich scheme and the turbulent source terms are evaluated at the cell centers. The mean flow gradients in the production terms are discretized using a second-order accurate central difference scheme. Explicit time integration is achieved using the first order forward Euler method. The Lax-Friedrich method is more dissipative than the modified Steger Warming method used by Sinha and Balasridhar [66], but can produce identical results with larger number of grid points.

We simulate shock-turbulence interaction for varying shock-strength, i.e. Mach number ranging from low supersonic to hypersonic values (see table 5.1). The turbulent Mach number M_t just upstream of the shock wave is taken as 0.22. The normalized turbulence kinetic energy is thus given by $k_1 = M_t^2/2$, where subscript 1 represents shock-upstream values. The Reynolds number based on Taylor microscale $Re_\lambda = \lambda u'_{rms}/\nu = 40$ [77], where $u'_{rms} = \sqrt{2k/3}$. The Taylor microscale is given by $\lambda = \sqrt{10\nu k/\epsilon}$, where ν is the mean kinematic viscosity of the fluid. The turbulent dissipation rate ϵ can thus be computed as

$$\epsilon_1 = \frac{5}{\sqrt{3}}\left(\frac{M_t^3}{\kappa_0\lambda}\right)\frac{1}{Re_\lambda}, \tag{5.22}$$

where $\kappa_0\lambda = 0.84$.

The computational domain extends from $\kappa_\circ x = -7.6$ to 29.6, with the shock centered at $x = 0$. The homogeneous turbulence upstream of the shock follows decay relations

$$\begin{aligned} \widetilde{u}\frac{dk}{dx} &= -\epsilon, \\ \widetilde{u}\frac{d\epsilon}{dx} &= -c_{\epsilon 2}\frac{\epsilon^2}{k}, \end{aligned}$$

with solution given by

$$\begin{aligned} k_0 &= k_1\left[1 + \kappa_0 x_{sh}\frac{(c_{\epsilon 2}-1)}{M_1}\frac{\epsilon_0}{k_0}\right]^{\frac{1}{c_{\epsilon 2}-1}}, \\ \epsilon_0 &= \epsilon_1\left[1 + \kappa_0 x_{sh}\frac{(c_{\epsilon 2}-1)}{M_1}\frac{\epsilon_0}{k_0}\right]^{\frac{c_{\epsilon 2}}{c_{\epsilon 2}-1}}, \end{aligned} \tag{5.23}$$

where k_0 and ϵ_0 are the inlet values obtained from the shock upstream values (see table 5.1). The same values are used to initialize the turbulence variables in the simulation. Here, $c_{\epsilon 2} = 1.2$ and $\kappa_0 x_{sh} = 6.83$. The mean flow quantities are initialized to Rankine-Hugoniot jump conditions at the shock at $x = 0$. At the exit boundary, we specify zero gradient boundary condition for all the mean flow and turbulence variables.

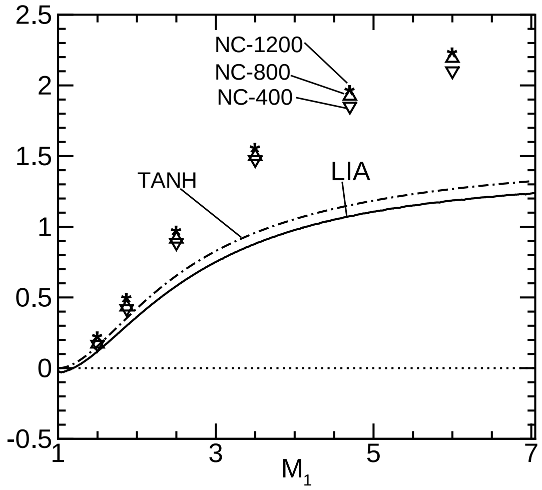

FIGURE 5.7: The post-shock turbulent energy flux as computed using the Lax-Friedrich scheme applied to the nonconservative (NC) form of the model equations, compared with the Runge-Kutta method (denoted as TANH) and linear theory (LIA) predictions. Solution computed on different grid sizes: 400 (gradient), 800 (triangle), 1200 (star). Normalisation as described in figure 5.1.

5.4.2 Numerical results

The mean flow and the model equations are solved using 800 points equally spaced along the shock-normal direction. The jump in the turbulent energy flux for varying Mach numbers is presented in figure 5.7. For low Mach numbers upto $M_1 = 2$, there is a good match between the Lax-Friedrich and the RK4 solution reproduced from figure 5.5. However, at higher Mach numbers, the numerical scheme overpredicts the jump in the turbulent energy flux. The reason for this can be attributed to the error in the numerical solution computed at the shock. The earlier results obtained for a specified tangent hyperbolic shock profile is devoid of such numerical error. The numerical error is not found to decrease with successive grid refinement; see results obtained using 400, 800 and 1200 grid points in figure 5.7. A similar trend is observed with the $k - \epsilon$ solution at shock waves [66] and is discussed below.

The streamwise variation of the turbulent energy flux obtained by solving (5.20) numerically is shown in figure 5.6. The results are compared with the RK4 method and the corresponding DNS data. For the low Mach number case of $M_1 = 1.50$, both the RK4 and the numerical solution match well and are comparable to the DNS data. With increasing Mach number, the numerical solution deviates from the RK4 result both in the jump across the shock and the downstream evolution. This deviation once again can be attributed to the nonconservative error in the source terms of the transport equation for k, ϵ and $\overline{u'e'}$.

Sinha and Balasridhar [66] studied the numerical issues involved while solving shock-turbulence interaction using the shock-unsteadiness k-ϵ equations. It was found that for shock capturing simulations, like those in this work, the nonconservative nature of the production terms can result in large numerical error at shock waves. The inviscid flux terms, on the other hand, are in conservative form. In a finite-volume approach, the fluxes are evaluated at cell interfaces. The corresponding truncation error involves higher-order derivatives of the flow variables, which take large values in the shock wave. It is shown that the error from adjacent cells cancel at the common interfaces when all the finite volume cells spanning the shock wave are taken together. The net error across the shock wave is therefore a function of the higher-order derivatives evaluated in a region of smooth flow solution, outside the shock wave. On successive grid refinement, the leading-error term vanishes and the solution tends towards the exact integral. Further details can be found in the appendix of Sinha and Balasridhar [66].

The source terms in both the k and ϵ equations involve flow derivatives that are evaluated using a symmetric second-order discretization Sinha and Balasridhar [66]. The corresponding truncation error involves third and higher-order derivatives of velocity, pressure and temperature. On integration over a finite volume cell, the corresponding error term thus involves integration of these higher order derivatives. The leading error term scales as $1/\delta^3$, where δ is the computed shock thickness, and hence the error takes large values in the region of a flow discontinuity. When all the finite volume cells spanning the shock wave are taken together, these error terms from the individual cells add up and appear as numerical volume sources. Unlike the conservative flux terms, the telescopic effect of error cancellation between adjacent cells is absent in the nonconservative source terms [66]. This leads to significant error that are comparable or larger than the physical production at the shock waves. Also, the numerical error does not decrease in magnitude with successive grid refinement as observed for smooth solutions.

To restrict the truncation errors at shock waves, Sinha and Balasridhar [66] proposes an alternative form of the shock-unsteadiness k-ϵ equations obtained by transforming the turbulence variables. Conserved quantities involving k and ϵ are formulated and transport equations for

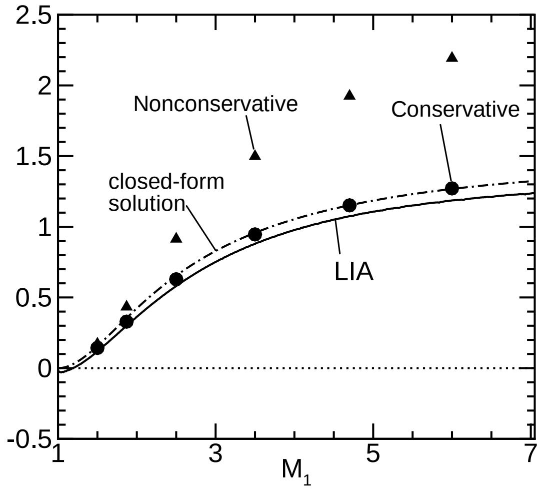

FIGURE 5.8: Comparison of the turbulent energy flux computed using the Lax-Friedrich scheme applied to the conservative and nonconservative forms of the model equations with the closed-form solution and the far-field LIA values. Normalisation as described in figure 5.1.

these new variables are derived. The new $k - \epsilon$ equations capture identical physics as the original shock-unsteadiness model, but are free of the nonconservative source terms, and therefore show dramatic improvement in numerical accuracy. Here, we follow a similar approach for the $\overline{u'e'}$ model equation given in (5.20) to derive the corresponding conservative form.

5.4.3 Conservative formulation

A conservative formulation of the governing equations for k and ϵ is derived by Sinha and Balasridhar [66], and is given as

$$\overline{\rho}\,\widetilde{u}\frac{\partial f}{\partial x} = -\rho\epsilon\rho^{-(2/3)c_o}, \tag{5.24}$$

$$\overline{\rho}\,\widetilde{u}\frac{\partial g}{\partial x} = \frac{-c_{\epsilon 2}\epsilon^2}{k}\rho^{1-(2/3)c_1}, \tag{5.25}$$

where $c_o = 1-b_1'$ and $b_1' = 0.4(1-exp(1-M_1))$, and the transformed variables $f = k\rho^{-\frac{2}{3}c_o}$ and $g = \epsilon\rho^{-\frac{2}{3}c_1}$ are based on the closed form solution of the original equations. Solving the above two equations instead of their corresponding nonconservative forms significantly improved the prediction of TKE and its dissipation rate in canonical STI; see Sinha and Balasridhar [66] for details.

A closed form solution for energy flux can be obtained by writing (5.18) as

$$\frac{\partial}{\partial x}\left(\overline{u'e'}\right) = \frac{c_{ue}c_p}{\overline{\rho}\widetilde{u}} f \rho^{(2c_0/3+1)}\frac{\partial \widetilde{T}}{\partial x}, \tag{5.26}$$

where f is a conserved variable across the shock [66]. This equation reduces to

$$\frac{\partial}{\partial x}\left(\overline{u'e'}\right) = -c_{ue} f (\overline{\rho}\,\widetilde{u})^{2c_0/3}\widetilde{u}^{-2c_0/3}\frac{\partial \widetilde{u}}{\partial x}, \tag{5.27}$$

using the total energy conservation across a shock wave. Integrating between the shock-upstream (subscript 1) and shock-downstream (subscript 2) locations yields

$$\overline{u_2'e_2'} = A_1\left[\widetilde{u}_2^{1-2c_0/3} - \widetilde{u}_1^{1-2c_0/3}\right], \tag{5.28}$$

where $A_1 = -c_{ue} f(\overline{\rho}\widetilde{u})^{2c_0/3}/(1-2c_0/3)$ is a conserved quantity across the shock. The value of the energy flux predicted by this closed form solution is plotted for varying upstream Mach numbers in figure 5.8. A good match is observed with the solution obtained by solving the corresponding differential equation (5.18) using RK4 method as shown in figure 5.7.

The closed form solution is used to define a new variable

$$h = \overline{u'e'} - A_1\widetilde{u}^{1-2c_0/3}, \tag{5.29}$$

and write the model equation for $\overline{u'e'}$ as

$$\frac{\partial h}{\partial x} = -c_2\frac{\overline{u'e'}}{L_\epsilon}, \tag{5.30}$$

which captures the same physics as the original equation (5.20), but is numerically more robust at shock waves than the former. This is because the nonconservative source terms involving the mean temperature derivative is eliminated from the transport equation. Numerical implementation of the conservative model equations follow the same method as described in (5.21), with k, ϵ and $\overline{u'e'}$ replaced by f, g and h, respectively. The source term vector $[S]$ is appropriately modified as per the right-hand sides of (5.24), (5.25) and (5.30). The initial and boundary conditions are recast in terms of the transformed variables, and the turbulence variables k, ϵ and

$\overline{u'e'}$ are obtained from the solution by invoking the reverse transformation.

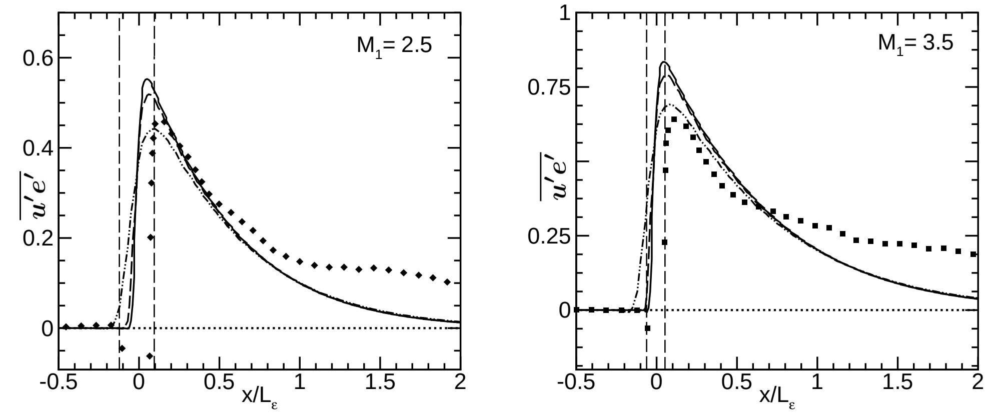

(a) (b)

FIGURE 5.9: Streamwise variation of $\overline{u'e'}$ as computed using the conservative form of the model equations are compared with the DNS data (symbols) for two upstream Mach numbers. The vertical lines near $x/L_\epsilon = 0$ represent the mean shock thickness, and the Lax-Friedrich scheme is employed on three different grids: 400 (dash dot dot), 800 (dash) and 1200 (solid). Normalisation as described in figure 5.1.

Figure 5.8 shows the peak turbulent energy flux for varying upstream Mach number obtained by numerically solving the conservative form of the model equations. The results match exactly with the closed form solution and are a significant improvement over the nonconservative results. Figure 5.9 shows the streamwise evolution of the turbulent energy flux computed on different numerical grids. The data corresponds to the higher Mach number cases, where the nonconservative error is most prominent. The results show a systematic grid convergence, with the difference in the peak $\overline{u'e'}$ values diminishing with successive grid refinement. The model predictions also compare well with the DNS data up to $x \simeq L_\epsilon$ for the Mach 2.5 interaction and upto $x \simeq 0.7L_\epsilon$ for the high Mach number case. Turbulent energy flux predicted for the Mach 1.5 and 1.87 flows are almost identical to those in figure 5.6, and they are also comparable to the post-shock DNS data.

5.5 Conclusion

In this paper, we look at various modelling strategies to predict the turbulent energy flux generated in canonical shock-turbulence interaction. Application of conventional $k - \epsilon$ models based on the gradient diffusion hypothesis yields large negative value of energy flux in the shock region, which rises drastically with increasing Mach number and grid refinement. These values are much higher in magnitude than the post-shock DNS predictions, which yield a low positive energy flux. Realizable model also predicts negative values of the energy flux in the shock region, but the peak value is limited by the realizability constraint. A new model is proposed using results from linear interaction analysis, which has been shown to capture the key physics of turbulent energy flux generated at a shock wave. The model is based on a heat-flux limiter formulation similar in form to the realizability constraint and is able to predict the peak turbulent energy flux over a range of Mach numbers. We also develop a transport equation model for the turbulent energy flux, based on the linear and inviscid interaction of turbulent fluctuations with a shock wave. The model parameters are taken from the well-established shock-unsteadiness $k - \epsilon$ model,and a numerically robust form is proposed by eliminating the nonconservative source terms in the equation. The new physics-based model is found to predict DNS values of the peak energy flux correlation and the acoustic decay downstream of the shock wave.

Chapter 6

Velocity-Temperature Correlation Coefficient

6.1 Introduction

A shock wave impinging on a supersonic boundary layer may lead to the separation and reattachment of the boundary layer, which in turn causes a high localized heat transfer to the surface [78, 79]. When the incoming boundary layer is turbulent, the peak heat transfer around the shock can be an order of magnitude higher than that in the incoming flow [1]. Turbulent enthalpy flux $\widetilde{u_j''h''}$ or the turbulent heat flux $\widetilde{u_j''T''}$, an important term in the mean energy conservation equation, is modelled in terms of the gradient diffusion hypothesis as described in section 5.2.1. The standard modelling approach is to follow the strong Reynolds analogy proposed by Morkovin [9] and assume that the velocity and temperature fluctuations are anti-correlated, i.e., that the correlation coefficient

$$R_{uT} = \frac{\widetilde{u''T''}}{\sqrt{\widetilde{u''^2}}\sqrt{\widetilde{T''^2}}} \tag{6.1}$$

is equal to -1, which corresponds to a value of the turbulent Prandtl number Pr_T = 1 [70].

The strong Reynolds analogy assumes that the total temperature fluctuations in a flow are negligible compared to the fluctuations in the static temperature and the flow kinetic energy. This is not true in the presence of shock waves. For example, Mahesh et al. [10] showed that considerable total temperature fluctuations are generated in the vicinity of a shock. As a consequence, they found that R_{uT} varied significantly across and behind the shock. The variation in R_{uT} could imply that the turbulent Prandtl number Pr_T used in standard models should vary around a shock as well. Indeed, some variable-Pr_T models have been found to improve the peak surface heat flux prediction in SBLI compared to conventional models [11].

A thorough study of R_{uT} is therefore important for high-speed flows with shock waves, and is the focus of the current chapter. Specifically, the objective is to study the variation of R_{uT} with flow parameters like the shock strength (characterized by the upstream mean Mach number M_{in}), the turbulence intensity (characterized by the turbulent Mach number $M_{t,\text{in}}$), and the Reynolds number Re (that characterizes viscous effects) in canonical shock-turbulence interaction. We also study the effect of different types of inflow disturbance fields, namely, vorticity, entropy, acoustic and their combination, on R_{uT}. Most importantly, we aim at understanding the physics that determines R_{uT} and its variation downstream of the shock, which could provide crucial insight towards developing closure models for the turbulent heat flux in the shock region. Note that we use the subscript in in this chapter for convenience in order to describe the shock-upstream parameters.

Section 6.2 describes R_{uT} variation for a purely vortical upstream turbulence. The LIA results are compared with the DNS data. The match between the two is explained by decomposing R_{uT} in terms of contribution from the Kovasznay modes, and comparing the individual modes between LIA and DNS. Section 6.3 studies the R_{uT} variation when the upstream turbulence has finite entropy and acoustic fluctuations.

6.2 Post-shock R_{uT} for purely vortical upstream turbulence

The post-shock turbulent heat flux can be computed from the downstream fluctuations given in (3.47).

$$\overline{u_2'T_2'} = \frac{1}{2}\left[\,\overline{u_2'T_2'^*} + \overline{T_2'u_2'^*}\,\right]. \tag{6.2}$$

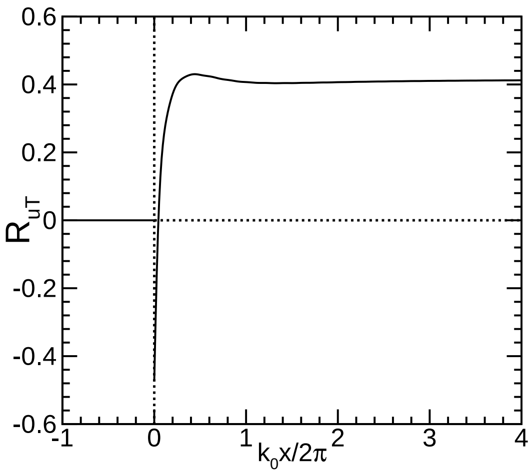

(a)

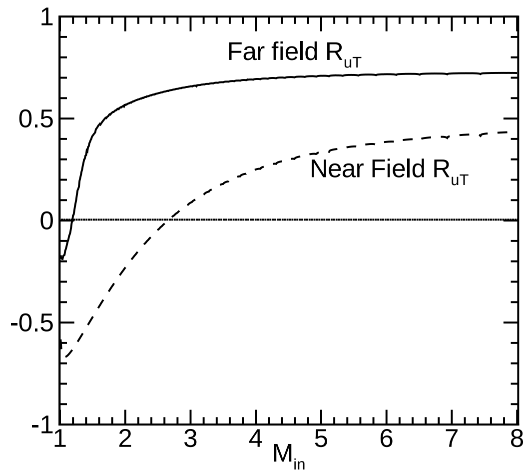

(b)

FIGURE 6.1: LIA prediction of R_{uT} for a purely vortical isotropic turbulence interacting with a normal shock: (a) streamwise variation for M_{in} = 1.5, and (b) near-field and far-field values for varying upstream Mach number.

Similar expressions for $\overline{u'^2}$ and $\overline{T'^2}$ can be written, and the value of R_{uT} can thus be found using (6.1). Note that the difference between Reynolds- and Favre-averaging is negligible in the linear framework.

We start by studying the post-shock R_{uT} correlation coefficient generated by the special case of purely vortical incoming disturbances. Therefore, in this section only, the fluctuations in pressure, density and temperature are assumed to be zero upstream of the shock.

The streamwise variation of R_{uT} obtained from LIA is shown in figure 6.1(a) for a sample case. The shock is located at $x = 0$, and R_{uT} is zero upstream of the shock due to the absence of temperature fluctuations in the incoming flow. Just downstream of the shock, the correlation coefficient attains a negative value, and rapidly rises to a positive peak followed by a constant far-field value. The change in sign is similar to that observed by for the turbulent energy flux (see chapter 4), and can be attributed to the decay behind a shock wave.

The decay of the acoustic energy leading to a rapid rise in the turbulent statistics, is an important aspect of shock-turbulence interaction. While this decay leads to a non-monotonic increase in TKE behind the shock, it exponentially decreases the value of thermodynamic fluctuations such as pressure, density and temperature [10]. The acoustic wave generated at the shock will

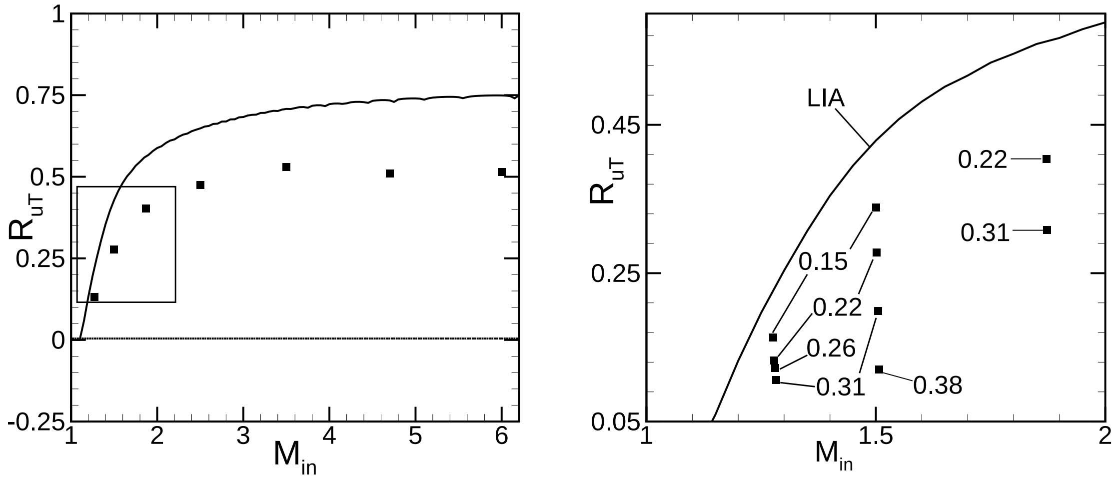

(a) (b)

FIGURE 6.2: Comparison of the peak post-shock R_{uT} between LIA (line; purely vortical incoming disturbances) and DNS (symbol) for varying upstream Mach numbers. The DNS cases in (a) correspond to $M_{t,\text{in}} = 0.22$ and $Re_{\lambda,\text{in}} = 40$. Figure (b) shows the effect of $M_{t,\text{in}}$ for a subset of M_{in}.

propagate or decay exponentially depending on the upstream incidence angle of each elementary wave [17].

Figure 6.1(b) shows the near- and far-field values of R_{uT} for varying upstream Mach numbers. For any given Mach number, the far-field value is higher than the near-field value. For upstream Mach numbers $M_{\text{in}} < 2.6$, the near-field R_{uT} values are negative and steadily attain positive values for higher Mach numbers, saturating at about 0.4. The far-field R_{uT} is positive for most Mach numbers and saturates early to a value of about 0.7.

6.2.1 Comparison between LIA and DNS

Figure 6.2(a) shows that the DNS post-shock peak R_{uT} follows the same trend as in LIA. Starting from low values, it increases with Mach number to reach an asymptotic level in the hypersonic limit. The linear theory predictions are higher than the DNS data, with a maximum difference of about 30% at high Mach numbers. The difference is highly dependent on the turbulent Mach number $M_{t,\text{in}}$ (or, analogously, on the turbulence intensity $\sim M_{t,\text{in}}/M_{\text{in}}$), as is clearly seen in figure 6.2(b). The fact that R_{uT} in DNS seem to converge towards the LIA predictions is analogous to the situation in Ryu and Livescu [57], although the present results

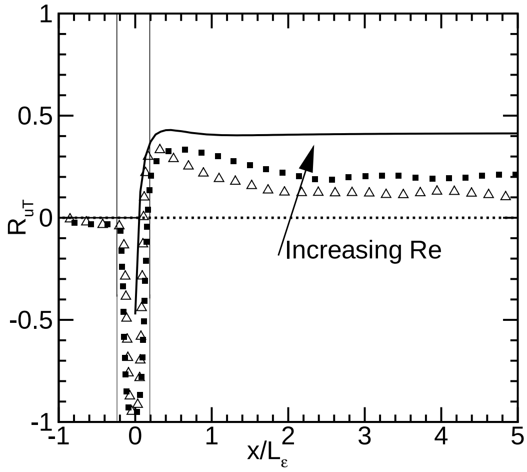

FIGURE 6.3: Streamwise comparison of R_{uT} between LIA (line; purely vortical incoming disturbances) and DNS (symbols) at $M_{\rm in} = 1.50$. The DNS cases have $M_{t,\rm in} = 0.15$ and $Re_{\lambda,\rm in}$ of 40 (triangle) and 75 (square). The vertical lines show the region over which the shock oscillates.

do not actually reach the LIA result due to the high turbulence intensities. It is also consistent with the observations about the post-shock viscous decay in Larsson et al. [20], specifically that viscous decay appears more rapidly for higher $M_{t,\rm in}$ when plotted versus a shock-normal coordinate that is scaled by a large eddy size. In other words, the systematic deviations at higher $M_{t,\rm in}$ in the figure may be due to larger relative viscous effects.

To assess the importance of the Reynolds number, the streamwise profiles of R_{uT} at fixed $M_{\rm in}$ and $M_{t,\rm in}$ but different Reynolds numbers are shown in figure 6.3. The DNS results clearly approach the LIA prediction at the higher Reynolds number, and the far-field value of R_{uT} is clearly affected by the Reynolds number in DNS. In contrast, the post-shock peak is barely different between the two cases; this could suggest that there is little Re-effect on the peak value, but could also be due to the rather different energy spectra in the two DNS cases. Either way, we conclude that LIA predicts the post-shock peak of R_{uT} rather well for purely vortical incoming disturbances.

6.2.2 Modal analysis

To analyze the post-shock R_{uT} results more deeply, we study the individual contributions to the correlation from the different Kovasznay modes. In the LIA formulation, the post-shock velocity fluctuations have contributions from the acoustic and vorticity modes, while the post-shock temperature and density fluctuations have contribution from the acoustic and entropy modes. The pressure fluctuations are purely acoustic.

The velocity-temperature correlation coefficient has contributions from all three modes. The post-shock heat flux can be written in terms of its components using (6.2) and (3.47) as

$$\overline{u_2'T_2'} = \left(\overline{u_2'T_2'}\right)_{aa} + \left(\overline{u_2'T_2'}\right)_{ae} + \left(\overline{u_2'T_2'}\right)_{va} + \left(\overline{u_2'T_2'}\right)_{ve}, \tag{6.3}$$

where the subscripts aa, ae, va and ve correspond to acoustic-acoustic, acoustic-entropy, vortical-acoustic and vortical-entropy components, respectively. The individual contributions are

$$\left(\overline{u_2'T_2'}\right)_{aa} = \frac{1}{2}\frac{\gamma-1}{\gamma}(\widetilde{F}\widetilde{K}^* + \widetilde{K}\widetilde{F}^*)\exp[i(\widetilde{k}-\widetilde{k}^*)x], \tag{6.4a}$$

$$\left(\overline{u_2'T_2'}\right)_{ae} = -\frac{1}{2}\left[\widetilde{F}\widetilde{Q}^*\exp[i(\widetilde{k}-kr\cos\psi)x] + \widetilde{Q}\widetilde{F}^*\exp[i(kr\cos\psi-\widetilde{k}^*)x]\right], \tag{6.4b}$$

$$\left(\overline{u_2'T_2'}\right)_{va} = \frac{1}{2}\frac{\gamma-1}{\gamma}\left[\widetilde{K}\widetilde{G}^*\exp[i(\widetilde{k}-kr\cos\psi)x] + \widetilde{G}\widetilde{K}^*\exp[i(kr\cos\psi-\widetilde{k}^*)x]\right], \tag{6.4c}$$

$$\left(\overline{u_2'T_2'}\right)_{ve} = -\frac{1}{2}\left[\widetilde{G}\widetilde{Q}^* + \widetilde{Q}\widetilde{G}^*\right]. \tag{6.4d}$$

Similarly, the post-shock values of $\overline{u'^2}$ and $\overline{T'^2}$ can be written in terms of their Kovasznay mode components as

$$\overline{u_2'u_2'} = \left(\overline{u_2'u_2'}\right)_{aa} + \left(\overline{u_2'u_2'}\right)_{vv} + 2\left(\overline{u_2'u_2'}\right)_{va} \tag{6.5}$$

and

$$\overline{T_2'T_2'} = \left(\overline{T_2'T_2'}\right)_{aa} + \left(\overline{T_2'T_2'}\right)_{ee} + 2\left(\overline{T_2'T_2'}\right)_{ae}, \tag{6.6}$$

where the subscripts vv and ee correspond to vortical-vortical and entropy-entropy components. Similarly to (6.4), the expressions for each of these modal components can be derived from (3.47).

Figure 6.4 shows the modal contributions to $\overline{u'T'}$, $\overline{u'^2}$ and $\overline{T'^2}$ for an upstream Mach number $M_{\text{in}} = 1.5$ as predicted by LIA. For each of the correlations, the components associated with the acoustic mode have significant contribution in the region close to the shock. This is most prominent for $\overline{T'^2}$, which takes large values immediately behind the shock and decays rapidly to low levels in the far-field. The temperature fluctuations thus clearly follow the acoustic

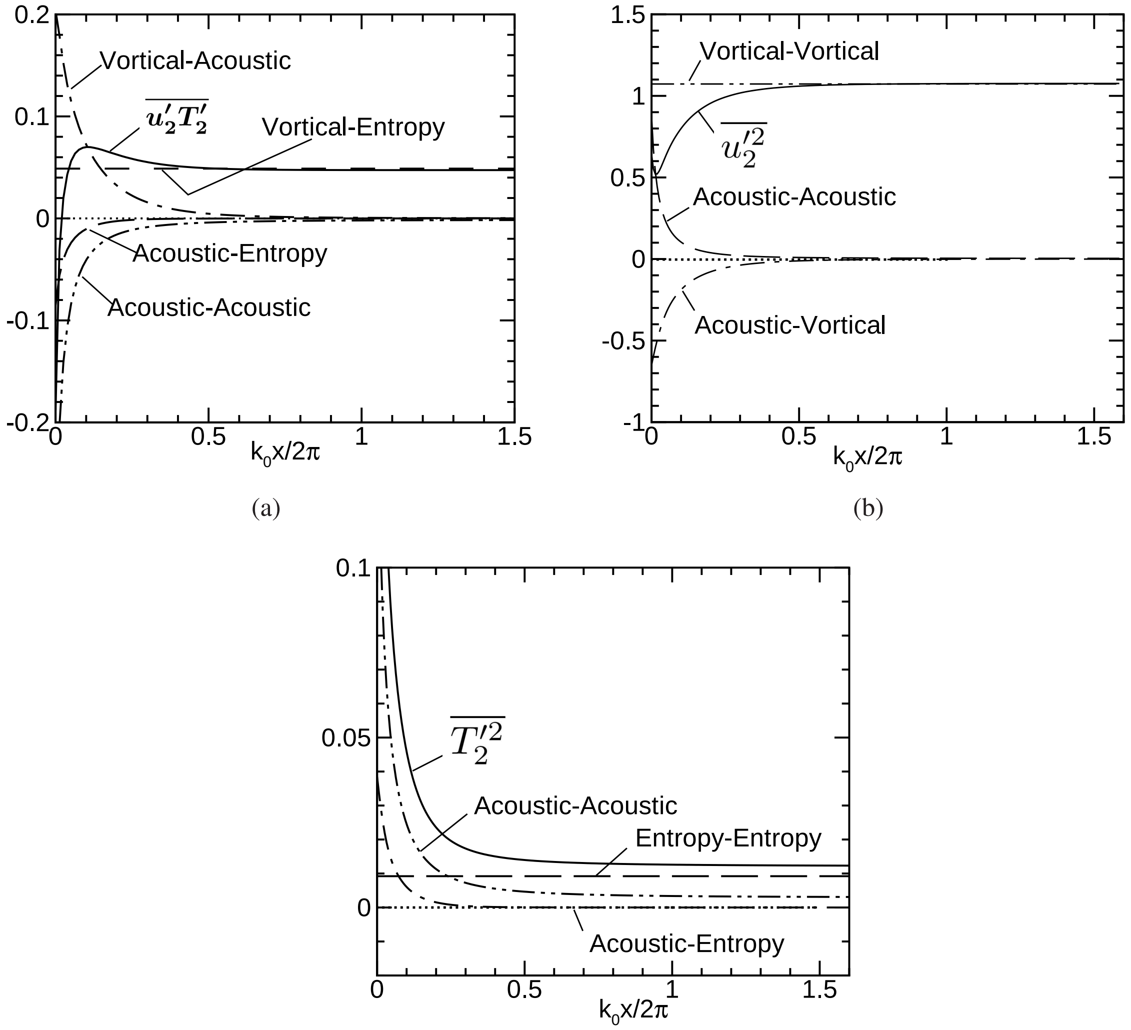

FIGURE 6.4: Kovasznay mode decomposition of (a) $\overline{u'T'}$, (b) $\overline{u'^2}$ and (c) $\overline{T'^2}$ plotted along the streamwise direction for $M_{\text{in}} = 1.50$. The upstream turbulence is purely vortical. The velocity fluctuations are normalized by the upstream mean velocity, and the temperature fluctuations are normalized by the downstream mean temperature. All correlations are further normalized by the upstream TKE.

components in figure 6.4(c). For the streamwise Reynolds stress, the acoustic and vorticity contributions are negatively correlated. A decay of the acoustic mode therefore results in a rise in $\overline{u'^2}$, as shown in figure 6.4(b). A similar trend is observed for $\overline{u'T'}$, where competing effects between the acoustic mode correlations results in a local peak in the turbulent heat flux correlation.

Figure 6.5 quantifies the percentage contribution of the Kovasznay modes to the near-field R_{uT} at varying upstream Mach numbers. At low Mach numbers, the acoustic-acoustic component

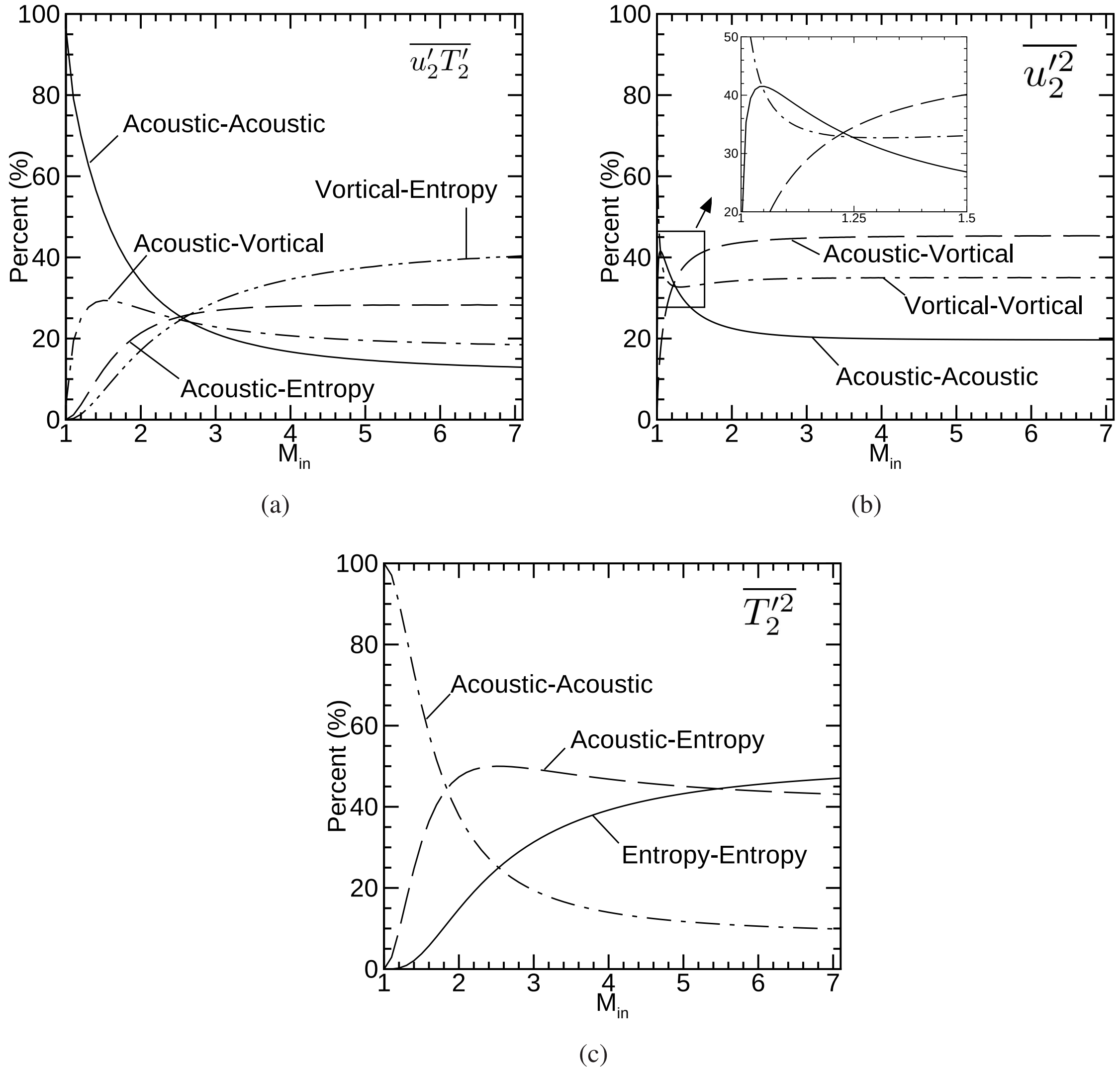

FIGURE 6.5: Percentage contribution of the Kovasznay components to the near-field ($x = 0$) values of (a) $\overline{u'T'}$, (b) $\overline{u'^2}$ and (c) $\overline{T'^2}$, as predicted by LIA for purely vortical incoming disturbances.

has a large contribution to $\overline{u'T'}$ and $\overline{T'^2}$. By comparison, the vortical-entropy component of $\overline{u'T'}$ shows a steady buildup from zero at $M_{\rm in} = 1$ to being the largest contributor beyond Mach 3. The entropy-entropy component of $\overline{T'^2}$ exhibits a similar variation for higher Mach numbers ($M_{\rm in} > 5.5$).

The modal decomposition of the velocity variance shows a slightly different trend. The vortical-vortical component of $\overline{u'^2}$ is the largest contributor at low Mach numbers, being the only contributor at $M_{\rm in} = 1$. This is because the upstream turbulence is purely vortical and remains unchanged across a very weak shock. The contribution of the vortical-vortical component decreases with Mach number, but remains one of the main contributors to $\overline{u'^2}$ at high Mach numbers. The acoustic-vortical part has a large contribution at the shock wave for $M_{\text{in}} > 1.5$, and represents the correlation between the dilatational and solenoidal components of the streamwise velocity fluctuations. The acoustic-acoustic part of $\overline{u'^2}$ is comparatively lower for high Mach numbers, as observed for the $\overline{u'T'}$ and $\overline{T'^2}$ correlations.

In summary, it is clear that R_{uT} has significant contributions from the acoustic mode at low Mach numbers. By comparison, the vorticity and entropy modes are the dominant contributors to R_{uT} for strong shock waves. Note that the results presented in figure 6.5 corresponds to the $x = 0$ location, immediately behind the shock. The energy in the acoustic mode decays to low values farther away from the shock, and thus the far-field values of $\overline{u'T'}$, $\overline{u'^2}$, $\overline{T'^2}$ and R_{uT} are primarily composed of the vortical and entropy components, at all Mach numbers.

6.2.3 Comparison of individual modes

For a given upstream turbulence that is purely vortical, we now know the dominant downstream modes that contribute to R_{uT}, both a function of Mach number and distance from the shock wave. We compare the individual downstream modes between LIA and DNS to explain the similarities and differences between the LIA and DNS R_{uT} values presented in section 6.2.1.

6.2.3.1 The vorticity mode

For incident isotropic disturbances, the upstream enstrophy is given by [19]

$$\frac{\left(\overline{\omega_i'\omega_i'}\right)_1}{U_1^2} = 3\int_{\psi=0}^{\pi/2}(2-\sin^2\psi)\sin\psi\,\mathrm{d}\psi\int_{k=0}^{\infty}\frac{k^2E(k)}{2}\mathrm{d}k, \tag{6.7}$$

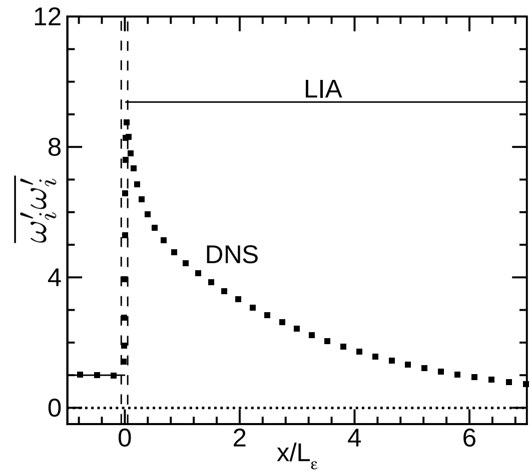

FIGURE 6.6: Streamwise evolution of the enstrophy $\overline{\omega_i'\omega_i'}$ as predicted by LIA (line; purely vortical incoming disturbances) and DNS (symbols) for the case of $M_{\text{in}} = 3.5$. The DNS data corresponds to $Re_{\lambda,\text{in}} = 40$ and $M_{t,\text{in}} = 0.15$, and the two vertical lines show the region of shock oscillation in the simulation. The correlations are normalized by their respective values just upstream of the shock.

where ω' is the fluctuating vorticity, and $E(k)$ is given by (4.12). The shock-normal vorticity variance remains unaffected across the shock, but the shock-transverse components get amplified. The post-shock value of the enstrophy can be computed using

$$\begin{aligned}\frac{\left(\overline{\omega_i'\omega_i'}\right)_2}{U_1^2} =&\frac{1}{3}\frac{\left(\overline{\omega_i'\omega_i'}\right)_1}{U_1^2} + 2\int_{\psi=0}^{\pi/2}\bigg(r^2\,\cos^2\psi\left|\widetilde{I}\right|^2 + \sin^2\psi\,\left|\widetilde{G}\right|^2 - \\ &2r\,\cos\psi\,\sin\psi(\widetilde{I}_r\widetilde{G}_r + \widetilde{I}_i\widetilde{G}_i) + r^2\,\cos^2\psi\bigg)\sin\psi\,\mathrm{d}\psi \times \int_{k=0}^{\infty}\frac{k^2E(k)}{2}\mathrm{d}k,\end{aligned} \tag{6.8}$$

where $\widetilde{G}$ and $\widetilde{I}$ represent the complex coefficients in (3.47), and subscripts r and i correspond to their real and imaginary parts.

A sample result is shown in figure 6.6, where the post-shock enstrophy is constant as per the linear inviscid theory. The DNS data, on the contrary, shows a rapid viscous decay behind the shock. The near-field values (extrapolated to the mean shock location in DNS [5, 56]) are compared in figure 6.7, showing an excellent match between LIA and DNS. Similar results were presented by Sinha [7]; an exception is the Mach 3.5 case at $Re_{\lambda,\text{in}} = 75$, which may require further grid refinement in the simulation. Thus the change in enstrophy across the shock is governed by a linear inviscid mechanism, while the downstream evolution is clearly strongly affected by some combination of nonlinear (e.g., vortex stretching or return-to-isotropy of the

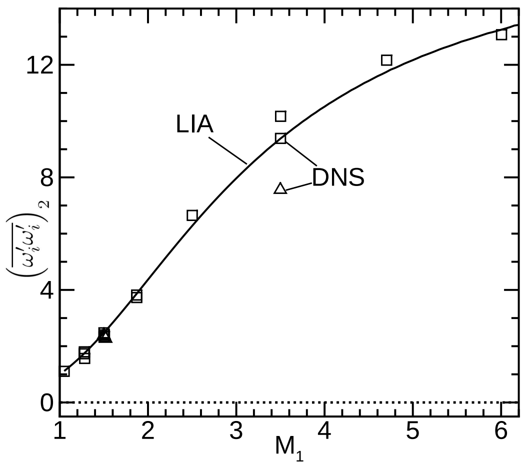

FIGURE 6.7: Post-shock enstrophy in the near-field (at $x = 0$) by LIA (line; purely vortical incoming disturbances) and DNS (symbols), normalized by the upstream value. The DNS cases are grouped into $Re_{\lambda,\text{in}} = 40$ (square) and $Re_{\lambda,\text{in}} = 75$ (triangle).

vorticity vector) and viscous effects. At high Mach numbers, the post-shock peak R_{uT} observed in the region $0 < x/L_\epsilon < 1$ has large contribution from the vortical mode (see figure 6.5). The discrepancies between DNS and LIA due to the missing nonlinear and viscous effects could then lead to potentially significant differences in the predicted peak R_{uT}, as well.

6.2.3.2 The entropy mode

The linearized expression for the normalized entropy fluctuation is

$$\frac{s'}{c_p} = \frac{p'}{\gamma \overline{p}} - \frac{\rho'}{\overline{\rho}}, \tag{6.9}$$

where c_p is the specific heat at constant pressure. In LIA, an expression for the downstream entropy variance for incoming isotropic turbulence is

$$\overline{s_2'^2} = 4\pi \int_{k=0}^{\infty} \int_{\psi=0}^{\pi/2} \left(\overline{s_2'^2}\right)_{2D} k^2 \sin\psi \, \mathrm{d}\psi \, \mathrm{d}k, \tag{6.10}$$

where $\left(\overline{s_2'^2}\right)_{2D} = \overline{s_2' s_2'^*}$ represents the entropy variance obtained for a two-dimensional interaction, which can be computed using the p_2' and ρ_2' expressions given in (3.47).

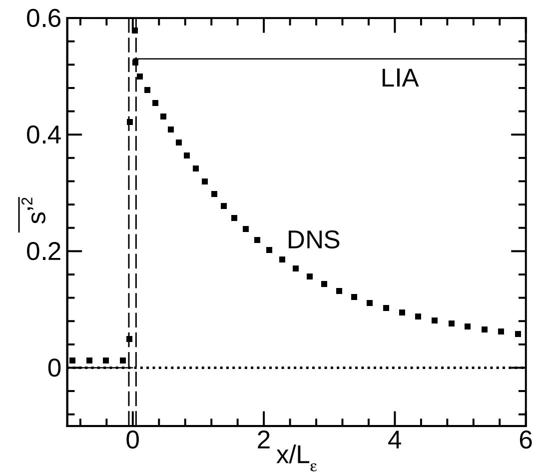

FIGURE 6.8: Streamwise variation of the entropy variance $\overline{s'^2}$ for the case of $M_{\text{in}} = 3.5$ as predicted by LIA (line; purely vortical incoming disturbances) and DNS (symbols), where DNS has $Re_{\lambda,\text{in}} = 40$ and $M_{t,\text{in}} = 0.15$. The entropy fluctuations are normalized by c_p and the velocity fluctuations are normalized by the upstream mean velocity. The correlation is further normalized by the upstream TKE.

The DNS and LIA results for the entropy variance in figure 6.8 are qualitatively similar to the enstrophy data presented previously. The rapid viscous decay in DNS is not captured by the LIA predictions, but there is a close match between the LIA near-field value and the DNS data extrapolated to the shock wave. This is true for Mach numbers up to 3.5 (see figure 6.9), beyond which the DNS entropy variance is higher than the theoretical prediction. A possible reason is that the incoming turbulence in DNS is not purely vortical, but has finite thermodynamic fluctuations [56]. These fluctuations could affect the downstream correlations especially at higher Mach numbers [19, 53].

The data suggests that the generation of the entropy mode across the shock is governed by linear mechanisms, while the downstream evolution is significantly affected by viscous and nonlinear mechanisms. This is similar to the vorticity mode, and can directly lead to the LIA-DNS mismatch in the peak R_{uT} at higher Mach numbers, where there is a significant contribution from the vorticity-entropy components.

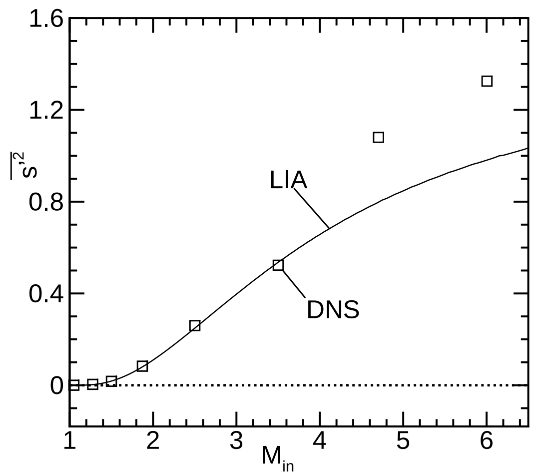

FIGURE 6.9: Amplification of $\overline{s'^2}$ across the shock for varying upstream Mach number as predicted by LIA (purely vortical incoming disturbances) and DNS (symbols). The DNS cases correspond to the lowest $M_{t,\text{in}}$ value for a given upstream Mach number. Normalization as described in figure 6.8.

6.2.3.3 The acoustic mode

As modelled in LIA, the pressure fluctuations have contributions solely from the acoustic mode. We compare the pressure-variance between LIA and DNS to comment on the acoustic mode behaviour. The pressure variance for three-dimensional incoming turbulence can be written as [19]

$$\overline{p_2'^2} = 4\pi \int_{k=0}^{\infty} \int_{\psi=0}^{\pi/2} \left(\overline{p_2'^2}\right)_{2D} k^2 \sin\psi \, \mathrm{d}\psi \, \mathrm{d}k, \tag{6.11}$$

where $\left(\overline{p_2'^2}\right)_{2D} = \overline{p_2' p_2'^*}$ represents the pressure variance obtained for a two-dimensional interaction, and can be computed using the expression given in (3.47).

We use the linearized Euler equations to derive a transport equation for the pressure variance downstream of the shock.

$$\frac{D}{Dt}\left(\frac{\overline{p'^2}}{2}\right) = -2\gamma\overline{p}\,\overline{p'\frac{\partial u_j'}{\partial x_j}}, \tag{6.12}$$

where the left-hand side represents the material derivative and $\partial u_j'/\partial x_j$ is the fluctuating dilatation. The pressure variance thus varies along the streamwise direction in the linear limit, unlike the vorticity and entropy variances, and its rate of change is governed by the pressure-dilatation correlation.

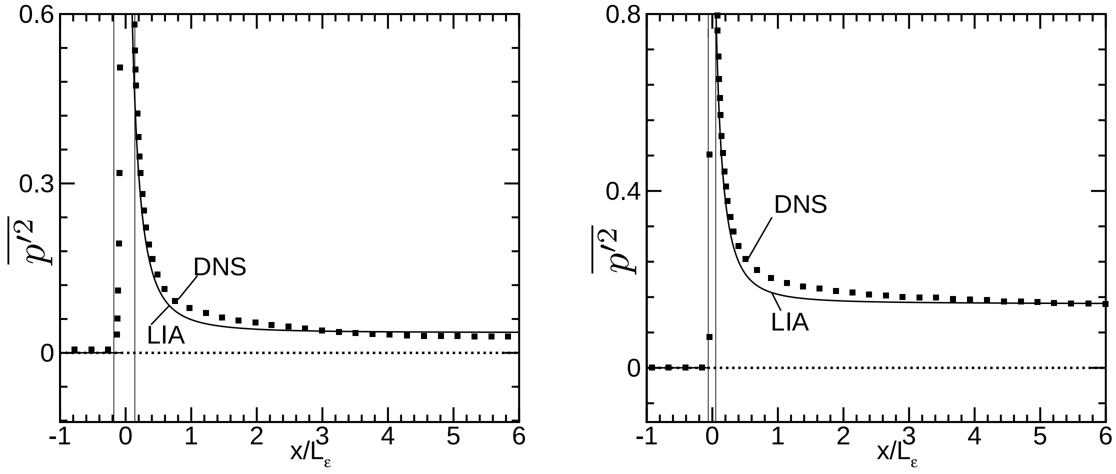

(a) (b)

FIGURE 6.10: Streamwise variation of $\overline{p'^2}$ as predicted by LIA (line; purely vortical incoming disturbances) and DNS (symbols) for the case of (a) $M_{\text{in}} = 1.50$ and (b) $M_{\text{in}} = 3.5$. The DNS data correspond to $Re_{\lambda,\text{in}} = 40$ and $M_{t,\text{in}} = 0.15$. The pressure fluctuations are normalized by the downstream mean pressure and the velocity fluctuations are normalized by the upstream mean velocity. The correlation is further normalized by the upstream TKE.

Figure 6.10 shows the streamwise evolution of the pressure variance obtained from DNS and LIA for two Mach numbers. There is an exponential decay immediately behind the shock that is well predicted by LIA. In the far-field, the linear theory gives a constant level associated with the propagating acoustic waves. The DNS results are in good agreement with this, but with a slight decay. The decay is much less pronounced compared to the vorticity- and entropy-results, which must be due to the much larger length scales for the acoustic waves. Note that there is a clear increase in the far-field value at the higher Mach number.

The DNS data shows an excellent match with the LIA far-field predictions for the entire range of Mach numbers (figure 6.11). The near-field results also compare well, within the constraints of accurately extrapolating the DNS data back to the shock center, due to the extremely rapid decay behind the shock (and the finite region of shock oscillation). This was found to be particularly difficult at low Mach numbers, which is why those cases are absent in the figure. Overall, it is found that LIA can accurately predict the generation of acoustic energy at the shock, its decay behind the shock, and the propagation of sound waves into the far-field. At low Mach numbers, the rapid variation in R_{uT} close to the shock is governed by the acoustic mode (see figure 6.5). This may explain the good match in the DNS and LIA values of peak post-shock R_{uT} at low

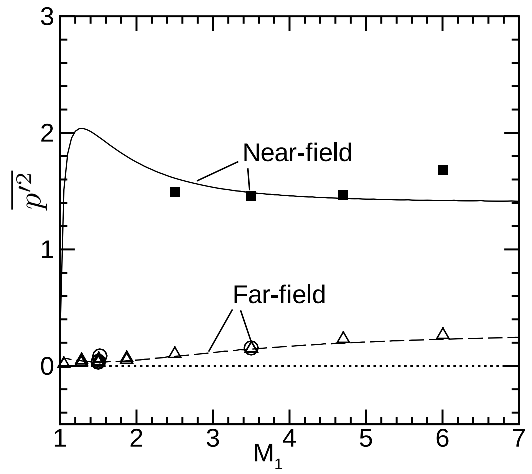

FIGURE 6.11: Near-field and far-field values of $\overline{p'^2}$ for varying upstream Mach number in LIA (lines; purely vortical incoming disturbances) and DNS (symbols). The lowest $M_{t,\text{in}}$ values at each Mach number and $Re_{\lambda,\text{in}} = 40$ are considered for the near-field comparison, whereas all DNS cases listed in table 3.1 are considered for the far-field comparison, with $Re_{\lambda,\text{in}} = 40$ (triangles) and $Re_{\lambda,\text{in}} = 75$ (circles). The DNS far-field data is averaged over $4 \leq x/L_\epsilon \leq 6$. Normalization as described in figure 6.10.

Mach numbers.

6.3 Post-shock R_{uT} for entropic and acoustic upstream turbulence

The LIA results presented so far are for purely vortical upstream turbulence. However, practical high-speed flows can have significant levels of entropy and acoustic fluctuations. In this section, we study the variation of R_{uT} across a shock when the upstream turbulence has entropy and acoustic fluctuations.

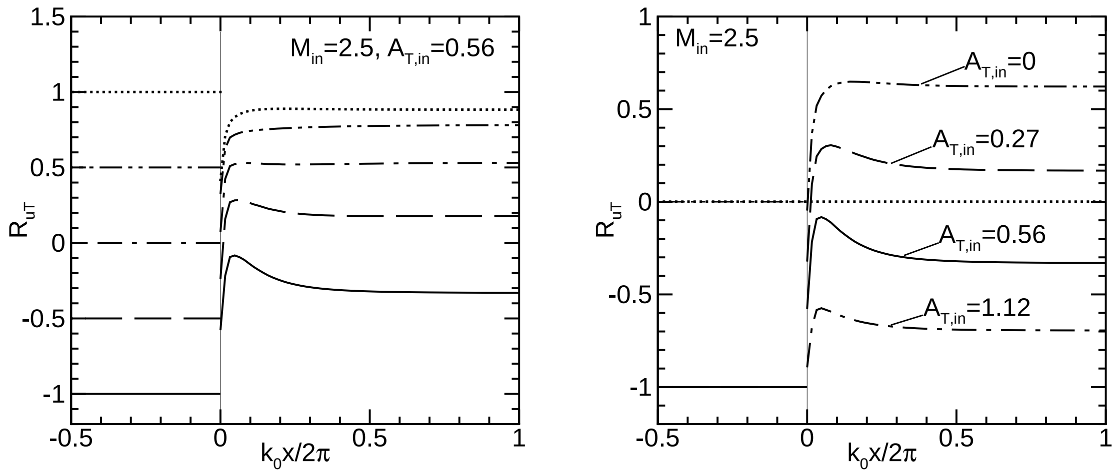

(a) (b)

FIGURE 6.12: Streamwise variation of R_{uT} when vorticity-entropy upstream turbulence interacts with a Mach 2.5 shock wave for (a) varying $R_{uT,\mathrm{in}}$ values: -1 (solid), -0.5 (dashed), 0 (dash-dotted), 0.5 (dash double-dotted) and 1 (dotted), with the amplitude ratio $A_{T,\mathrm{in}} = 0.56$, and (b) varying amplitude ratio for $R_{uT,\mathrm{in}} = -1$.

6.3.1 Combined vorticity-entropy upstream turbulence

We consider a field of vorticity and entropy waves interacting with a normal shock. The thermodynamic field is related to the velocity fluctuations by [6]

$$\frac{\rho'}{\overline{\rho}} = -\frac{T'}{\overline{T}} = A_{T,\mathrm{in}} \exp(i\phi_{T,\mathrm{in}})\frac{u'}{U},$$

and the pressure fluctuations are neglected. Here, $A_{T,\mathrm{in}}$ can be interpreted as the ratio of the normalized temperature and velocity fluctuations in the incoming flow, and $\phi_{T,\mathrm{in}}$ is the corresponding phase difference. The velocity-temperature correlation coefficient in the incoming flow is thus given by $R_{uT,\mathrm{in}} = -\cos\phi_{T,\mathrm{in}}$. Morkovin's hypothesis corresponds to taking $A_{T,\mathrm{in}} = (\gamma - 1)M_{\mathrm{in}}^2$ and $R_{uT,\mathrm{in}} = -1$. The procedure for calculating the downstream disturbance field is described in section 3.3.3.2 with details available in Mahesh et al. [19]. Note that amplitude and phase difference are applied to each elementary wave, which results in an axisymmetric incoming entropy field.

Figure 6.12(a) shows the streamwise variation of R_{uT} for the upstream values of the correlation ranging from -1 to +1. The case with $R_{uT,\mathrm{in}} = 0$ results in a positive velocity-temperature

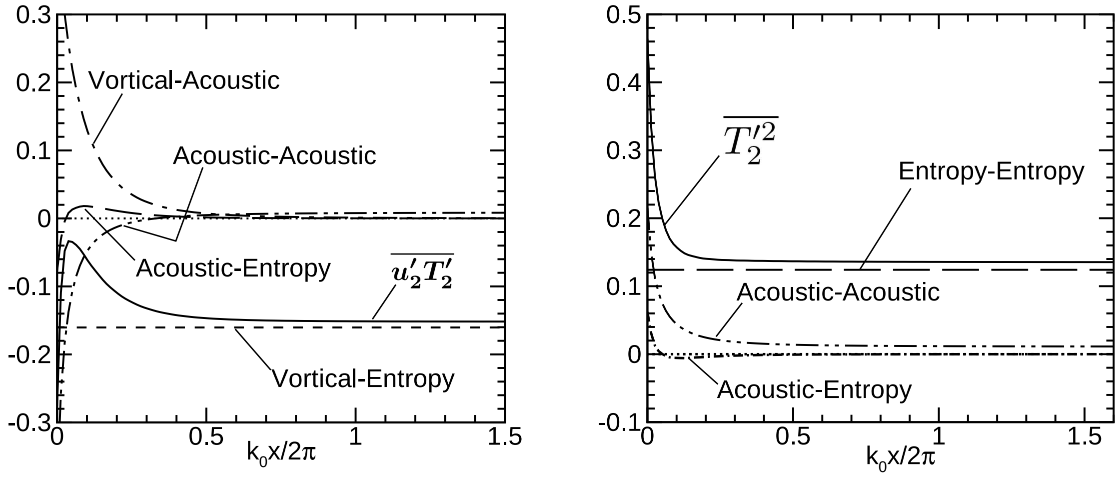

(a) (b)

FIGURE 6.13: Kovasznay mode decomposition of (a) $\overline{u'T'}$ and (b) $\overline{T'^2}$ for a vorticity-entropy disturbance field interacting with a shock wave at $M_{\text{in}} = 2.5$. The shock is located at $x = 0$. The upstream turbulence is characterised by $A_{T,\text{in}} = 0.56$ and $R_{uT,\text{in}} = -1$. Normalization as described in figure 6.4.

correlation behind the shock, and the streamwise variation is akin to that presented in figure 6.1(a). The post-shock values are relatively lower for negative $R_{uT,\text{in}}$, whereas higher values are attained for positively correlated velocity-temperature fluctuations in the incoming flow. All the cases exhibit a rapid variation of R_{uT} downstream of the shock wave similar to the purely vortical interaction (see figure 6.1(a)).

The effect of varying upstream amplitude ratio on the correlation coefficient is presented in figure 6.12(b). As $A_{T,\text{in}}$ increases, the post-shock R_{uT} decreases and takes negative values for high levels of upstream entropy fluctuations. This is true for $R_{uT,\text{in}} = -1$. An opposite trend is observed for $R_{uT,\text{in}} > 0$, and we find positively correlated velocity and temperature fluctuations behind the shock. Note that the sign of the correlation determines the direction of heat transfer due to turbulent mixing. Positive values of R_{uT} indicate heat transfer away from the shock, whereas a negative correlation coefficient implies that the turbulent heat transfer is directed towards the shock wave.

Figure 6.13 shows the Kovasznay mode decomposition of $\overline{u'T'}$ and $\overline{T'^2}$ for $M_{\text{in}} = 2.5$, $A_{T,\text{in}} = 0.56$ and $R_{uT,\text{in}} = -1$. The acoustic contributions to $\overline{u'T'}$ are qualitatively similar to those in figure 6.4(a), with large post-shock magnitudes and a decay within $k_0x/(2\pi) = 0.5$. The

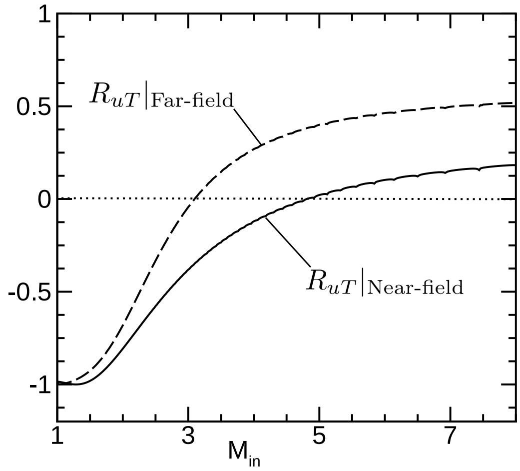

FIGURE 6.14: Near-field and far-field R_{uT} as predicted by LIA for varying upstream Mach number. The upstream turbulence has vorticity-entropy fluctuations with amplitude ratio $A_{T,\text{in}} = 0.56$ and $R_{uT,\text{in}} = -1$.

vortical-entropy component in this case is negative, unlike that in the purely vortical interaction, and it leads to a negative far-field value of $\overline{u'T'}$. The rapid post-shock variation and the local peak in $\overline{u'T'}$ is a result of the acoustic adjustment behind the shock wave. Similar observations can be made for $\overline{T'^2}$ in figure 6.13(b), where the acoustic contributions are large immediately behind the shock, and the far-field is dominated by the entropy mode. The modal decomposition of $\overline{u'^2}$ exhibits identical trends to that in figure 6.4(b), and is not shown here. Overall, the three turbulent correlations contributing to R_{uT} are dominated by the acoustic mode in the vicinity of the shock wave. The linear theory is therefore expected to well predict the near-field R_{uT} and its rapid variation behind the shock.

The LIA predictions of the near-field and the far-field R_{uT} are plotted in figure 6.14 for a range of upstream Mach numbers. As expected, the downstream R_{uT} is close to its upstream value of -1 for very weak shock waves ($M_{\text{in}} \to 1$). The correlation coefficient increases with Mach number to take positive values for strong shock waves. The far-field R_{uT} is primarily due to the vorticity-entropy contribution, while the near-field value is dominated by the acoustic mode. The difference between the far-field and the near-field R_{uT} is the net acoustic contribution to the correlation coefficient. A large difference at high Mach numbers thus indicates a higher acoustic contribution close to the shock, as compared to the low Mach number interactions.

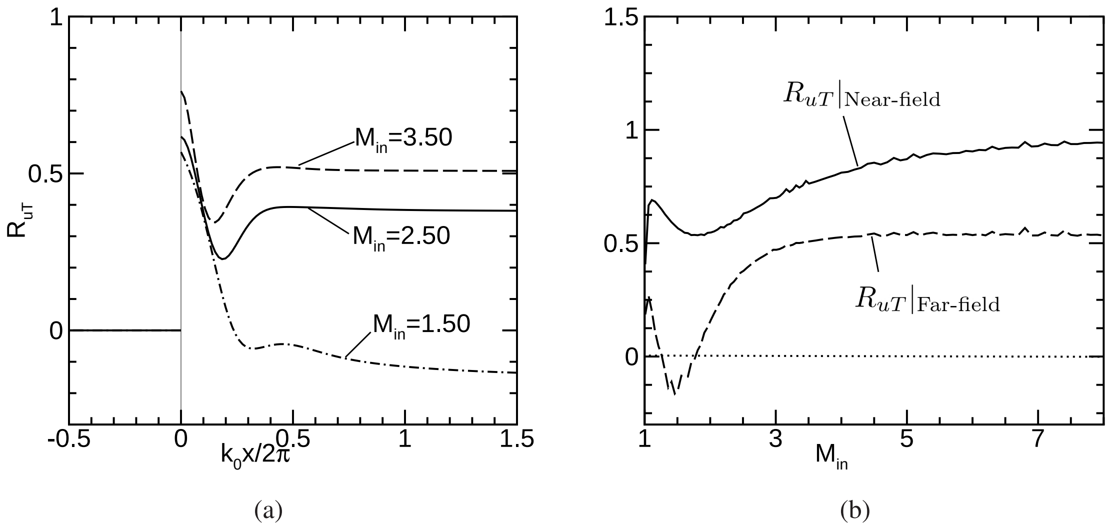

FIGURE 6.15: R_{uT} values obtained by the interaction of a purely acoustic disturbance field with a normal shock. (a) Streamwise variation of R_{uT} for three Mach numbers, with $x = 0$ representing the shock location. (b) Near-field and far-field values of R_{uT} for varying upstream Mach numbers.

6.3.2 Purely acoustic upstream field

We next study the interaction of a field of acoustic waves with a normal shock by following the procedure outlined by Moore [46]. The acoustic and the vorticity/entropy waves travel at different speed upstream of the shock and are not correlated to each other. Therefore, R_{uT} generated by the combined field of the acoustic and vorticity/entropy waves can be analyzed by first studying the independent interaction of the acoustic waves with the shock. The combined value of R_{uT} can then be calculated based on the ratio of dilatational turbulence kinetic energy associated with the acoustic mode to the total turbulence kinetic energy in the flow field. Details are provided in Mahesh et al. [45]. The LIA procedure is presented in appendix A. Three-dimensional results obtained by integrating the two-dimensional results over the von Karman spectrum given in (4.12) are presented below.

Figure 6.15(a) shows the LIA predictions for different upstream Mach numbers. It is found that the downstream variation of R_{uT} generated by the upstream acoustic field is qualitatively different from those in the purely vortical and the vorticity-entropy cases. Specifically, R_{uT} takes a large positive value immediately behind the shock and rapidly decays to lower asymptotic values in the far-field. The near-field and the far-field values also show a non-monotonic variation with Mach number, unlike earlier cases (figures 6.1(b) and 6.14). Also, the far-field R_{uT} values are lower than the near-field values for all Mach numbers indicating a net positive contribution of the decaying acoustic component behind the shock wave.

The modal decomposition of $\overline{u'T'}$, $\overline{u'^2}$ and $\overline{T'^2}$ (figure 6.16) shows interesting trends. The post-shock $\overline{T'^2}$, both near-field and far-field, are determined by the acoustic components. Same is true for $\overline{u'T'}$ and $\overline{u'^2}$. Also, the streamwise variation of $\overline{u'T'}$ and $\overline{u'^2}$ for this case is qualitatively different from those observed in figure 6.4 and 6.13. Overall, all the turbulent correlations contributing to the post-shock R_{uT} are dominated by the acoustic components, and hence are expected to be predicted well by LIA. This is true for acoustic disturbance field interacting with weak shocks. A similar decomposition carried out for stronger shock waves (data not shown) reveals that the vorticity and entropy modes can have significant contribution to post-shock R_{uT} at higher Mach numbers.

6.4 Summary

In this work, we investigate the correlation coefficient R_{uT} between the streamwise velocity and the temperature in a canonical shock-turbulence interaction. Linear interaction analysis (LIA) is employed to predict the post-shock values for vortical, acoustic and entropic upstream turbulence field. The predictions are then compared to available DNS data for which the incoming turbulence was mostly vortical. The results are summarized in figure 6.17.

For purely vortical upstream turbulence, LIA predicts a far-field R_{uT} that increases with the shock strength. The DNS data is in qualitative agreement but with lower quantitative values. This is most likely due to the known effect of the Reynolds number: e.g., note that the $Re_{\lambda,\text{in}} = 75$ results are consistently higher than those at 40. The addition of acoustic incoming waves increases the near-field R_{uT} but generally (for $M_{\text{in}} \gtrsim 1.2$) decreases the far-field R_{uT}. The addition of incoming entropy waves can increase or decrease the R_{uT} values depending on their correlation with the incoming vorticity. For the important special case of $R_{uT,\text{in}} = -1$ (which corresponds to each elementary wave satisfying Morkovin's hypothesis), the addition of incoming entropy waves leads to decreased post-shock R_{uT} values.

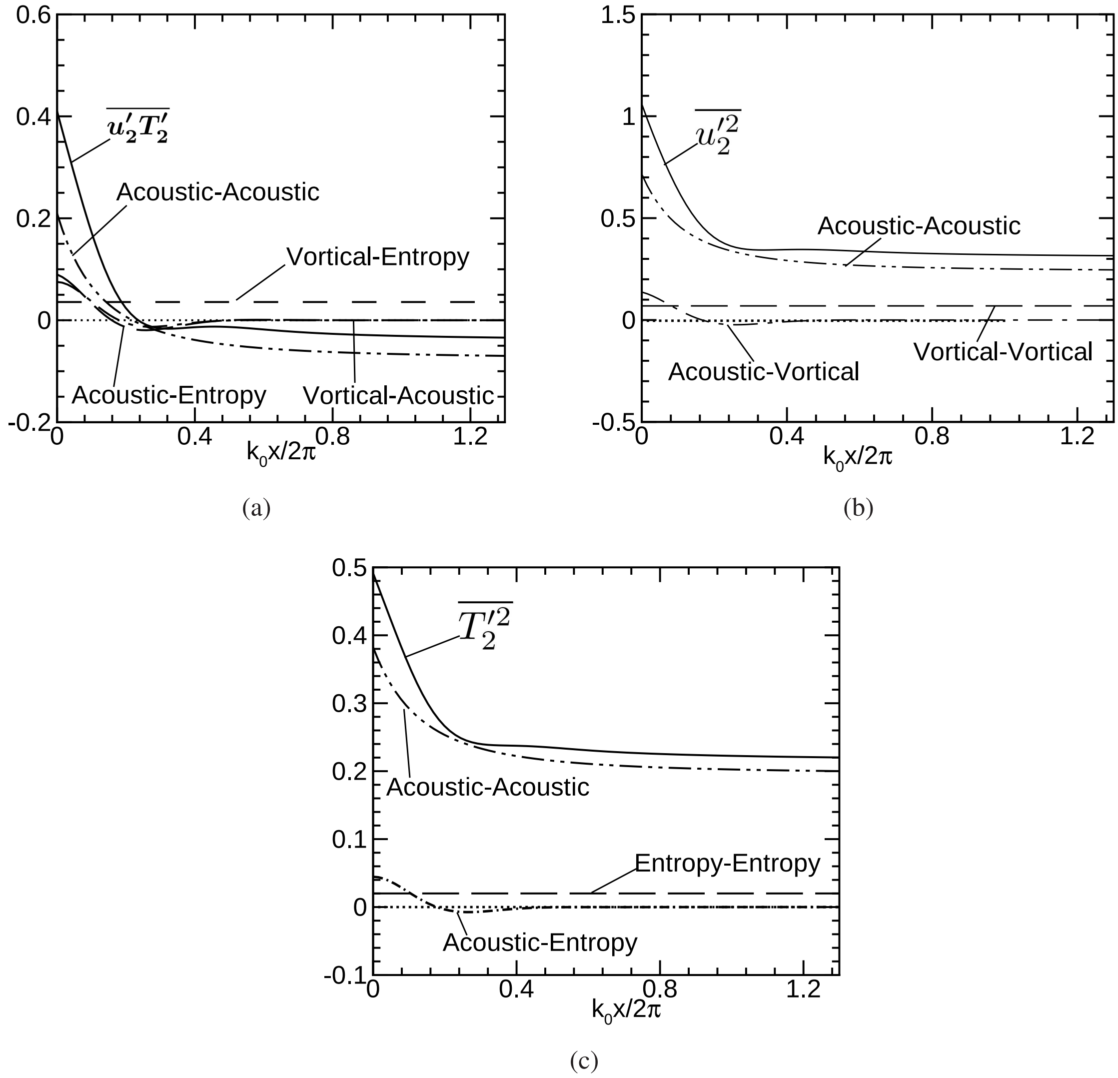

FIGURE 6.16: Kovasznay mode decomposition of (a) $\overline{u'T'}$, (b) $\overline{u'^2}$ and (c) $\overline{T'^2}$ for a purely acoustic disturbance field interacting with a normal shock. The upstream Mach number is $M_{\text{in}} = 1.50$, and the shock is located at $x = 0$. Normalization as described in figure 6.4.

The downstream R_{uT} obtained for purely vortical upstream turbulence is decomposed in terms of the Kovasznay modes of vorticity, entropy and acoustics. The vorticity-entropy downstream mode has a large contribution to the velocity-temperature correlation generated by strong shock waves. These modes are strongly influenced by viscous and non-linear effects, which explains the mismatch between LIA and DNS at high Mach numbers. At low Mach numbers, the acoustic downstream mode dominates the disturbance field behind the shock, and the peak R_{uT} value is determined by the acoustic decay in this region. There is a close match between the LIA prediction and the DNS data in terms of the generation and downstream evolution of the acoustic

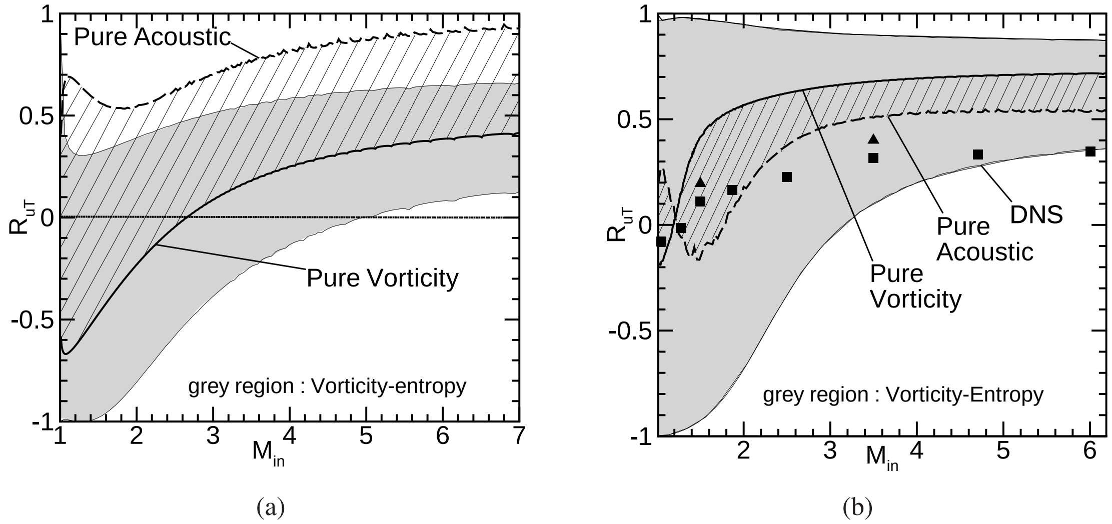

FIGURE 6.17: Summary of LIA predictions for the R_{uT} correlation coefficient in the (a) near-field at $x = 0$ and (b) far-field at $x \to \infty$. The grey region shows the bounds (for different phase angles) for combined vorticity-entropy incoming disturbances for an amplitude ratio of $A_{T,\text{in}} = 0.56$. The hatched region corresponds to different amplitude ratios of incoming vorticity and acoustic disturbances having the same spectrum. The DNS results in the far-field (averaged over $2 < x/L_\epsilon < 6$) are for the lowest $M_{t,\text{in}}$ at each M_{in}, at $Re_{\lambda,\text{in}}$ of 40 (squares) and 75 (triangles, always above the low-Re result). Note that the DNS results are known to be low due to the low Reynolds number, as evidenced in Fig. 6.3.

mode, and thus the peak positive R_{uT} generated by the vortical disturbance field interacting with relatively weak shocks is therefore well predicted by LIA. The acoustic mode is also found to be dominant for weak shock interactions of upstream turbulence with entropy and acoustic disturbances, and thus LIA is expected to provide reasonably accurate predictions of R_{uT} in such cases. Well-validated LIA predictions, along with DNS data, can thus be effectively used to propose new models for the turbulent heat flux in shock-dominated flows.

Chapter 7

Conclusion and Future Work

We investigate the turbulent energy flux correlation generated by homogeneous isotropic turbulence passing through a normal shock. We use linear interaction analysis (LIA) and direct numerical simulation (DNS) data for the study, and consider the incoming turbulence to be purely vortical. We first carry out a single wave analysis, which lies at the heart of the linear theory. A single incoming vortical wave generates all three Kovasznay modes of vorticity, entropy and acoustic disturbances. The resulting turbulent energy flux correlation is found to be a strong function of the wave incidence angle with respect to the shock. We notice that waves with higher incidence angles contribute significantly to the three-dimensional energy flux correlation. These waves have a large acoustic component that decays rapidly behind the shock. We also observe that small shock-upstream entropy fluctuations could significantly affect the downstream turbulent energy flux.

Both LIA and DNS predict a rapid non-monotonic variation, with a peak positive value of the correlation behind the shock. A budget of the transport equation for the energy flux highlights two acoustic mechanisms - pressure energy and pressure dilatation - that are dominant in the near-field. We also analyze the contribution of individual Kovasznay modes of vorticity, entropy and acoustic disturbances to the turbulent heat flux correlation. At low Mach numbers, the acoustic mode dominates the disturbance field behind the shock, and the peak correlation value is determined by the acoustic decay in this region. We find that the linear theory can accurately predict the acoustic wave generation across the shock and its decay in the downstream flow. The near-field turbulent energy flux is therefore reliably predicted by linear interaction analysis, especially for low Mach numbers. At higher Mach numbers, the post-shock energy flux correlation has significant contribution from the vorticity and entropy modes. These modes however are significantly affected by viscous and non-linear mechanisms, absent in the LIA formulation. Therefore we observe a substantial mismatch in the LIA and DNS peak energy flux values at high Mach numbers.

The acoustic decay behind the shock, along with other linear theory results, are used to propose a model for the turbulent energy flux. The differential equation based model, in conjunction with previously developed $k-\epsilon$ model, is found to match the DNS data for a range of upstream Mach numbers. An alternate algebraic model is also proposed which can predict the peak energy flux accurately.

Contributions

Overall, the thesis discusses in detail, how the correlation between velocity and temperature is altered by a shock wave in canonical shock-turbulence interaction. Some of the specific contributions of this thesis are :

- Using LIA and DNS data to carry out a detailed investigation of turbulent energy flux across the shock, and indentifying the important parameters which affect this correlation.
- Establishing LIA as a reliable tool to study the correlation between velocity and temperature fluctuations in canonical shock-turbulence interaction.
- Identifying dominant Kovaznay mode contributions to the velocity-temperature correlation for varying upstream Mach numbers, and analyzing the influence of the dominant mode on the accuracy of LIA prediction.
- Developing new algebraic and differential equation-based models to capture the essential physics of turbulent energy flux evolution across the shock.

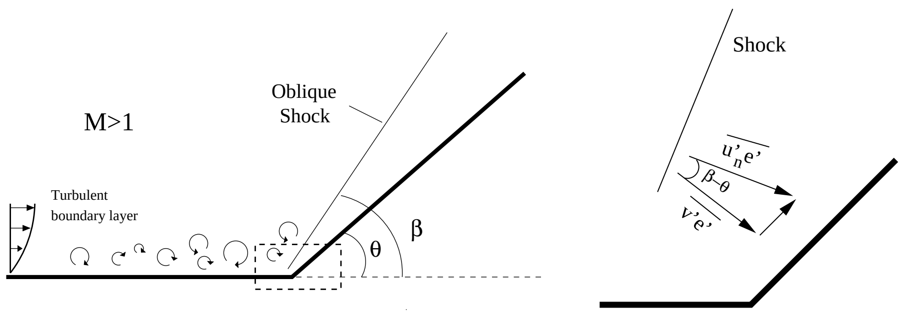

FIGURE 7.1: Schematic of a turbulent boundary layer interacting with an oblique shock wave.

Implications for Shock/boundary-layer interactions

In the current study of shock-turbulence interaction, it was seen that peak positive values of the shock-normal or streamwise energy flux are generated behind the shock. The implication of this study to a canonical shock/boundary-layer interaction (SBLI) is explored by considering figure 7.1, which shows a schematic of an incoming turbulent boundary layer on a flat plate encountering a compression corner. The ramp angle θ is small, such that an attached oblique shock is formed at an angle β with respect to the incoming flow. High wall pressure and convective heat transfer rates are observed at the point of interaction.

For the canonical SBLI configuration considered here, the peak turbulent energy flux normal to the oblique shock is denoted by $\overline{u'_n e'}$ as seen in figure 7.1(b). The component of the turbulent energy flux in the wall-normal direction can be written as

$$\overline{v'e'} = -\overline{u'_n e'} \cos(\beta - \theta)$$

where $\beta - \theta$ is small for a weak oblique shock wave and v' is taken as positive away from the wall. This implies that large negative values of $\overline{v'e'}$ can be generated by the shock. A negative wall-normal turbulent energy flux in the near-wall region amounts to a net energy transfer towards the wall, which would enhance the heat flux to the wall. Thus it is possible that this type of effect is partially responsible for the increased heat transfer usually observed in SBLI experiments [16, 39].

It was earlier seen that the peak positive energy flux in the shock-homogeneous turbulence interaction occurs at a distance of $0.5L_\epsilon$ from the shock wave. This translates to about $0.25-0.5\delta_0$ in a compression ramp SBLI, where δ_0 is the upstream undisturbed boundary layer thickness. Further, the above description is for an unseparated weak shock/boundary-layer interaction. In the stronger interactions with boundary-layer separation, a similar argument can be applied to the reattachment shock, leading to a high heat transfer near the reattachment point. It can also be extended to the reflected shock in an oblique shock impingement on a turbulent boundary layer.

Conventional models based on gradient hypothesis are insensitive to the peak energy flux values obtained in the acoustic adjustment region behind the shock wave. Outside the shock wave, they switch to the local temperature gradient in the downstream flow. The results reported here show that this may be grossly inadequate, as the primary effect of the shock wave on heat transfer is via the peak turbulent energy flux following the shock wave. It may therefore be important to predict this phenomena in realistic flows. Most conventional models are based on a local formulation for the turbulent heat flux vector, with no downstream influence of the shock wave. A few advanced models based on transport equations for the energy flux correlation and related quantities [11] may be able to bring in this effect.

Future work

Following are some of the ideas inspired by the current work that could be pursued.

- Presence of upstream thermodynamic fluctuations (temperature, pressure, density), and their correlation with the upstream vorticity fluctuations, could have a significant bearing on the turbulent energy flux generated across the shock. It would be interesting to study the sign and magnitude of the energy flux for flows with various types of upstream turbulence.
- One of the key characteristics of turbulent energy flux in the shock-turbulence interaction is the peak positive value of the correlation followed by an acoustic decay. These findings

in the near-shock region could be implemented into a RANS simulation of canonical shock/boundary-layer interaction. This could highlight the importance of turbulent energy flux variation across the shock on the wall heat flux.

- We carried out a detailed study of R_{uT} variation across the shock. The effect of change in R_{uT} on the variation of Pr_T, and its implication on variable Pr_T modelling can be studied.

- LIA showed accurate prediction of modes just across the shock. This efficacy of the linear theory could be extended to analyse the shock distortion, which essentially correlates the upstream and the downstream fluctuations.

- At high Mach numbers ($M_1 > 4.7$), the near-field DNS values of the entropy and acoustic variances showed a mismatch with the LIA results. There is a need to analyze the bounds in which the linearized Rankine-Hugoniot jump conditions, which govern the LIA near-field values, are valid.

- The match in the acoustic mode between DNS and LIA has several implications:

  – It would be interesting to observe the effect of upstream thermodynamic fluctuations on the post-shock acoustic mode and to analyze the efficacy of LIA in predicting the acoustic mode.

  – The post-shock temperature and density fluctuations have significant contributions from the acoustic mode; comparing the LIA and DNS values of these thermodynamic fluctuations could reveal some of their interesting characteristics.

  – We could perform an in-depth analysis to reason why the acoustic fluctuations are unaffected by the viscous and non-linear effects; studying the downstream wavenumber and the convection speed of the acoustic wave could help answer this question.

  – We could compare the LIA and DNS values of the turbulent statistics, which similar to pressure variance, have their contribution from the acoustic mode alone; for example, velocity dilatation variance.

Appendix A

Interaction of an acoustic wave with shock wave

Moore [46] considered a shock moving with a velocity V into a stationary gas having an acoustic wave; a schematic is shown in figure A.1. All three modes (acoustic, entropy and vorticity) are generated downstream of the shock, and the amplitude and phase of the downstream waves are functions of the incidence angle and shock strength. In an alternate frame of reference, this configuration is similar to the one considered in the current study, where a mean flow convecting

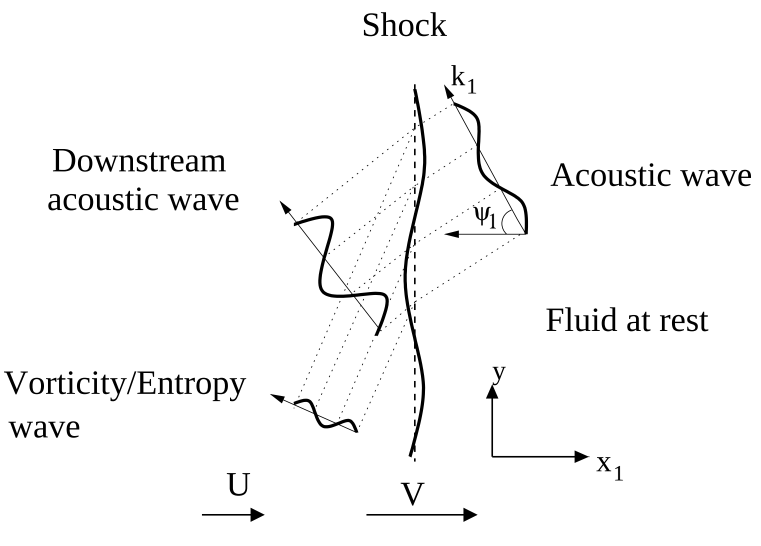

FIGURE A.1: A single acoustic wave in a stationary gas interacts with a shock wave moving with a velocity V to generate all three waves (acoustic, entropy and vorticity).

the disturbance interacts with a stationary shock wave. The development follows the work of Moore [46] and all the essential steps required to obtain the relevant results in the current report are given below.

In the frame of reference $x_1 - y$ (figure A.1) attached to the fluid at rest, the upstream acoustic waveforms can be represented as

$$\frac{u_1'}{V} = -\frac{\cos\psi}{\gamma M_1} A_p \exp[ik_1(x_1\cos\psi - y\sin\psi + a_1 t)], \tag{A.1a}$$
$$\frac{T_1'}{\overline{T}_1} = \frac{\gamma - 1}{\gamma} A_p \exp[ik_1(x_1\cos\psi - y\sin\psi + a_1 t)], \tag{A.1b}$$

where u_1' is the streamwise velocity fluctuation in the stationary gas, V represents the mean shock velocity, and T_1' is the temperature fluctuations. a_1 and $\overline{T}_1$ represent the mean speed of sound and temperature, respectively, in the gas which is stationary in the mean. ψ represents the angle of incidence of the upstream acoustic wave with respect to the shock-normal direction, and k_1 is the corresponding wavenumber. A_p is the amplitude of the acoustic wave and $M_1 = V/a_1$ is the Mach number of the shock wave.

The downstream acoustic field could either be decaying or propagating in nature depending on the angle of the incident acoustic wave. The critical angles ψ_{cl} and ψ_{cu} are obtained as the roots of the following equation [46]

$$\left(\frac{a_2}{V}\right)^2 - \left(1 - \frac{U}{V}\right)^2 = \left(\cot\psi + \frac{a_1}{V}\csc\psi\right)^2,$$

where a_2 and U are the post-shock mean speed of sound and mean velocity, respectively. For the value of upstream incidence angle in the range $0 \leq \psi < \psi_{cl}$ or $\psi_{cu} < \psi \leq \pi$, the downstream acoustic wave has a propagating nature, and for $\psi_{cl} < \psi < \psi_{cu}$, the acoustic wave decays exponentially.

The linearised Rankine-Hugoniot conditions are now given as

$$\frac{\xi_t - u_2'}{V} = B\frac{\xi_t - u_1'}{V} + \hat{B}\frac{p_1'}{P_1}, \quad \frac{v_2'}{V} = \frac{v_1'}{V} - \frac{U}{V}\xi_y,$$
$$\frac{T_2'}{\overline{T}_2} = (D - C)\frac{\xi_t - u_1'}{V} + (\hat{D} - \hat{C})\frac{p_1'}{P_1},$$

where the terms B, C and D are as defined in (3.38). The coefficients due to the acoustic fluctuations are given as follows,

$$\hat{B} = \left(\frac{\gamma-1}{\gamma+1}\right)\frac{2}{\gamma M_1^2}, \quad \hat{C} = \frac{1}{\gamma}\left(1 - \frac{2\,(\gamma-1)}{2+(\gamma-1)\,M_1^2}\right), \quad \hat{D} = \frac{2M_1^2-(\gamma-1)}{2\gamma M_1^2-(\gamma-1)}.$$

The solutions for the downstream waveforms in the propagating regime ($0 \le \psi_1 < \psi_{cl}$ or $\psi_{cu} < \psi_1 \le \pi$) are given by

$$\frac{1}{A_p}\frac{u_2'}{V} = \widetilde{F}\exp(ik_2\eta_a) + \widetilde{G}\exp(ik_1\eta_v), \tag{A.3a}$$

$$\frac{1}{A_p}\frac{T_2'}{\overline{T}_2} = \frac{\gamma-1}{\gamma}\widetilde{K}\exp(ik_2\eta_a) - \widetilde{Q}\exp(ik_1\eta_v), \tag{A.3b}$$

where the arguments of the vorticity/entropy waveform (η_v) and the acoustic waveform (η_a) are defined as

$$\eta_a = \alpha x_2 + \beta y + a_2 t,$$
$$\eta_v = \frac{\cos\psi + 1/M_1}{1-r}x_2 - y\sin\psi,$$

The above downstream expressions are written in a frame of reference that moves with a mean velocity U such that x_2 axis is stationary with respect to the mean flow downstream of the shock. k_2 is the corresponding downstream wavenumber.

The complex coefficients $\widetilde{K}$ and $\widetilde{F}$ correspond to the acoustic mode, $\widetilde{G}$ correspond to the vortical mode and $\widetilde{Q}$ represents the contribution from the entropy mode. The expressions for α, β, $\widetilde{K}$, $\widetilde{F}$, $\widetilde{G}$ and $\widetilde{Q}$ are provided below; they are functions of upstream Mach number and angle of incidence.

$$\widetilde{L} = -\frac{m}{\gamma M_1}\frac{\left[1+\frac{\gamma+1}{4}\frac{M_1}{m}\left(\frac{3-\gamma}{\gamma+1}+\frac{\gamma-1}{2}r\right)\right]\chi + \frac{\gamma+1}{4}\left[1-2\frac{\gamma-1}{\gamma+1}\frac{n}{\sigma}-\frac{n\sigma}{1-r}\right](1-r)}{1+\chi-\frac{\gamma+1}{4}r\left(1+\frac{\sigma^2}{1-r}\right)},$$

$$\widetilde{K} = D\left(\widetilde{L}+\frac{m}{\gamma M_1}\right)+\hat{D}, \quad \widetilde{Q} = C\left(\widetilde{L}+\frac{m}{\gamma M_1}\right)+\hat{C}-\frac{\widetilde{K}}{\gamma},$$

$$\widetilde{F} = -\frac{a_2}{\gamma V}\widetilde{K}\alpha, \quad \widetilde{G} = \widetilde{L}-\widetilde{F}-B\left(\widetilde{L}+\frac{m}{\gamma M_1}\right)-\hat{B},$$

where

$$
\begin{aligned}
&l = \sin\psi, \quad m = \cos\psi, \quad n = \tan\psi, \\
&r = \frac{2}{\gamma+1}\left(1 - \frac{1}{M_1^2}\right), \quad \left(\frac{a_2}{V}\right)^2 = (1-r)\left(1 + \frac{\gamma-1}{2}r\right), \quad \sigma = \frac{n\,(1-r)}{1+\frac{1}{M_1 m}}, \\
&\chi = \left[1 - \frac{r\,(\gamma+1)\,(1+\sigma^2)}{2+(\gamma-1)\,r}\right]^{1/2}, \quad \alpha = \frac{1}{1-r}\left[\frac{\lambda_2}{\lambda_1}\left(m + \frac{1}{M_1}\right) - \frac{a_2}{V}\right], \quad \beta = -l\frac{\lambda_2}{\lambda_1}, \\
&m\frac{\lambda_2}{\lambda_1} = m\frac{k_1}{k_2} = \frac{\frac{a_2}{V}\left(1+\frac{1}{M_1 m}\right)}{\left(1+\frac{1}{M_1 m}\right)^2 + n^2\,(1-r)^2}\left[1 + \sqrt{1 - r\frac{1+n^2\,(1-r)^2 \Big/ \left(1+\frac{1}{M_1 m}\right)^2}{1-\frac{\gamma-1}{\gamma+1}\,(1-r)}}\,\right].
\end{aligned}
$$

The solutions for the fluctuations in the decaying regime i.e. $\psi_{cl} < \psi < \psi_{cu}$ are given as

$$\frac{1}{A_p}\frac{u_2'}{V} = \widetilde{F}_{(1)}\Phi_{(1)} + \widetilde{F}_{(2)}\Phi_{(2)} + \left(\widetilde{G}_{(1)} + i\widetilde{G}_{(2)}\right)\exp(ik_1\eta_v), \tag{A.4a}$$

$$\frac{1}{A_p}\frac{T_2'}{\overline{T}_2} = \frac{\gamma-1}{\gamma}\left(\widetilde{K}_{(1)}\Phi_{(1)} + \widetilde{K}_{(2)}\Phi_{(2)}\right) + \left(\widetilde{Q}_{(1)} + i\widetilde{Q}_{(2)}\right)\exp(ik_1\eta_v), \tag{A.4b}$$

where η_v is as defined before and the expressions for $\Phi_{(1)}$ and $\Phi_{(2)}$ are

$$
\begin{aligned}
\Phi_{(1)} &= \exp(k_1\zeta)\,\exp(ik_1\eta_d), \\
\Phi_{(2)} &= i\exp(k_1\zeta)\,\exp(ik_1\eta_d),
\end{aligned}
$$

where the arguments ζ and η_d are given by

$$\zeta = d(x_2 - (V-U)t), \quad \eta_d = (\alpha x_2 + \beta y + cVt)$$

The coefficients $\widetilde{K}_{(\alpha)}$ and $\widetilde{F}_{(\alpha)}$ correspond to the acoustic mode, $\widetilde{G}_{(\alpha)}$ to the vorticity mode, and $\widetilde{Q}_{(\alpha)}$ represents the entropy mode. The expressions for these amplitudes along with those for c,

d, α and β are provided below.

$$\widetilde{L}_{(1)} = \frac{h_1 h_2 - \left(\frac{m}{\gamma M_1} + \frac{\hat{D}}{D}\right) h_3^2}{h_2^2 + h_3^2}, \quad \widetilde{L}_{(2)} = h_3 \frac{h_1 + \left(\frac{m}{\gamma M_1} + \frac{\hat{D}}{D}\right) h_2}{h_2^2 + h_3^2},$$
$$\widetilde{F}_{(1)} = h_4 \left(\widetilde{L}_{(1)} + \frac{m}{\gamma M_1} + \frac{\hat{D}}{D}\right) - h_5 \widetilde{L}_{(2)}, \quad \widetilde{F}_{(2)} = h_5 \left(\widetilde{L}_{(1)} + \frac{m}{\gamma M_1} + \frac{\hat{D}}{D}\right) + h_4 \widetilde{L}_{(2)},$$
$$\widetilde{K}_{(1)} = D \left(\widetilde{L}_{(1)} + \frac{m}{\gamma M_1}\right) + \hat{D}, \quad \widetilde{K}_{(2)} = D \widetilde{L}_{(2)},$$
$$\widetilde{Q}_{(1)} = C \left(\widetilde{L}_{(1)} + \frac{m}{\gamma M_1}\right) + \hat{C} - \frac{\widetilde{K}_{(1)}}{\gamma}, \quad \widetilde{Q}_{(2)} = C \widetilde{L}_{(2)} - \frac{\widetilde{K}_{(2)}}{\gamma},$$
$$\widetilde{G}_{(1)} = \widetilde{L}_{(1)} - \widetilde{F}_{(1)} - B \left(\widetilde{L}_{(1)} + \frac{m}{\gamma M_1}\right) - \hat{B}, \quad \widetilde{G}_{(2)} = \widetilde{L}_{(2)} (1 - B) - \widetilde{F}_{(2)},$$

where

$$h_1 = -\frac{1-r}{r}\frac{1}{\sigma}\left[\frac{l}{\gamma M_1} + \left(\frac{m}{\gamma M_1} B + \hat{B}\right)\frac{1}{\sigma}\right], \quad h_2 = 1 - \frac{1-r}{r}\frac{1-B}{\sigma^2},$$
$$h_3 = -\frac{4d\,(1-r)\,/\,l\sigma}{(2 + (\gamma - 1)\,r)}, \quad h_4 = \frac{4}{\gamma+1}\frac{\sigma^2}{1+\sigma^2}, \quad h_5 = \frac{2rd\sigma\,(1-r)}{l\,(1+\sigma^2)}\frac{V^2}{a_2^2},$$
$$c = \frac{m + 1/M_1}{1 - V^2\,(1-r)^2\,/a_2^2}, \quad \alpha = -\frac{V^2}{a_2^2}\,(1-r)\,c, \quad \beta = -l, \quad d = \sqrt{\frac{\alpha^2 + l^2 - V^2 c^2/a_2^2}{1 - V^2\,(1-r)^2\,/a_2^2}}.$$

with l, m, n and σ being the same as in the propagating regime.

The normalized turbulent energy flux generated downstream of the shock can be written as

$$\overline{u_2' e_2'} = \left(\frac{1}{\gamma - 1}\right)\frac{1}{V\overline{T}_2}\frac{\left[\overline{u_2' T_2'^*} + \overline{T_2' u_2'^*}\right]}{2(TKE_1/V^2)}, \tag{A.6}$$

where the velocity fluctuation is normalized by the mean shock speed V which is identical to the upstream mean flow velocity relative to the shock. The temperature fluctuation is normalized by the downstream mean temperature $\overline{T}_2$, and C_v is normalized by R. Here, * indicates complex conjugate, and TKE_1 corresponds to the turbulence kinetic energy upstream of the shock.

Mahesh et al. [45] extend the two-dimensional analysis by Moore [46] to study a field of acoustic waves interacting with a shock. In the linear inviscid framework, post-shock statistics are computed by superimposing single wave results for a specified isotropic energy spectrum upstream of the shock wave. The value of downstream $\overline{u_2' e_2'}$ for a three-dimensional isotropic spectrum of planar waves can be written as

$$(\overline{u_2'e_2'})_{3D} = 2\pi \int_0^{\pi} \int_0^{\infty} (\overline{u_2'e_2'})_{2D}\, k^2\ \sin\psi\, dk\, d\psi\,, \tag{A.7}$$

where $(\overline{u_2'e_2'})_{2D}$ is the correlation obtained for a two-dimensional planar wave in (A.7). Computations of the three-dimensional statistics requires the spectrum of pressure fluctuations ahead of the shock, which is related to the three-dimensional energy spectrum $E(k)$ as [45]

$$\frac{|\hat{p}_1|^2(\mathbf{k})}{P_1^2} = \left(\frac{\gamma M_1}{V}\right)^2 \frac{E(k)}{4\pi k^2},$$

with the expression for $E(k)$ taken as per the von Karman spectrum given in (4.12). Further details are provided in Mahesh et al. [19].

Bibliography

[1] C. J. Roy and F. G. Blottner. Review and assessment of turbulence models for hypersonic flows. *Progress in Aerospace Sciences*, 42 (7):469–530, 2001.

[2] F. Thivet, D. D. Knight, A. A. Zheltovodov, and A. I. Maksimov. Importance of limiting the turbulent stresses to predict 3D shock-wave/boundary-layer interactions. *23rd International Symposium on Shock Waves, Fort Worth, TX*, 2001.

[3] D. C. Wilcox. Formulation of the $k-\omega$ turbulence model revisited. *AIAA Journal*, 46 (11):2823–2838, 2008.

[4] F. R. Menter. Two-equation eddy-viscosity turbulence models for engineering applications. *AIAA Journal*, 32 (8):1598–1605, 1994.

[5] K. Sinha, K. Mahesh, and G. V. Candler. Modeling shock-unsteadiness in shock-turbulence interaction. *Phys. Fluids*, 15:2290–2297, 2003.

[6] V. K. Veera and K. Sinha. Modelling the effect of upstream temperature fluctuations on shock/homogeneous turbulence interaction. *Phys. Fluids*, 21:025101, 2009.

[7] K. Sinha. Evolution of enstrophy in shock/homogeneous turbulence interaction. *J. Fluid Mech.*, 707:74–110, 2012.

[8] A. A. Pasha and K. Sinha. Shock-unsteadiness model applied to hypersonic shock-wave/turbulent boundary-layer interactions. *Journal of Propulsion and Power*, 28 (1): 46–60, 2012.

[9] M. V. Morkovin. Effects of compressibility on turbulent flows. *Mecanique de la Turbulence, CNRS. edited by A. Favre, Gordon and Breach, New York,*, pages 367–380, 1962.

[10] K. Mahesh, S. K. Lele, and P. Moin. The influence of entropy fluctuations on the interaction of turbulence with a shock wave. *J. Fluid Mech.*, 334:353–379, 1997.

[11] X. Xiao, H. A. Hassan, J. R. Edwards, and R. L. Gaffney Jr. Role of turbulent Prandtl numbers on heat flux at hypersonic Mach numbers. *AIAA Journal*, 45 (4):806–813, 2007.

[12] T. P. Sommer, R. M. C. So, and H. S. Zhang. Near-wall variable-prandtl-number turbulence model for compressible flows. *AIAA Journal*, 31 (1):27–35, 1993.

[13] Kevin W. Brinckman, William H. Calhoon Jr., and Sanford M. Dash. Scalar fluctuation modeling for high-speed aeropropulsive flows. *AIAA journal*, 45(5):1065, 2007.

[14] Uriel C. Goldberg, Sampath Palaniswamy, Paul Batten, and Vinit Gupta. Variable turbulent schmidt and prandtl number modeling. *Engineering application of computational fluid mechanics*, 4:511, 2010.

[15] R. D. W. Bowersox. Extension of equilibrium turbulent heat flux models to high-speed shear flows. *J. Fluid Mech.*, 633:61–70, 2009.

[16] E. Schulein. Optical skin friction measurements in short-duration facilities. *AIAA Journal*, 44:1732–1741, 2006.

[17] H. S. Ribner. Convection of a pattern of vorticity through a shock wave. Technical Report 1164, NACA Report, 1953.

[18] H. S. Ribner. Shock-turbulence interaction and the generation of noise. Technical Report 1233, NACA Report, 1954.

[19] K. Mahesh, S. K. Lele, and P. Moin. The interaction of a shock wave with a turbulent shear flow. Technical Report 69, Thermosciences division, Department of Mechanical Engineering, Stanford University, Stanford, CA., 1996.

[20] J. Larsson, I. Bermejo-Moreno, and S. K. Lele. Reynolds- and Mach number effects in canonical shock-turbulence interaction. *J. Fluid Mech.*, 717:293–321, 2013.

[21] H. Laurent. Turbulence d'une interaction onde de choc/couche limite surune paroi plane adiabatique ou chauffee. Technical report, Th'ese de Doctorat, Universite de la Mediterranee, France., 1996.

[22] J. F. Debi‘eve. Etude d’une interaction turbulence/onde de choc. Technical report, Th‘ese de Universite d’Aix-Marseille II, 1983.

[23] J. P. Dussage. Evolution de transferts turbulents dans une detente rapide, en ecoulement supersonique. Technical report, Th‘ese de Doctorat d‘Etat, Universit é d’Aix Marseille, 1981.

[24] M. Wu and M. P. Martin. Direct numerical simulation of two shock-wave/turbulent boundary layer interactions at mach 2.9 and re_θ = 2400. *AIAA paper*, 04-2145, 2004.

[25] S. Pirozzoli, F. Grasso, , and T. B. Gatski. Direct numerical simulation and analysis of a spatially evolving supersonic turbulent boundary layer at m=2.25. *Phys. Fluids*, 16:530, 2004.

[26] W. Rodi. Turbulence models and their application in hydraulics - a state-of- the-art review. *An IAHR (International Association of Hydraulic Research) Publication, Delft, The Netherlands*, 1980.

[27] M. Aouissi, A. Bounif, and K. Bensayah. Scalar turbulence model investigation with variable turbulent prandtl number in heated jets and diffusion flames. *Heat Mass Transfer*, 44:1065, 2008.

[28] R. M. C. So and T. P. Sommer. An explicit algebraic heat-flux model for the temperature field. *Int. J. Heat Mass Transfer.*, 39(3):455–465, 1996.

[29] K. Abe and K. Suga. Towards the development of a reynolds-averaged algebraic turbulent scalar-flux model. *International Journal of Heat and Fluid Flow*, 22:19–29, 2001.

[30] N. Uddin, S. O. Neumann, B. Weigand, and B. A. Younis. Large-eddy simulations and heat-flux modeling in a turbulent impinging jet. *Numerical Heat Transfer, Part A*, 55: 906–930, 2009.

[31] B. J. Daly and F. H. Harlow. Transport equations in turbulence. *The physics of fluids*, 13(11):2634, 1970.

[32] B. A. Younis, C. G. Speziale, and T. T. Clark. A rationale model for turbulent scalar fluxes, proc. of the royal society a. *Proc. of the Royal Society A*, 461:575–594, 2005.

[33] A. Shams, F. Roelofs, E. Baglietto, S. Lardeau, and S. Kenjeres. Assessment and calibration of an algebraic turbulent heat flux model for low-prandtl fluids. *International Journal of Heat and Mass Transfer*, 79:589–601, 2014.

[34] A. Pucciarellia, I. Borronia, M. Sharabib, and W. Ambrosini. Results of 4-equation turbulence models in the prediction of heattransfer to supercritical pressure fluids. *Nuclear Engineering and Design*, 281:5–14, 2015.

[35] H. Schneider, D. A. V. Terzi, Hans-Jörg Bauer, and W. Rodi. Coherent structures in trailing-edge cooling and the challenge for turbulent heat transfer modelling. *International Journal of Heat and Fluid Flow*, 51:110–119, 2015.

[36] H. Müller, B. A. Younis, and B. Weigand. Development of a compact explicit algebraic model for the turbulent heat fluxes and its application in heated rotating flows. *International Journal of Heat and Mass Transfer*, 86:880–889, 2015.

[37] A. A. Pasha. Application of shock-unsteadiness model to hypersonic shock/turbulent boundary-layer interaction. Technical report, Ph.D. Thesis, Indian Institute of Technology Bombay, 2011.

[38] A. A. Pasha and K. Sinha. Shock-unsteadiness model applied to oblique shock-wave/turbulent boundary-layer interaction. *Int. J. Comput. Fluid Dyn.*, 22 (8):569–582, 2008.

[39] M. S. Holden. Studies of the mean and unsteady structure of turbulent boundary-layer separation in hypersonic flow. *AIAA paper*, page 1778, 1991.

[40] K. Sinha, K. Mahesh, and G. V. Candler. Modeling the effect of shock unsteadiness in shock-wave / turbulent boundary-layer interactions. *AIAA Journal*, 43 (3):586–594, 2005.

[41] L. S. G. Kovasznay. Turbulence in supersonic flow. *J. Aeronaut. Sci.*, 20 (10):657–674, 1953.

[42] M. M. Stanišić and L. S. G. Kovasznay. Weak fluctuation modes of an electrically and thermally conducting viscous incompressible fluid in a homogeneous magnetic field. *Physics of Fluids*, 13(1):32–36, 1970.

[43] P.E. Doak. Momentum potential theory of energy flux carried by momentum fluctuations. *Journal of Sound and Vibration*, 131(1):67 – 90, 1989.

[44] S. Sarkar, G. Erlebacher, and M. Y. Hussaini. Compressible homogeneous shear: Simulation and modeling. *Turbulent Shear Flows*, 8:249–267, 1993.

[45] K. Mahesh, S. Lee, S. K. Lele, and P. Moin. The interaction of an isotropic field of acoustic waves with a shock wave. *J. Fluid Mech.*, 300:383–407, 1995.

[46] F. K. Moore. Unsteady oblique interaction of a shock wave with a plane disturbance. Technical Report 2879, NACA Report, 1954.

[47] J. L. Kerrebrock. The interaction of flow discontinuities with small disturbances in a compressible fluid. Technical report, Ph.D. Thesis, Califor- nia Inst. of Technology, 1956.

[48] C. T. Chang. Interaction of a plane shock and oblique plane disturbances with special reference to entropy waves. *J. Aeronaut. Sci.*, 24:675–682, 1957.

[49] H. S. Ribner. Acoustic energy flux from shock-turbulence interaction. *J. Fluid Mech.*, 35 (2):299–310, 1969.

[50] H. S. Ribner. Spectra of noise and amplified turbulence emanating from shock-turbulence interaction. *AIAA Journal*, 25 (3):436–442, 1987.

[51] S. Lee, S. K. Lele, and P. Moin. Direct numerical simulation of isotropic turbulence interacting with a weak shock wave. *J. Fluid Mech.*, 251:533–562, 1993.

[52] S. Lee, S. K. Lele, and P. Moin. Interaction of isotropic turbulence with shock waves: effect of shock strength. *J. Fluid Mech.*, 340:225–247, 1997.

[53] S. Jamme, J.-B. Cazalbou, F. Torres, and P. Chassaing. Direct numerical simulation of the interaction between a shock wave and various types of isotropic turbulence. *Flow, Turbulence and Combustion*, 68:227–268, 2002.

[54] D. Fabre, L. Jacquin, and J. Sesterhenn. Linear interaction of a cylindrical entropy spot with a shock. *Phys. Fluids*, 13(8):2403–2422, 2001.

[55] J. Griffond. Linear interaction analysis for richtmyer-meshkov instability at low atwood numbers. *Phys. Fluids*, 18:054106, 2006.

[56] J. Larsson and S. K. Lele. Direct numerical simulation of canonical shock-turbulence interaction. *Phys. Fluids*, 21:126101, 2009.

[57] J. Ryu and D. Livescu. Turbulence structure behind the shock in canonical shock-vortical turbulence interaction. *J. Fluid Mech.*, 756:R1, 2014.

[58] P. W. Duck, D. G. Lasseigne, and M. Y. Hussaini. On the interaction between the shock wave attached to a wedge and freestream disturbances. *Theoretical and Computational Fluid Dynamics*, 7(2):119–139, 1995.

[59] J. F. McKenzie and K. O. Westphal. Interaction of linear waves with oblique shock waves. *Physics of Fluids*, 11(11), 1968.

[60] K. Mahesh, S. K. Lele, and P. Moin. The response of anisotropic turbulence to rapid homogeneous one dimensional compression. *Phys. Fluids*, 6(2), 1994.

[61] L. Jacquin, C. Cambon, and E. Blin. Turbulence amplification by a shock wave and rapid distortion theory. *Physics of Fluids A*, 5(10):2539–2550, 1993.

[62] S. Lee, P. Moin, and S. K. Lele. Interaction of isotropic turbulence with a shock wave. Technical Report 52, Thermosciences division, Department of Mechanical Engineering, Stanford University, Stanford, CA., 1992.

[63] D. A. Donzis. Amplification factors in shock–turbulence interactions: effect of shock thickness. *Phys. Fluids*, 24:011705, 2012.

[64] D. A. Donzis. Shock structure in shock–turbulence interactions. *Phys. Fluids*, 24:126101, 2012.

[65] D. Livescu and J. Ryu. Vorticity dynamics after the shock–turbulence interaction. *Shock Waves*, pages 1–11, 2015. ISSN 0938-1287. doi: 10.1007/s00193-015-0580-5.

[66] K. Sinha and S. J. Balasridhar. Conservative formulation of the $k - \epsilon$ turbulence model for shock-turbulence interaction. *AIAA Journal*, 51 (8):1872–1882, 2013.

[67] N. N. Fedorova and I. A. Fedorchenko. Computations of interaction of an incident oblique shock wave with a turbulent boundary layer on a flat plate. *Journal of Applied Mechanics and Technical Physics*, 45(3):358–366, 2004.

[68] D. C. Wilcox. In *Turbulence modeling for CFD*. DCW Industries, Inc., 2006.

[69] F. M. White. In *Viscous Fluid Flow*. Mcgraw Hill Series in Mechanical Engineering, 2005.

[70] A. J. Smits and J. Dussage. In *Turbulent Shear Layers in Supersonic Flow*. Springer, 2006.

[71] S. B. Pope. In *Turbulent Flows*. Cambridge Univ. Press, London, 2000.

[72] J. Larsson. Effect of shock-capturing errors on turbulence statistics. *AIAA Journal*, 48(7): 1554–1557, 2010.

[73] F. Ducros, F. Laporte, T. Soulères, V. Guinot, P. Moinat, and B. Caruelle. High-order fluxes for conservative skew-symmetric-like schemes in structured meshes: Application to compressible flows. *Journal of Computational Physics*, 161(1):114 – 139, 2000.

[74] J. R. Ristorcelli and G. A. Blaisdell. Consistent initial conditions for the DNS of compressible turbulence. *Phys. Fluids*, 9(1):4–6, 1997.

[75] A. E. Hanifi, P. H. Alfredsson, A. V. Johansson, and D. S. Henningson. In *Transition, Turbulence and Combustion Modelling*. ERCOFTAC Series, 1999.

[76] R. Quadros, K. Sinha, and J. Larsson. Turbulent energy flux generated by shock/homogeneous-turbulence interaction. *Submitted to J. Fluid Mech.*, 2016.

[77] H. Tennekes and J. L. Lumley. In *A First Course in Turbulence*. The MIT press, 1972.

[78] H. Loyau, P. Batten, and M. A. Leschziner. Modelling shock/boundary-layer interaction with nonlinear eddy-viscosity closures. *Flow, Turbulence and Combustion*, 60:257–282, 1998.

[79] F. A. Haidinger and R. Friedrich. Computation of shock wave/turbulent boundary layer interactions using a two-equation model with compressibility corrections. *Flow, Turbulence and Combustion*, 51:501–505, 1993.

List of Publications

Journal papers

- **Quadros, R.**, Sinha, K. and Larsson, J. "Turbulent energy flux generated by shock/ homogeneous-turbulence interaction", *accepted in Journal of Fluid Mechanics*, March, 2016.

- **Quadros, R.**, Sinha, K. and Larsson, J. "Kovasznay Mode Decomposition of Velocity-Temperature Correlation in Canonical Shock-Turbulence Interaction", *accepted in Flow, Turbulence and Combustion*, February, 2016, DOI: 10.1007/s10494-016-9722-9.

- **Quadros, R.** and Sinha, K. "Modelling of turbulent energy flux in canonical shock-turbulence interaction". *submitted to International Journal of Heat and Fluid Flow*, March, 2016.

Conference papers and reports (peer reviewed)

- **Quadros, R.**, Larsson, J. and Sinha, K. "Modelling of turbulent energy flux in shock-turbulence interaction" Presented at *International symposium on Turbulence and Shear Flow Phenomena*, Australia, 2015.

- **Quadros, R.**, Sashittal, P., Ramachandran, A., and Sinha, K. "Evolution of turbulent heat flux across a shock wave." 5^{th} *European Conference for Aeronautics and Space Sciences*, Germany, 2013.

- **Quadros, R.**, Sinha, K. "Physics based modeling of turbulent heat flux in shock dominated flows." 2^{nd} *SFB-TR 40 Summer program research briefs.*, Germany, 2013.

Published abstracts and conference presentations

- **Quadros, R.**, Sinha, K. and Larsson, J. "Modal analysis in shock-turbulence interaction" *IUTAM symposium on Advances in Computation, Modelling and control of transitional and turbulent flows*, India, 2015.

- **Quadros, R.**, Thirupathi, M., Larsson, J., and Sinha, K. "Reynolds stress budgets in canonical shock-turbulence interaction." 3^{rd} *National symposium on Shock waves.*, India, 2014

ACKNOWLEDGEMENTS

I am grateful to my advisor Prof. Krishnendu Sinha for guiding me along the wonderful, and sometimes arduous journey of research. My heartfelt thanks to Prof. Johan Larsson, our collaborator, for the endless support, countless email discussions and untiring patience, which helped me tremendously. I would also like to thank Prof. Rama Govindrajan, Prof. Datta Gaitonde and Prof Joseph Mathew, who reviewed my thesis and provided really insightful comments. Thanks are also to Prof. Amit Agarwal and Prof. Sudarshan who guided me in my annual review seminars. I am thankful to Indian Space Research Organisation-Space Technology Cell (ISRO-STC) and Aeronautics Research and Development Board (ARDB) for partially supporting my research.

I would like to thank my friend Abhishek Shankaran, looking at whom I have learnt the meaning of perseverance. A special thanks to my current and former labmates, Palash, Ashwin, Yogesh, Bijaylakshmi, Vishnu, Vignesh, Nithiyaraj, Anand Sudhi, Sarvesh and Balasridhar. My friends and my labmates, Nitin, Rajhansa and Maninder, thanks to you guys, the lab was a fun place. My dear friends, Pavan, Anu, Puneeth, Mathew, Tara, Carl, Nisha, Audrey, Divya and Vishal, thank you for your amazing support. I thank all the wonderful people of my Christian fellowship, who have been a constant source of support in all my endeavours. My dearest brother Royan and sis-in-law Jenny, without your ever-present help, I could never accomplish this journey. My deepest gratitude to Clemitha, my beloved, for the being a pillar of strength to me. There are many others whose name may not have surfaced here, but I thank them with all my heart for trusting in me and helping in big and small ways over the years. Last but not the least, my parents, no words could express what an amazing source of support and strength you have been through out my life.